



# Conception d'impulsions non-sélectives refocalisantes en transmission parallèle pour l'Imagerie par Résonance Magnétique du Cerveau Humain à très Haut Champ

Aurélien Massire

## ► To cite this version:

Aurélien Massire. Conception d'impulsions non-sélectives refocalisantes en transmission parallèle pour l'Imagerie par Résonance Magnétique du Cerveau Humain à très Haut Champ. Medical Physics [physics.med-ph]. Université Paris Sud - Paris XI, 2014. English. NNT : 2014PA112180 . tel-01165058

**HAL Id: tel-01165058**

**<https://theses.hal.science/tel-01165058>**

Submitted on 18 Jun 2015

**HAL** is a multi-disciplinary open access archive for the deposit and dissemination of scientific research documents, whether they are published or not. The documents may come from teaching and research institutions in France or abroad, or from public or private research centers.

L'archive ouverte pluridisciplinaire **HAL**, est destinée au dépôt et à la diffusion de documents scientifiques de niveau recherche, publiés ou non, émanant des établissements d'enseignement et de recherche français ou étrangers, des laboratoires publics ou privés.

UNIVERSITÉ PARIS-SUD

ÉCOLE DOCTORALE 422 :  
SCIENCES ET TECHNOLOGIES DE L'INFORMATION DES TÉLÉCOMMUNICATIONS  
ET DES SYSTÈMES

Laboratoire : NeuroSpin UNIRS

# THÈSE DE DOCTORAT SUR TRAVAUX

PHYSIQUE

par

**Aurélien Emilien Florian Massire**

Non-selective Refocusing Pulse Design in Parallel  
Transmission for Magnetic Resonance Imaging of the  
Human Brain at Ultra High Field

**Date de soutenance : 26/09/2014**

**Composition du jury :**

Directeur de thèse :  
Rapporteurs :

Examineurs :

Denis Le Bihan  
Ulrich Katscher  
Jean-Philippe Ranjeva  
Jean-Christophe Ginefri  
Alexis Amadon

Directeur, CEA NeuroSpin.  
Senior Scientist, Philips Research  
Professeur, Université Aix-Marseille.  
Maître de Conférence, Univ. Paris XI.  
Ingénieur chercheur CEA NeuroSpin.



# Preface



This thesis is submitted in partial fulfillment of the requirements for the Degree of Doctor of Philosophy at University Paris-Sud XI. The results presented herein are based on the author's scientific work performed between March 2011 and July 2014 at NeuroSpin.

This manuscript focuses on the development of parallel-transmission strategies to maximize the performances of current and future ultra-high field Magnetic Resonance Imaging systems, including the whole body 11.7 Tesla setup expected in NeuroSpin in 2015.



**© Aurélien Massire 2014**



# Contents

<b>Acknowledgments.....</b>	<b>9</b>
<b>French abstract .....</b>	<b>11</b>
<b>General Introduction .....</b>	<b>14</b>
<b>Thesis Overview .....</b>	<b>16</b>
<b>1. Scientific Background.....</b>	<b>17</b>
<b>1.1. Nuclear Magnetic Resonance .....</b>	<b>17</b>
1.1.1. Nuclear spins.....	17
1.1.2. Bloch equation .....	18
1.1.3. Relaxation .....	19
1.1.4. The NMR signal .....	20
<b>1.2. Magnetic Resonance Imaging.....</b>	<b>21</b>
1.2.1. Principle.....	21
1.2.2. MRI hardware.....	23
1.2.3. MRI signal acquisition & contrast.....	24
1.2.4. MRI sequences .....	25
1.2.5. Spin echo-based MRI sequences .....	27
1.2.6. Turbo Spin Echo-based MRI sequences .....	29
1.2.7. Variable Flip Angle Turbo Spin Echo-based MRI sequences.....	31
<b>1.3. Specific Absorption Rate.....</b>	<b>36</b>
1.3.1. Definition .....	36
1.3.2. Guidelines .....	36
<b>1.4. Ultra High Field MRI .....</b>	<b>38</b>
1.4.1. Advantages.....	38
1.4.2. Challenges.....	40
1.4.3. Solutions .....	42
<b>2. MRI Pulse Design &amp; Parallel Transmission .....</b>	<b>44</b>
<b>2.1. Radio-Frequency Pulse Design .....</b>	<b>44</b>
2.1.1. Multi-dimensional RF Pulses and k-space interpretation .....	44
2.1.2. Trajectories through k-space .....	46
<b>2.2. MRI Coils .....</b>	<b>48</b>
2.2.1. Types of MRI coils .....	48
2.2.2. Multiple channel coils.....	49

<b>2.3. <math>B_1^+</math> Mapping</b>	<b>50</b>
<b>2.4. Parallel Transmission</b>	<b>51</b>
2.4.1. Origins	51
2.4.2. Spatial Domain method	55
2.4.3. Magnitude Least Square Problem	57
2.4.4. Large Tip Angle design and Optimal Control theory	58
<b>3. Experimental Setup</b>	<b>60</b>
<b>3.1. MRI system</b>	<b>60</b>
3.1.1. Magnet	60
3.1.2. Gradient & Shim Coils	61
3.1.3. Radio-Frequency Chain	62
3.1.4. Transmit-Array Coil	63
<b>3.2. Other Materials</b>	<b>65</b>
3.2.1. MRI phantom manufacturing	65
3.2.2. Computational Resources	67
<b>4. Specific Absorption Rate Assessment</b>	<b>68</b>
<b>4.1. Ensuring patient safety</b>	<b>68</b>
4.1.1. Aims	68
4.1.2. Strategies	69
<b>4.2. Methods for SAR prediction and assessment</b>	<b>71</b>
4.2.1. Conventional MRI systems	71
4.2.2. pTX-enabled MRI systems	71
<b>4.3. SAR prediction validation</b>	<b>72</b>
4.3.1. $B_1^+$ measurements and electromagnetic simulations	72
4.3.2. MRI Thermometry and temperature simulations	76
<b>4.4. Online SAR assessment based on time-averaged power measurements</b>	<b>77</b>
4.4.1. Methods	78
4.4.2. Practical implementation	80
4.4.3. Future SAR monitoring	82
<b>5. Thermal simulations in the human head for high field MRI using parallel transmission</b>	<b>83</b>
<b>5.1. Introduction</b>	<b>85</b>
<b>5.2. Materials and Methods</b>	<b>86</b>
5.2.1. Head model	86
5.2.2. Coil design and electromagnetic simulations	88

5.2.3. SAR calculation.....	90
5.2.4. Thermal calculations .....	90
5.2.5. Monte Carlo simulations .....	92
5.2.6. Circularly-polarized mode simulations.....	92
5.2.7. Realistic parallel transmission RF exposure simulations .....	93
<b>5.3. Results.....</b>	<b>94</b>
5.3.1. SAR in the human head model.....	94
5.3.2. Temperature distributions for random static RF configurations .....	95
5.3.3. CP-mode simulations .....	97
5.3.4. MRI sequence simulations .....	98
<b>5.4. Discussion.....</b>	<b>99</b>
<b>6. Design of non-selective refocusing pulses with phase-free rotation axis by gradient ascent pulse engineering algorithm in parallel transmission at 7 T .....</b>	<b>102</b>
<b>6.1. Introduction .....</b>	<b>104</b>
<b>6.2. Theory.....</b>	<b>105</b>
6.2.1. Spin-domain Bloch equation .....	106
6.2.2. Performance criterion.....	107
6.2.3. GRAPE algorithm .....	108
6.2.4. Extension to tailoring gradient waveforms.....	109
<b>6.3. Experiments .....</b>	<b>109</b>
6.3.1. Experimental setup.....	109
6.3.2. $B_1$ and $B_0$ mapping .....	110
6.3.3. Pulse design .....	110
6.3.4. Measurement of the rotation matrix induced by the refocusing pulse .....	111
6.3.5. Spin echo sequence.....	112
<b>6.4. Results.....</b>	<b>113</b>
6.4.1. Pulse design .....	113
6.4.2. Measurement of the rotation matrix induced by the refocusing pulse .....	115
6.4.3. Spin echo measurement.....	116
<b>6.5. Discussion.....</b>	<b>117</b>
6.5.1. The GRAPE algorithm .....	117
6.5.2. Phase-free refocusing pulses are strictly equivalent to inversion pulses.....	118
6.5.3. Quantum Process Tomography .....	119
6.5.4. Spin-echo results .....	120
<b>6.6. Conclusion .....</b>	<b>120</b>



<b>7. Parallel-transmission-enabled 3D T<sub>2</sub>-weighted imaging of the human brain at 7 Tesla</b>	<b>121</b>
<b>7.1. Introduction</b>	<b>123</b>
<b>7.2. Theory</b>	<b>125</b>
7.2.1. GRAPE aiming at any given refocusing angle with a phase-free transverse rotation axis	125
7.2.2. GRAPE aiming at any given refocusing angle with a specific phase pattern target	127
<b>7.3. Methods</b>	<b>129</b>
7.3.1. Experimental setup	129
7.3.2. Online fast pTX calibration and pulse design	130
7.3.3. Sequence design and validation	131
7.3.4. SAR evaluation	132
<b>7.4. Results</b>	<b>132</b>
7.4.1. pTX calibration and pulse design	132
7.4.2. Sequence validation	134
7.4.3. SPACE & FLAIR T <sub>2</sub> -weighted images	135
7.4.4. T <sub>2</sub> -weighted images automated segmentation	137
<b>7.5. Discussion</b>	<b>138</b>
<b>7.6. Conclusion</b>	<b>140</b>
<b>General Conclusion &amp; Perspectives</b>	<b>140</b>
<b>List of Publications</b>	<b>143</b>
<b>Nomenclature</b>	<b>145</b>
<b>Bibliography</b>	<b>148</b>

# Acknowledgments

I would like to express my appreciation to all the people that collaborated with me during these profitable and enjoyable three years.

First, I would like to thank my thesis director, Denis Le Bihan, who is also the director of NeuroSpin, for giving me the opportunity to work and learn in such a great environment, when he initially transmitted my internship application to my advisors. It has been a great honor to work in these facilities of international level. I would also like to thank Cyril Poupon, the head of the UNIRS unit, for financing my internship with his own funding. It was a decisive step for allowing me to carry on my studies, enabling my application to the IRTTELIS PhD Program of the DSV and getting my PhD in CEA.

I am sincerely grateful to Nicolas Boulant and Alexis Amadon, my thesis advisors, for their continuous support and teaching throughout all my scientific endeavors. I have learnt more than ever thanks to them. Their attitude towards both work and scientific reasoning is an inspiration for me. Over the years, I admired Nicolas' perseverance and dedication to understand every physics concept to its roots, as well as Alexis' patience and global vision towards MRI. I would also like to thank them for their generous support for the future and for proofreading my manuscript.

I would also like to express all my gratitude to Alexandre Vignaud, who really acted as my third advisor, which is something that really few PhD students can benefit from. I highly value all his advices, both regarding my professional career and my personal life. I also consider him as a model to follow.

It has been a real pleasure to work with many people from NeuroSpin and IRFU. Among them, my first thoughts go to Martijn Cloos, the PhD student who preceded me and from whom I learnt probably the most. He has impressive skills and a broad knowledge about pulse design, brain anatomy, programming and MRI in general, and he helped me a lot during my first year of PhD.

I would like to thank Michel Luong for his kindness when working with him, and for his advanced expertise on RF-coil design and electromagnetic simulations. I thank Guillaume Ferrand, a former PhD student of Michel's, for his time dedicated to the development of the transmit-array coil used throughout this work and upcoming new coils. Many thanks also to Christopher J. Wiggins for his work on the 7 Tesla scanner, to Karl Edler for invigorating discussions with a foreign colleague, to Eric Giacomini and Marie-France Hang for their really precious help fixing the MRI coil even under time pressure. Friendly thanks to Benoit Schmitt, a former fellow student of my engineering school and NeuroSpin PhD student, who

advised me for my application to IRTELIS. More generally, I thank all my colleagues from the UNIRS for the healthy working atmosphere and for their scientific values. Last, warm thanks to Alfredo Lopez Kolkovsky, my fellow PhD student from IRTELIS, who dedicated his time to improve spectroscopy in NeuroSpin and shared his time facing the same difficulties during these three years.

It has been a great pleasure to work in NeuroSpin and enjoy every little moment in there, the community of PhD students was exceptionally invigorating. I would like to thank everyone in the other labs of this facility; I had a really great time among you.

Special thanks to my colleagues and friends, who shared with me these perilous years: Elodie Cauvet, Baptiste Gauthier and Catherine Wacongne. Now all of you are PhD and in your own specific way you showed me how to grow, both personally and professionally. To Elodie: many thanks for my integration in Neurospin, I will never forget how we met and the really precious time we had. To Baptiste: thank you for the good time we had, and for your brilliant spirit, which is good deep down, I guess. To Catherine: thank you for introducing me to the Aikido world and for sharing with me all these little moments of joy, anger and hope. I have many names to cite (and many more that I would have to): Gaël Varoquaux, Anne Kosem, Nicolas Zilber, Lucie Charles, Ileana Jelescu, Olivier Reynaud, Guillaume Radecki, Yann Leprince, Johanna Laversin, Urielle Thoprakharn, Benoit Larrat, Andrès Hoyos, Yannick Schwartz, Benoit Da Mota, Claire Chang, Gaël Saib, and many more...

The technical support from the Siemens Healthcare team was appreciated, for this I thank Luc Renou for fixing the 7 Tesla scanner, Franck Mauconduit for advanced pTX programming, and Benjamin Robert especially, who help me a lot with the SPACE sequence, his skills in programming were a huge breakthrough in my project. I would also like to give my appreciations to Séverine B, Séverine R, Chantal and the nurses for their hard-working and support.

I would like to thank Laura Dupas, the PhD student who will be continuing the team effort to enhance the pTX capabilities available to the lab, for the good time we spent together and the work we accomplished, I wish her the best for the future.

Finally, I would like to thank my brother Hugo and my sister Flora, my parents Jean-Paul and Evelyne, for their unconditional love and support. And last, because having someone who cares about you, understands you better than anyone, and loves you every day is the best motivation one could ever wish for, many thanks to you, Matilde.

**Aurélien Massire**

**Gif-sur-Yvette, France. July 2014.**

## French abstract

En Imagerie par Résonance Magnétique (IRM), l'augmentation de la valeur du champ magnétique statique permet en théorie de fournir un rapport signal sur bruit accru, améliorant ainsi la qualité des images produites. L'objectif de l'IRM à ultra haut champ est d'atteindre une résolution spatiale suffisamment haute pour pouvoir distinguer des structures si fines (soit l'échelle de quelques centaines de neurones) qu'elles sont actuellement impossibles à visualiser de façon non-invasive. Le Commissariat à l'Energie Atomique et aux Energies Alternatives (CEA) s'inscrit directement dans cette dynamique, avec l'installation imminente d'un imageur IRM clinique à 11.7 Tesla unique en son genre. Celui-ci est actuellement en fabrication, et sera rendu opérationnel au cours de l'année 2015 à NeuroSpin. Cet appareil de nouvelle génération, dont la réalisation en elle-même mobilise d'importants moyens, ambitionne de faire avancer l'imagerie médicale à un niveau inédit.

Cette dynamique tournée vers les hauts champs est un formidable élan qui mobilise de nombreux chercheurs du monde entier afin de développer de nouvelles méthodes d'acquisition prenant en compte le changement de régime imposé par les fréquences électromagnétiques très élevées (transmission et reconstruction parallèles, impulsions radiofréquences et réseaux d'antennes dédiées...). En effet, à de telles valeurs de champs magnétiques statiques, la longueur d'onde du rayonnement électromagnétique envoyé pour basculer les spins des protons de l'eau est du même ordre de grandeur que l'objet dont on souhaite faire l'image (soit environ 13 cm à 7 Tesla). Des phénomènes d'interférences ondulatoires sont alors observés, ce qui se traduit par l'inhomogénéité de ce champ radiofréquence (RF) au sein de l'objet, qui est d'autant plus accentuée à très hauts champs. Ces interférences engendrent alors des artefacts de signal et/ou de contraste dans les images IRM, et rendent ainsi leur exploitation délicate voire impossible dans certaines régions du corps. Il est donc crucial de fournir des solutions pour atténuer la non-uniformité de l'excitation des spins. A défaut de quoi, de tels systèmes d'imagerie à très haut champ ne pourront atteindre leurs pleins potentiels.

Pour obtenir des diagnostics cliniques pertinents à très haut champ, il est donc nécessaire de créer des impulsions RF homogénéisant l'excitation de l'ensemble des spins (ici du cerveau humain), optimisées pour chaque individu que l'on souhaite imager. Pour cela, un système de transmission parallèle (pTX) à 8 canaux a été installé au sein de notre imageur à 7 Tesla. Alors que la plupart des systèmes IRM cliniques n'utilisent qu'un seul canal d'émission, l'extension pTX permet de jouer différentes formes d'impulsions RF de concert

sur plusieurs canaux. La somme résultante de ces interférences doit alors être optimisée pour atténuer la non-uniformité observée classiquement.

L'objectif de cette thèse est donc de synthétiser ce type d'impulsions RF élaborées, en utilisant la transmission parallèle. Ces impulsions auront pour contrainte supplémentaire le respect des limitations internationales en vigueur concernant l'exposition à des champs radiofréquence, qui induit une hausse de température dans les tissus. En ce sens, de nombreuses simulations électromagnétiques et de températures ont été réalisées en introduction de cette thèse, afin d'évaluer la relation entre les seuils recommandés d'exposition RF et l'élévation de température effectivement prédite dans les tissus. Les résultats de ces simulations indiquent que les recommandations de TAS (Taux d'Absorption Spécifique) semblent : 1) être une métrique adaptée pour s'assurer que la température dans la tête ne dépasse pas des valeurs dangereuses pour la santé dans le cadre d'examens IRM en transmission parallèle à 7 Tesla et 2) sont plus limitantes que des seuils de température (qui reste très difficile à mesurer en temps réel), à l'exception des yeux.

Cette thèse porte plus spécifiquement sur la conception de l'ensemble des impulsions RF refocalisantes utilisées dans des séquences IRM non-sélectives, basées sur l'écho de spin. Dans un premier temps, seule une impulsion RF a été générée, pour une application simple : l'inversion du déphasage des spins dans le plan transverse, dans le cadre d'une séquence spin écho classique. Dans un deuxième temps, sont considérées les séquences à très long train d'échos de refocalisation appliquées à l'imagerie in vivo. Dans tous les cas, l'opérateur mathématique agissant sur la magnétisation, et non pas son état final comme il est fait classiquement, est optimisé. Le gain en imagerie à très haut champ est clairement visible puisque les opérations mathématiques (c'est-à-dire la rotation des spins) voulues sont réalisées avec bien plus de fidélité que dans le cadre des méthodes de l'état de l'art.

Pour cela, la génération de ces impulsions RF combine une méthode d'excitation des spins avec navigation dans l'espace de Fourier, les  $k_T$ -points, et un algorithme d'optimisation, appelé Gradient Ascent Pulse Engineering (GRAPE), utilisant le contrôle optimal. Le principe des  $k_T$ -points est de limiter la trajectoire de l'espace-k de transmission (parcourue avec les gradients du scanner) à un petit groupe de points autour du centre de cet espace. De cette façon, comme les inhomogénéités RF sont dominées par de basses fréquences spatiales, la limitation des excursions dans l'espace-k garantit qu'aucune énergie n'est gaspillée à des fréquences spatiales élevées d'un faible intérêt pour l'uniformisation de l'excitation des spins. De plus, le temps requis pour couvrir les quelques  $k_T$ -points est minimisé, permettant une faible durée des impulsions simultanées résultantes.

Pour étendre la portée des  $k_T$ -points aux séquences utilisant l'écho de spin, il est nécessaire de leur donner des propriétés refocalisantes du déphasage des spins, induit dans le plan transverse, pour produire une image de qualité, sans utiliser les approximations typiquement

utilisées. Les stratégies d'optimisation classiques font en effet une approximation, appelée « classe linéaire de grand angle de bascule », pour optimiser l'angle de rotation des spins de façon homogène. Toutefois, ces stratégies d'optimisation tentent une telle opération via une approximation rendue possible par une certaine symétrie imposée dans les impulsions RF et dans la trajectoire dans l'espace  $k$ . Cette approximation se détériore pour de grandes valeurs d'angles de bascule et introduit donc des erreurs dans la manipulation de la magnétisation, qui se répercutent ensuite dans l'image produite. Pour finir, ce formalisme n'est strictement valide qu'en l'absence d'offset de champ statique dans le repère tournant, une approximation plus que grossière dans le cerveau humain à très haut champ.

Une originalité supplémentaire de cette méthode est qu'elle permet la conception d'impulsions RF avec des contraintes spécifiques, selon l'utilisation faite de l'impulsion RF dans la séquence. Celle-ci peut par exemple posséder un angle de refocalisation de valeur choisie, ou encore soit une distribution de phase précise, soit une distribution de phase laissée libre. La totalité des impulsions RF utilisées dans une séquence d'imagerie à très long train d'échos peut être conçue par le biais de cette méthode en une seule fois, ce qui constitue également une nouveauté (le plus souvent, une seule impulsion est conçue, puis dilatée pour obtenir les autres). Cette conception est relativement rapide par rapport à l'état de l'art, grâce à des calculs analytiques plus directs que des méthodes de différences finies. La prise en compte d'un très grand nombre de paramètres nécessite l'usage de GPUs (*Graphics Processing Units*) pour atteindre des temps de calcul compatibles avec un examen clinique.

Cette méthode de conception d'impulsions RF a été validée expérimentalement avec succès sur l'imager 7 Tesla de NeuroSpin, sur une cohorte de volontaires sains. Un protocole d'imagerie, d'abord testé à de multiples reprises sur fantômes (des boules d'eau de la taille d'un cerveau humain servant à tester les réglages de la machine), a été développé pour évaluer l'amélioration de la qualité des images par rapport à des impulsions RF non optimisées, typiquement utilisées.

L'ensemble des développements méthodologiques réalisés au cours de cette thèse a donc contribué à améliorer les performances de l'IRM à très haut champ à NeuroSpin, en augmentant le nombre de séquences IRM compatibles en mode de transmission parallèle. De futurs développements sont prévus afin d'augmenter encore les possibilités de la transmission parallèle, en particulier concernant l'acquisition ultra-rapide et simultanée de plusieurs coupes d'imagerie. L'ensemble des travaux présentés dans ce manuscrit, ainsi que les futurs travaux menés, devraient contribuer à faire fonctionner le futur aimant corps entier de 11.7 Tesla à son plein potentiel.

# General Introduction

Medical imaging is the technique of creating visual representations of the body internal structures. It concerns a wide variety of methods dedicated to aid the diagnosis process and to contribute to the understanding of pathological conditions. It incorporates advanced techniques such as: X-ray radiography, magnetic resonance imaging, ultrasounds imaging and nuclear medicine imaging.

Recording techniques like electroencephalography (EEG), magnetoencephalography (MEG) and electrocardiography (ECG), which are not designed to produce images, can also be considered as forms of medical imaging.

From the perspective of both patient comfort and clinical performance, in particular when considering delicate anatomical structures with limited regenerative capabilities such as the brain, non-invasive medical imaging techniques are preferable. The term noninvasive is used to denote a procedure where no instrument is introduced into a patient's body, which is the case for most imaging techniques currently used.

Over the years, several non-invasive tomography methods have been developed to provide clinically relevant images. Among the most well-known three-dimensional imaging techniques to date are: Computed Tomography (CT), Positron Emission Tomography (PET) and Magnetic Resonance Imaging (MRI).

Although each of the aforementioned techniques has its merits (with regards to spatial resolution, temporal resolution, sensitivity, cost, etc.), the first two of them both involve ionizing radiations, which are inherently harmful and potentially lethal to biological tissues, the latter property being used in radiotherapy for the treatment of cancer.

CT is a technology that uses X-rays to produce a three-dimensional image of the inside of an object from a large series of two-dimensional radiographic images taken around a single axis of rotation. Nuclear medicine uses radioactive material to diagnose or treat various pathologies. Relatively short lived isotope is administered to the patient and gamma cameras are used to detect regions of biologic activity that may be associated with disease, such as tumors. MRI uses powerful magnets to polarize and excite hydrogen nuclei in water molecules of living tissues, producing a detectable signal which is further spatially encoded, resulting in images of the exposed organ. Unlike the two methods cited above, MRI does not involve the use of ionizing radiation and is therefore not associated with the same health hazards. There are no known long-term effects on health due to exposure to MRI scans yet. MRI has a wide range of applications in medical diagnosis and there are estimated to be over 25,000 scanners in use worldwide in 2013. MRI is the investigative tool of choice for

brain and central nervous system imaging, as well as musculoskeletal, osteoarticular, breast, abdominal, pelvic and cardiac imaging, it is also vastly used in oncology. Last, functional MRI (fMRI), a functional neuroimaging procedure using MRI technology that measures brain activity by detecting associated changes in blood flow, is a formidable research tool.

With the aim of continuously improving MRI, higher main magnetic field strengths are explored. Combined with recent advances in phased-array-coil technology and sequence development, these Ultra High Field (UHF) systems start to probe spatial resolutions comparable to those of the cytoarchitectonic structures in the brain. Beyond these gains, UHF MRI has been also shown to provide unique functional and physiologic information.

Nevertheless, with strength of 3 Tesla already, the radiofrequency (RF) wavelength corresponding to the proton Larmor frequency becomes comparable to the dimensions of some imaged human body parts. This results in zones of shade and losses of contrast distributed across the images of large organs. When migrating to 7 Tesla and above, RF interferences cause inhomogeneous excitation profiles to emerge in the human brain. Consequently, a sub-optimal Signal-to-Noise Ratio (SNR) is obtained and a strong bias introduced on the desired contrast, hampering tissue delineation with high confidence. It is therefore crucial to provide adequate solutions to mitigate these excitation non-uniformities so that these systems can reach their full potential.

Parallel transmission (pTX) is one of the most promising solutions available to mitigate these artifacts. It utilizes multiple independently driven coil-elements to facilitate relatively short excitation pulses with the flexibility to obtain nearly any excitation pattern (the pulse design approach), almost insensitive to RF distortions. However, there are certain difficulties inherent in this approach, stemming mainly from the potential occurrence of highly localized energy deposition in the exposed volume. Therefore, special care must be taken to prevent tissue damage. In spite of the fact that the relevant safety parameter is the RF induced temperature, for simplicity the Specific Absorption Rate (SAR) is often considered instead. This measure of the energy deposition may then be constrained according to standardized guidelines to provide adequate safety with respect to temperature.

Over the years, various very interesting applications have benefited from the enhanced degrees of freedom introduced by the pTX approach. This thesis herein focuses on the development and demonstration of pTX-based techniques and pulse design to provide substantial advances towards RF pulse refocusing quality in any spin echo-based MRI sequence.



# Thesis Overview

In the first chapter of this thesis, the fundamental concepts of NMR and MRI are introduced, underlying both the advantages encountered at UHF and the corresponding challenges that need to be faced. Subsequently, the concepts and techniques related to pulse design and to the pTX approach are detailed in Chapter 2, followed by an overview of the experimental setup (Chapter 3) used throughout the following chapters. With respect to the goals stated earlier, different scientific and practical contributions were made to the development of the pTX platform at NeuroSpin. The method developed to evaluate the RF energy deposition in the context of human brain imaging, and its experimental validation, are discussed in Chapter 4. Then in Chapter 5, numerical simulations were performed in order to assess the compliance of the SAR guidelines, recommended for MRI scans, with the biological primary parameter of interest, the temperature, to avoid local thermal damage or thermoregulatory problems in the context of parallel transmission MRI. Subsequently, a new pulse design strategy relying on optimal control is introduced to achieve non-selective uniform refocusing at UHF, followed by an in-vitro demonstration at 7 Tesla for the  $180^\circ$  pulse of a spin-echo sequence (Chapter 6). This concept is then generalized to any rotation angle, with a specific focus on the design of rotation matrices rather than final magnetization states. The proposed combination of these refocusing RF pulses is evaluated in-vivo at 7 Tesla in one of the most commonly used  $T_2$ -weighting 3D sequences: the variable flip angle turbo spin echo sequence (Chapter 7). This thesis is concluded with a summary of its scientific contributions and a brief outlook on possible future developments.

# 1. Scientific Background

## 1.1. Nuclear Magnetic Resonance

### 1.1.1. Nuclear spins

Most particles have, besides properties such as mass and charge, an intrinsic form of angular momentum referred to as spin, a quantum mechanical property. Particles with half-integer spins, such as 1/2, 3/2, 5/2, are known as fermions, while particles with integer spins, such as 0, 1, 2, are known as bosons. The two families of particles obey different rules and broadly have different roles in the world around us. The Hydrogen proton is the most abundant spin 1/2 nucleus in organic tissues ([Frieden, 1972](#)), making it the best candidate for medical imaging techniques. All of the experiments performed in this work pertain to proton imaging.

Nuclear Magnetic Resonance (NMR) ([Rabi et al., 1938](#)) is by nature a quantum phenomenon and all its theory can be derived from quantum mechanics. However, a classical mechanics description of a magnetic moment in a magnetic field is possible for single spin systems and is therefore often adopted for simplicity. The basic motion of the proton spin thus may be understood by imagining it as a spinning gyroscope that is also electrically charged, creating its own current loop, capable of interacting with external magnetic fields as well as producing its own. When immersed in a static magnetic field ( $B_0$ ), the magnetic moment vector of the spin will tend to align itself along the static field and precess around the magnetic field direction. The precession angular frequency is referred as the proton Larmor angular frequency:

$$\omega_0 = \gamma B_0 \quad (1.1)$$

where  $\gamma$  is the gyromagnetic ratio ( $\gamma/2\pi = 42.58$  MHz/T for the Hydrogen proton in water). For a proton with two quantum states, only two alignments are possible: parallel alignment (low energy) and anti-parallel alignment (high energy). The quantum energy difference between the two is:

$$\Delta E = \gamma B_0 \hbar \quad (1.2)$$

where  $\hbar$  is the Planck constant divided by  $2\pi$ . Due to this energy difference, at thermal equilibrium the proportion of spins oriented in the parallel direction is greater than that of the spins in the antiparallel direction, the difference being given by Boltzmann's law.

### 1.1.2. Bloch equation

The magnetization vector  $\mathbf{M}_0$ , which results from the magnetic moment sum of the spin population at thermal equilibrium, immersed in the above-mentioned static magnetic field and when  $kT \gg \Delta E$ , is:

$$M_0 = \frac{\rho_0 \gamma^2 \hbar^2}{4kT} B_0 \quad (1.3)$$

where  $\rho_0$  is the spin density and  $k$  is the Boltzmann's constant. This magnetization vector is measured by tipping it away from the external field direction thanks to a transverse radiofrequency (RF) magnetic field whose frequency is adjusted to the Larmor frequency (on resonance). When perturbed by a magnetic field  $\mathbf{B}_{\text{ext}}$ , the magnetization vector  $\mathbf{M} = \{M_x(t), M_y(t), M_z(t)\}^T$  obeys the Bloch equation (Bloch, 1946):

$$\frac{d\mathbf{M}}{dt} = \gamma \mathbf{M} \wedge \mathbf{B}_{\text{ext}} + \frac{1}{T_1} (M_0 - M_z) \mathbf{e}_z - \frac{1}{T_2} \mathbf{M}_T \quad (1.4)$$

where:  $\mathbf{M}_T = M_x + iM_y$  is the transverse magnetization.  $T_1$  and  $T_2$  are the longitudinal relaxation and the transverse relaxation times respectively (Bloch, 1946). These relaxation terms describe the return to equilibrium when only a static field pointing to the z-axis is present. In addition, instead of describing the magnetization in the laboratory frame of reference, it is often more convenient to consider it in the frame rotating at the Larmor frequency  $\omega_0$ , when  $\mathbf{B}_{\text{ext}} = B_0 \mathbf{e}_z$ .

In the context of MRI, the flip-angle (FA or  $\theta$ ) is often adopted to express the result of a RF excitation. If the initial state of the magnetization is  $M_0 \mathbf{e}_z$ , and  $M_z$  is the longitudinal component after the excitation, then the flip angle is expressed by:

$$\theta = \cos^{-1} \left( \frac{M_z}{\|\mathbf{M}\|} \right) \quad (1.5)$$

The value of the angle is given, on resonance, by:

$$\theta = \gamma \int_0^T B_1^+(t) dt \quad (1.6)$$

with  $T$  the duration of the RF pulse and  $B_1^+ = \frac{1}{2}(B_{1,x} + iB_{1,y})$  the positively rotating RF magnetic field applied.

### 1.1.3. Relaxation

Spin-lattice relaxation ( $T_1$ ) is the mechanism by which the longitudinal component of the magnetization vector comes into thermodynamic equilibrium with its surroundings. Indeed, nuclei are held within a lattice structure, and are in constant vibrational and rotational motion, creating a complex fluctuating magnetic field. The magnetic field caused by thermal motion of nuclei within the lattice is called the lattice field. The lattice field of a nucleus in a lower energy state can interact with nuclei in a higher energy state, causing the energy of the higher energy state to distribute itself between the two nuclei. In the rotating frame, it writes:

$$\left(\frac{dM_z}{dt}\right)' = \frac{1}{T_1}(M_0 - M_z) \quad (1.7)$$

which has the solution:

$$M_z(t) = M_0(1 - e^{-t/T_1}) \quad (1.8)$$

The relaxation parameter  $T_1$  ranges from hundreds to thousands of milliseconds for protons in human tissues over all static field strengths available for NMR.

The spin-spin relaxation ( $T_2$ ) is the mechanism by which  $\mathbf{M}_T$ , the transverse component of the magnetization vector, exponentially decays towards its equilibrium value of zero. Indeed, spins experience local fields which are combinations of the applied field and the fields of their neighbors. Since time variations of the local field lead to different local precession frequencies, the individual spins tend to fan out in time, reducing the net transverse magnetization (equation in the rotating frame):

$$\left(\frac{d\mathbf{M}_T}{dt}\right)' = -\frac{1}{T_2}\mathbf{M}_T \quad (1.9)$$

with the solution:

$$M_T(t) = M_T(0) e^{-t/T_2} \quad (1.10)$$

In practice, the dephasing due to static field inhomogeneities is distinguished from the rapidly varying ones. The former leads to an additional dephasing of the magnetization ( $T_2'$ ). The overall relaxation observed  $T_2^*$  is defined as:

$$\frac{1}{T_2^*} = \frac{1}{T_2} + \frac{1}{T_2'} \quad (1.11)$$

The loss of transverse magnetization  $T_2'$ , which is both device and sample dependent, is recoverable in theory, thanks to the spin echo phenomenon, which will be described in Section 1.2.5. The intrinsic  $T_2$  losses however are not recoverable as they are related to local random time-dependent field variation. The relaxation parameter  $T_2$  is on the order of tens of milliseconds for protons in human tissues. Solids have much shorter  $T_2$  than liquids. Table 1.1 provides several  $T_1$  and  $T_2$  values of the human brain tissues at 7 Tesla ([Rooney et al., 2007](#); [Visser et al., 2010](#)):

Tissue	$T_1$ (ms)	$T_2$ (ms)
Gray Matter (GM)	2132±103	55±4
White Matter (WM)	1220±36	46±2
Cerebrospinal fluid (CSF)	4425±137	~2300

**Table 1.1:** Several  $T_1$  and  $T_2$  values of the human brain tissues measured at 7 Tesla, with mean ± standard deviation (SD).

#### 1.1.4. The NMR signal

The previous sections briefly explained how an ensemble of protons immersed in a magnetic field may be excited, and the mechanisms that allow it to relax back to equilibrium. However, in order to exploit this behavior in the framework of NMR, a measurable signal needs to be extracted. As discussed above, the magnetization can be rotated away from the  $B_0$  axis by applying a RF magnetic field for a short time (i.e. an RF pulse). This pulse is produced by a nearby ‘transmit’ coil tuned at the Larmor frequency. Following this RF excitation, the magnetic moment precesses in the transverse plane at the Larmor frequency. Considering now a ‘receive’ coil placed close to the sample, the rotating magnetic field of the nuclear

magnetization thus generated induces an electromotive force (EMF) in the coil (Hoult and Bhakar, 1997), a consequence of Faraday's law, given by:

$$\text{EMF} = \oint \frac{d}{dt} (\mathbf{M}_T \cdot \mathbf{B}_1^-) d^3r \quad (1.12)$$

$B_1^-$  being the static field produced by the receive coil per unit current. Since the induced EMF is proportional to the field produced by the oscillating magnetic moment, a suitable analog-to-digital converter (ADC) may be used to observe the time evolution of the system and facilitate subsequent computerized post-processing. Because the current induced in the receive coil is directly proportional to the transverse magnetization, the loss of coherence due to  $T_2^*$  relaxation will result in the recording of an attenuated signal. This measurement corresponds to what is commonly referred to as the free induction decay (FID) (Hahn, 1950a). Due to this Faraday's law, and from previous equations, it follows that the signal from an MR experiment will depend on the square of the static magnetic field:

$$\text{Signal} \propto \frac{\gamma^3 B_0^2 \rho_0}{T} \quad (1.13)$$

This is why the interest in higher fields stems from the growth of the signal with field strength, this will be the subject of Section 1.4.

## 1.2. Magnetic Resonance Imaging

### 1.2.1. Principle

In 1952, the first transitional steps from NMR to MRI were reported by Herman Carr in his PhD thesis, where he produced a one-dimensional MRI image (Carr, 1952). His technique was later extended by Paul Lauterbur in 1973. Lauterbur published the first 2D MRI image (Lauterbur, 1973) and the first cross-sectional image of a living mouse in January 1974. These experiments were still performed using a standard NMR spectrometer with an added field gradient, thus introducing the concept of frequency encoding (Figure 1.1). The key goal of this imaging technique is thus to correlate a series of signal measurements with the spatial locations of the various sources. The inversion of the signal is greatly facilitated through a connection to Fourier transforms. With more gradient coils, data reconstruction by inverse Fourier transformation can be carried in more spatial dimensions and enable two- and three-

dimensional imaging. These much faster imaging techniques involving multiple linear field gradients were pioneered by Peter Mansfield in the 1970s (Mansfield and Maudsley, 1977; Mansfield, 1977). These techniques are closer to what is now common practice, rather than the projection technique originally used by Lauterbur. Raymond Damadian, along with Larry Minkoff and Michael Goldsmith, performed the first MRI body scan of a human being on July 3, 1977. The first MRI systems dedicated to healthcare were available at the beginning of the 1980s and spread rapidly worldwide (Sijbers et al., 1996). Diffusion MRI (dMRI) came into existence in the mid-1980s and allows the mapping of the diffusion process of molecules (mainly water) in living biological tissues (Le Bihan and Breton, 1985). Functional MRI (fMRI), which emerged in the 1990s, measures brain activity by detecting associated changes in blood flow (Ogawa et al., 1990). At the beginning of the year 2014, more than 40 UHF MRI scanners (7 Tesla and above) are installed in the world.

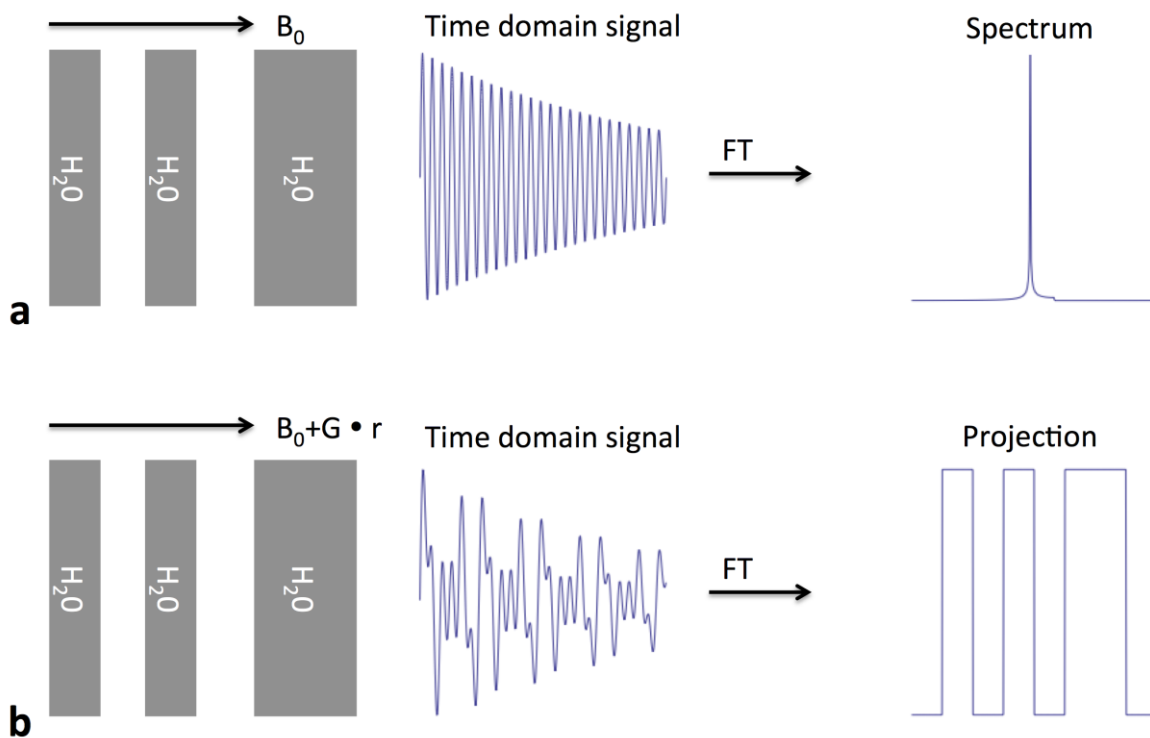


**Figure 1.1:** Frequency encoding in MRI (Cloos, 2012). **a:** Three compartments filled with water immersed in a static magnetic field  $B_0$  result in a FID whose spectrum shows the Larmor frequencies present in the sample, e.g., a single proton peak in this case. **b:** Same compartments with position  $r$  immersed in a linear field gradient  $G$  on top of the static magnetic field result in a FID with a range of resonance frequencies. Each frequency in the spectrum corresponds to a spatial location along the direction of the gradient. Thus, the spectrum gives a projection of the imaged object after Fourier Transform.

### 1.2.2. MRI hardware

Most current clinical MRI systems use superconducting electromagnets, which work continuously and consist of a superconductive coils cooled by liquid helium. They produce strong, homogeneous magnetic fields, but are expensive and require regular maintenance. In the event of loss of superconductivity, electrical energy is instantly dissipated as heat. This heating causes a rapid boil-off of the liquid Helium (a quench). To reduce the stray field strength, the device has a shielding system that is either passive (metallic) or active (an outer superconducting coil whose field opposes that of the inner coil).

Gradient coils, placed in each spatial direction, produce linear variations in magnetic field intensity in three directions of space. They modify the spin resonance frequency according to the position in the sample and in proportion to their current. This variation in Larmor frequency also causes a dispersion of spin phases. Gradient performances are linked to their maximal amplitude (in mT/m), which determines maximal spatial resolution (slice thickness and field of view), their slew rate, corresponding to their switching speed, and their linearity. The rapid switching of the gradients induces currents in the conducting materials in the vicinity of the gradient coils. These so-called Eddy currents will oppose the gradient fields and distort the desired patterns. Pre-emphasis can be used to reduce their effect. Last, gradient switches produce Lorentz forces causing vibrations in the gradient coils and their supports. These vibrations are the main source of the characteristic MRI noise.

The radiofrequency system comprises the set of components for transmitting and receiving the radiofrequency waves involved in exciting the spins. In transmission, the goal is to deliver uniform excitation throughout the scanned volume. On reception, the coils must be as sensitive as possible. Last, as the resonance frequency of protons is very close to that of the radio waves used in radio broadcasting and the FM band, the MR device is therefore placed in a Faraday cage to insulate it from external RF signals which could pollute the signal. A brief depiction of an MRI system is provided in Figure 1.2.



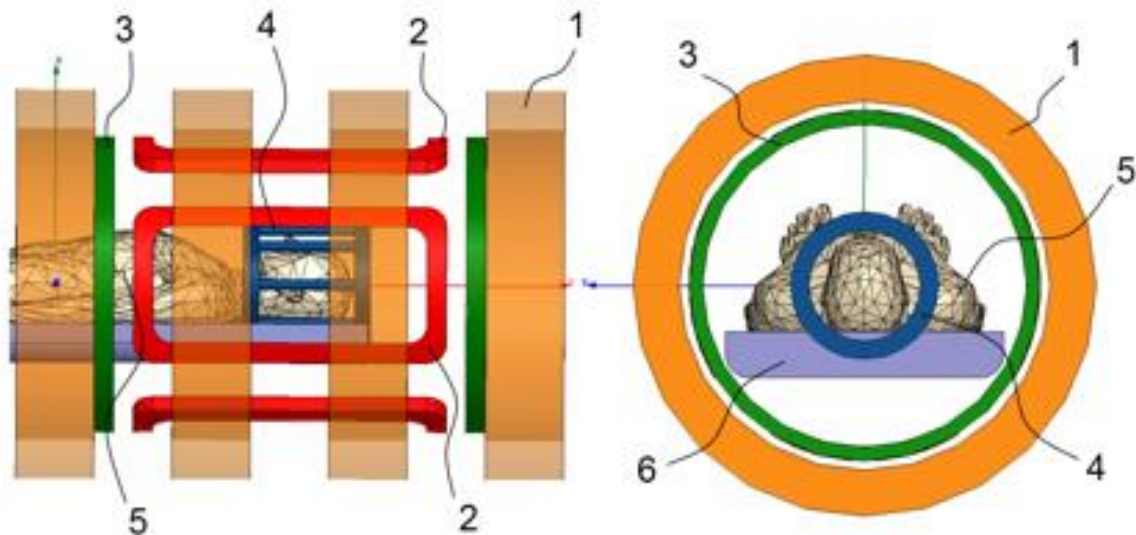


**Figure 1.2:** Schematic overview of a current MRI system (Cloos, 2012). **1:** The main superconducting magnet cooled with liquid helium, responsible for the static magnetic field in the z-direction ( $B_0$ ). **2:** Gradient coils used to produce linear field gradients along the x and y direction through the subject (in a limited region of interest). **3:** Gradient coils used to produce linear field gradients along the z-axis. **4:** Head coil used for RF excitation and NMR signal reception. Many clinical systems are also equipped with a larger RF transmission coil for whole body applications (not shown), comparable in size to the gradient coil diameter. **5:** Subject. **6:** Patient table.

### 1.2.3. MRI signal acquisition & contrast

As previously described, the NMR signal is extracted after at least one RF excitation (or possibly more depending on the MRI sequence considered). Imaging gradients during the ADC readout enable frequency encoding, as multiple frequencies are introduced into the FID dependent on the location of the source. The same encoding principle is used with transverse phase for 2D and 3D imaging. Once the spins are excited, they are left free to precess and relax, and then the signal is acquired around an “Echo Time” (TE). Last, the excitation is repeated at a “Repetition Time” (TR) to image another section of k-space.

Since the tissues of the human body have different  $T_1$  and  $T_2$  parameters, the two imaging parameters TE and TR determine the value of both transverse and longitudinal magnetizations of the different tissues when the signal is acquired. In that way, MRI images have a specific “weighting”, depending on which relaxation parameter is emphasized. Usually, when the FA is not too low:

- A short TR and a short TE give a  $T_1$ -weighted image.
- A long TR and long TE give a  $T_2^*$ -weighted image.
- A long TR and short TE give a proton density (PD-weighted) image, that is to say, little influenced by  $T_1$  and  $T_2$ .

A substance with long  $T_1$  and long  $T_2$  (e.g. the cerebrospinal fluid, CSF) will give a hypo-intense  $T_1$ -weighted signal and a hyper-intense  $T_2$ -weighted signal.

There are two basic acquisition schemes to cover a volume of interest: 2D and 3D, yet MRI sequences can have different strategies to fill k-space. The 3D acquisition strategy generally implies that the whole volume within the coil sensitivity range is excited before spatial encoding. As a result, a 3D k-space needs to be filled, with one read-out direction and two phase-encoding directions. However, the most common approach in MRI (and the historical one) is in fact the selective excitation of a single slice prior to 2D imaging. Stacking adjacent slices then allows the reconstruction of the 3D volume of interest. Nevertheless, the main advantages of 3D acquisitions are a high SNR, as the whole volume contributes to signal, and the possibility of achieving high isotropic resolution. Indeed, in multi-slice 2D mode, the slice thickness is limited by the gradient strength and excitation duration, and the thinner the slice, the lower the signal as well. However, being able to excite and image only a part of the attainable volume also presents clear advantages. One may not be interested in imaging the whole volume, and selecting only a given spatial location leads to considerable gain in scan time while removing aliasing concerns in the selection direction. 2D and 3D acquisitions will be both addressed in the following sections. Yet, remembering the aim of this work is the design of non-selective excitation, only the 3D acquisition strategies will be considered later.

#### **1.2.4. MRI sequences**

An MRI sequence is a preselected set of defined RF and gradient pulses, usually repeated many times during a scan, wherein the time interval between pulses and the amplitude and shape of the gradient waveforms will control NMR signal reception and affect the characteristics of the MR images. Over the years, a plethora of imaging methods has been introduced. The several MRI sequences discussed in this thesis are depicted in Figure 1.3, as part of two categories: the Gradient-Recalled-Echo (GRE) and the Spin-Echo (SE):

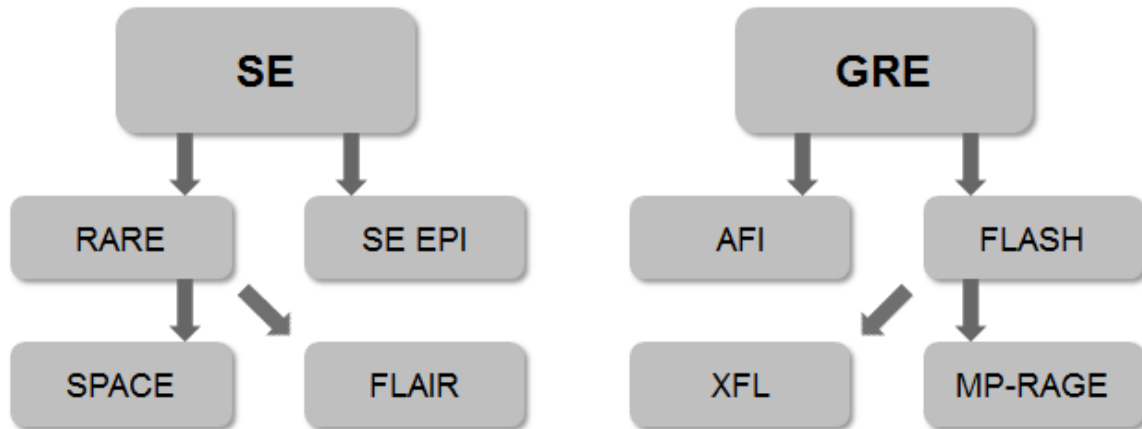


**Figure 1.3:** Overview of several MRI sequences addressed in this thesis. SE ([Hahn, 1950b](#)), EPI ([Mansfield, 1977](#)), RARE/FSE/TSE ([Hennig et al., 1986](#)), FLAIR ([Hajnal et al., 1992a](#)), SPACE ([Mugler, 2000](#)), GRE ([Frahm et al., 1986](#)), FLASH ([Haase et al., 1986](#)), AFI ([Yarnykh, 2007](#)), MP-RAGE ([Mugler and Brookeman, 1990](#)), XFL ([Fautz et al., 2008](#); [Amadon et al., 2012](#)). All these acronyms are detailed in the Nomenclature. For a more complete review of all the different imaging techniques, the reader is directed to one of the numerous textbooks such as ([Bernstein et al., 2004](#)).

After a short explanation of how the GRE sequence ([Frahm et al., 1986](#)) works in the context of a volumetric acquisition and how EPI readout ([Mansfield, 1977](#)) can accelerate acquisition, a more precise description of imaging sequences in the framework of the spin echo phenomenon is given: first the SE phenomenon and the related MRI sequence are studied; then following the research advances achieved in the past decades, several imaging techniques will be presented: RARE ([Hennig, 1988](#); [Hennig et al., 1986](#); [Hennig, 2000](#)), FSE/TSE ([Constable et al., 1992](#)), Hyperechoes ([Hennig and Scheffler, 2001](#)), TRAPS ([Hennig et al., 2003](#)), SPACE ([Mugler, 2000](#); [Busse et al., 2006](#)), FLAIR ([Hajnal et al., 1992a, 1992b](#)) and DIR ([Bydder and Young, 1985](#); [Madelin et al., 2010](#)).

In a GRE sequence (Figure 1.5.a) the excitation pulse tilts the magnetization by a flip angle typically between  $0^\circ$  and  $90^\circ$ . The data are sampled during a gradient echo, which is achieved by dephasing the spins with a gradient before they are rephased by a gradient with opposite polarity to generate the echo. The signal generated by a gradient echo depends on the longitudinal magnetization and the flip angle. Additional gradients and RF pulse phase shifts may be introduced in order to spoil the transverse magnetization ([Epstein et al., 1996](#)). GRE usually have a low SAR and are sensitive to field inhomogeneities.

EPI ([Stehling et al., 1991](#); [Turner et al., 1991](#)) is an ultrafast MRI pulse sequence, vastly used in diffusion imaging ([Turner et al., 1990](#)), real-time imaging ([Uecker et al., 2010](#)) and

fMRI (Kwong et al., 1992). EPI employs a series of bipolar readout gradients to generate a train of gradient echoes and thus produces an image in only a few tens of milliseconds with modern gradient hardware. Since no additional RF is needed, images are produced really fast and with an adapted phase-encoding gradient, multiple lines of k-space can be filled in a single shot. However, EPI is more prone to a variety of artifacts (Yang et al., 1998; Zakhor et al., 1991) and is not really used in 3D imaging.

### 1.2.5. Spin echo-based MRI sequences

A Spin Echo (Figure 1.4) is the refocusing of the magnetization vector by a  $180^\circ$  rotation RF pulse. For a given population of spins, the NMR signal observed following an initial excitation pulse decays with time due to both intrinsic spin  $T_2$  relaxation and by external field inhomogeneities which cause different spins in the sample to precess at different rates. The inhomogeneous static dephasing can be removed by applying this  $180^\circ$  refocusing pulse. If the refocusing pulse is applied after a period  $t$  of dephasing, the phase will rewind to form an echo at time  $2t$ . The intensity of the echo relative to the initial signal is given by  $e^{-2t/T_2}$ .

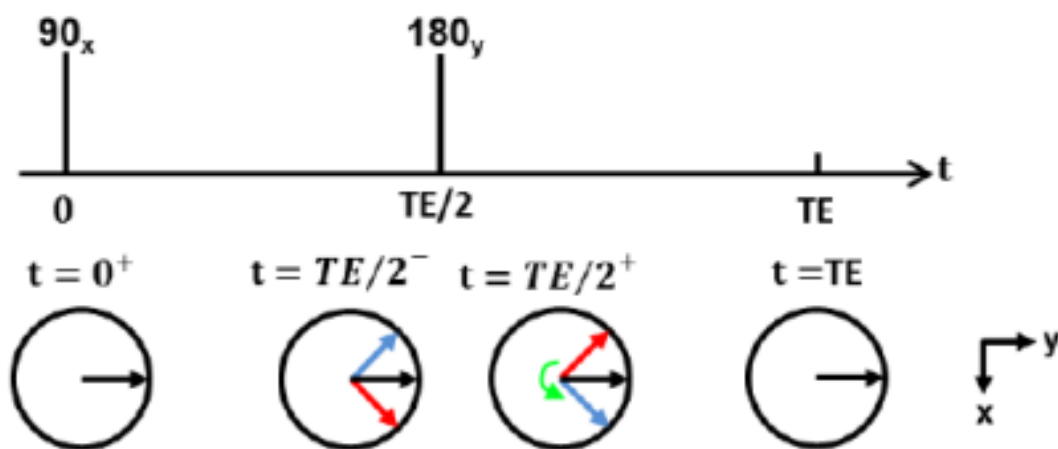


**Figure 1.4:** The Spin Echo (SE) phenomenon (Hahn, 1950b). Following a  $90^\circ$  excitation along the x-axis, magnetization is flipped along the y-axis in the transverse plane. The spins gradually dephase due to local magnetic field inhomogeneities. The red spin has a phase advance and the blue spin a phase delay. By applying a  $180^\circ$  flip angle pulse oriented along the y-axis at  $t = TE/2$ , the magnetization configuration is flipped (green arrow) so that the phase of the magnetization is negated with respect to the phase of the refocusing pulse. Progressively, the phases slowly rewind and come back in coherence. Complete refocusing

occurs at  $t=TE$  on the y-axis. An accurate  $T_2$  echo can be measured with all  $T_2'$  effects removed.

The main advantage of a SE pulse sequence (Figure 1.5.b) is its ability to obtain a specific contrast weighting ( $T_1$ ,  $T_2$ , PD) (Hendrick, 1999) depending on TE and TR, as described in Section 1.2.3. Because the SE signal decays with  $T_2$  (and not  $T_2^*$ ), it enables the use of longer TE values than GRE sequences. From the clinical point of view, diseased tissue often contains more free water than healthy tissue, leading to a longer  $T_2$ . This is why  $T_2$ -weighted images are sought to enhance their visibility. SE images are typically obtained in 2D, so that the interleaved acquisition strategy can be used.

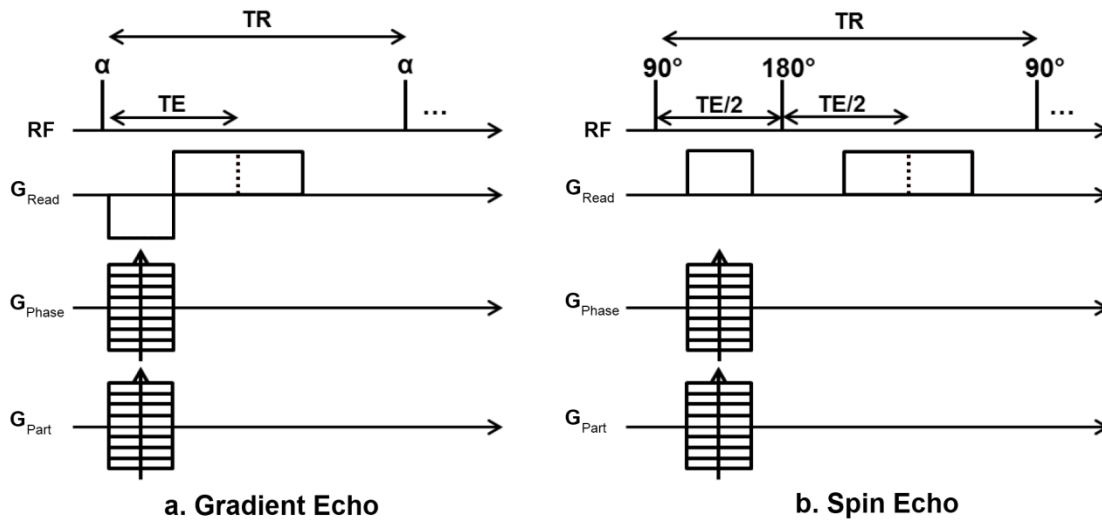


**Figure 1.5:** **a.** The Gradient Echo (GRE) sequence chronogram. The echo is formed when the gradient momentum is zero. **b.** The Spin Echo (SE) sequence chronogram. A refocusing pulse is placed between excitation and signal acquisition. For both sequences, signal acquisition is 3D Cartesian. The arrows indicate how the phase-encoding gradient amplitude changes successively to sample the whole k-space.

SE images can be acquired with either a single-echo or a multiple-echo (Feinberg et al., 1985) pulse sequence, depending on the number of RF refocusing pulses that are applied in each TR interval. Because the signal decays exponentially, the number of useful echoes in the echo train is limited. In that case, each echo fills its own independent k-space and contributes to an independent image. In that way, several contrasts (PD and  $T_2$  for instance) can be achieved simultaneously. Yet, k-space is filled one line at a time, making the acquisition time too long for clinical  $T_2$ -weighted 3D imaging.

### 1.2.6. Turbo Spin Echo-based MRI sequences

As explained in Section 1.1.3, transverse magnetization lifetime is governed by spin-spin relaxation time  $T_2$ . In the case of a single-echo SE sequence, data is thus acquired only for a small fraction of this lifetime and the considerable portion of the signal that can be potentially acquired before and after this acquisition window is therefore wasted. Yet, as long as some transverse magnetization remains, additional  $180^\circ$  refocusing pulses could be added to form a train of spin echoes, acquiring more data.

Rapid Acquisition with Relaxation Enhancement (RARE), is a fast imaging sequence that employs an RF excitation pulse followed by a train of refocusing pulses to produce multiple RF spin echoes (Hennig et al., 1986). Each echo is distinctively spatially encoded so that multiple k-space lines can be sampled following each excitation pulse. RARE can be used in either 2D or 3D acquisition mode and is compatible with virtually all k-space sampling strategies, including rectilinear Fourier (Hennig et al., 1986) and spiral (Pauly et al., 1993) imaging.

Especially when dealing with  $T_2$ -weighed imaging (i.e. when long TR are considered), RARE provides considerable time savings compared to conventional SE sequences. This MRI sequence is therefore a great candidate in clinical settings, with similar or even better scan-time and less sensitivity to off-resonance effects than EPI or GRASE (Oshio and Feinberg, 1991). On the other hand, the major drawbacks of RARE include increased RF power deposition (due to the multiple  $180^\circ$  pulses of the echo train, which is especially problematic at UHF) (Hennig et al., 2003) and blurring (because high frequencies are often acquired at the end of the echo train where signal is low) (Alsop, 1997). Since the initial introduction of RARE, a number of variations and modifications of the sequence have been developed. Along with these developments, many names appeared, including Fast-Spin-Echo (FSE), Turbo-Spin-Echo (TSE), and others (Constable et al., 1992; Le Roux and Hinks, 1993). A chronogram of the RARE sequence is provided in Figure 1.6.

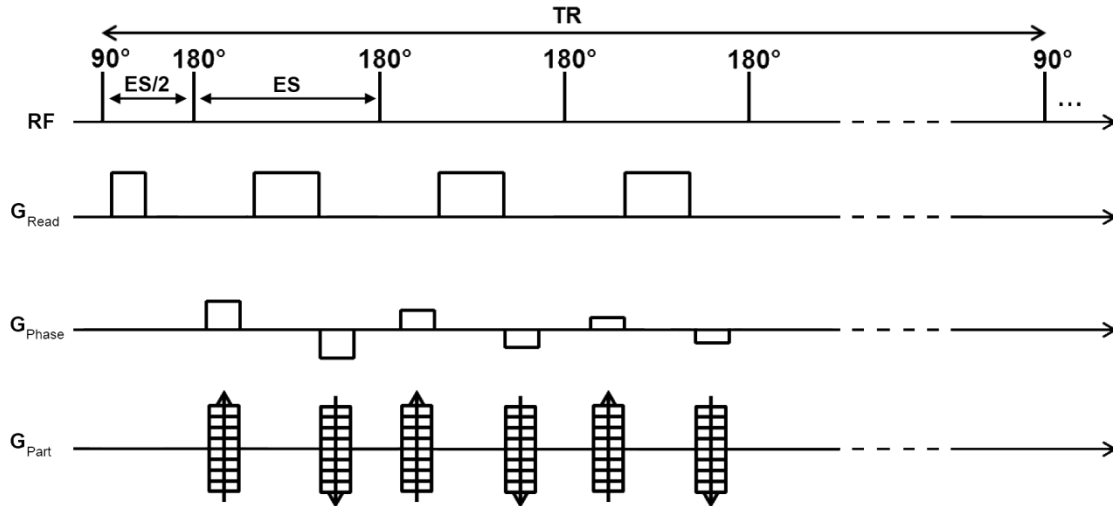


**Figure 1.6:** The RARE sequence chronogram (3D rectilinear Fourier imaging). A slab is selected by the  $90^\circ_x$  excitation pulse. Refocusing pulses ( $180^\circ_y$ ) are not selective. The primary phase encoding is performed during the echo train, whereas secondary phase encoding is performed every TR. For both, phase-rewinding gradients follow the readout gradient. Crusher gradients surrounding the RF refocusing pulses (not represented here) in readout and partition directions are used to cut undesired FIDs.

The Echo Train Length (ETL) is the number of RF refocusing pulses, corresponding to the number of signal echoes that could be sampled in one TR. It determines the scan-time reduction compared to conventional SE sequences. Maximal ETL is practically determined by  $T_2$  relaxation time and the interval between two consecutive spin echoes. The latter being known as the Echo Spacing (ES), is limited by RF pulses duration, SAR and gradient specificities. Non selective refocusing pulses shorten ES, which allows a longer ETL to be used. The readout gradient waveforms of RARE are identical to SE's ones. Phase encoding throughout the echo train can be performed along either the primary ( $k_y$ ) or the secondary ( $k_z$ ) phase-encoded directions. The phase encoding in the other direction is accomplished at the rate of one step per TR interval. But because each refocusing pulse negates the accumulated phase of the spin echo, the secondary phase-encoding step will alternate sign throughout the echo train (i.e.  $-k_z, k_z, -k_z, k_z$ , etc.). Thus, an extra step is required to sort the 3D k-space data and confine all  $k_y$  lines in the same  $k_z$  plane. An additional problem with this approach is that the phase-encoding value of the stimulated echoes does not coincide with the one of the primary spin echoes, causing image artifacts. To solve both issues, gradient waveform along the partition direction includes series of phase-encoding/phase-rewinding paired lobes for each echo, similar to those used in the phase direction, except that lobe

areas remain the same throughout one echo train. Crusher gradients surrounding the RF refocusing pulses in readout and partition directions are used to cut undesired FIDs. Depending on the number of independent RF excitation pulses used to sample k-space, RARE/TSE/FSE can be single-shot, where the entire k-space is acquired with one excitation, or multi-shot, where only fractions of k-space are acquired with each shot.

The intervals between the refocusing pulses are twice as long as the time between the excitation and the first refocusing pulse. To reduce accumulating effects of imperfections of the  $180^\circ$  pulses, a  $\pi/2$  phase shift between the excitation pulse and the subsequent refocusing pulses is commonly set. This timing and phase relationship of the RF echo train is known as the “Carr-Purcell-Meiboom-Gill” (CPMG) condition ([Carr and Purcell, 1954](#); [Meiboom and Gill, 1958](#)). This condition is crucial when considering variable flip angle Turbo Spin Echo-based MRI sequences and will be explained in the subsequent section.

There has been a growing interest for isotropic 3D acquisitions over the years. Indeed, such acquisitions do not have the partial volume issues typically related to slice thickness in 2D multi-slice acquisitions. Thus they allow the observation of lesions in any direction, which is particularly interesting for several structures. Yet, high-resolution 3D TSE sequences are still long. Indeed, the decay of the signal after the excitation pulse is too fast to authorize the acquisition of more than several dozen echoes for one repetition. Under these conditions, even when using parallel imaging acceleration factors, it is not possible to obtain images with a high isotropic resolution in less than 60 minutes. To address this  $T_2$ -weighted 3D imaging acquisition time challenge, longer echo train pulse sequences need to be considered, with alternative strategies to keep the transverse magnetization at a measurable level for a period of time larger than  $T_2$ .

### **1.2.7. Variable Flip Angle Turbo Spin Echo-based MRI sequences**

As explained before, high-resolution 3D acquisitions enable precise characterization and localization of anatomy and pathology, but acquisition times are prohibitively long, so  $T_2$ -weighted sequences are usually only viable in 2D mode. Acquisition speed is limited by the length of the echo train and very long echo trains are generally not possible due to loss of contrast and blurring. Latter developments on the RARE sequence thus focused on reducing the flip angle of all the refocusing pulses, as a useful mean of addressing high RF power deposition, and extending the duration of the echo train limited by the  $T_2$  decay, in order to accelerate acquisition times.

The first approach consisted in applying the same reduced flip angle for the refocusing pulses ([Hennig, 1988](#)). In that case, the transverse magnetization is partially tipped onto the



longitudinal axis, partially refocused as usual, and partially left intact. Similarly, the longitudinal magnetization is partially excited to the transverse plane, partially inverted and partially left along the longitudinal axis. Each of these magnetization components is further divided following the subsequent non-180° refocusing pulse. The transverse magnetization component continues to accumulate phase until it is affected by the next RF pulse. The phase evolution of the magnetization is depicted in an Extended Phase Graph (EPG), provided in Figure 1.7 with detailed explanations.

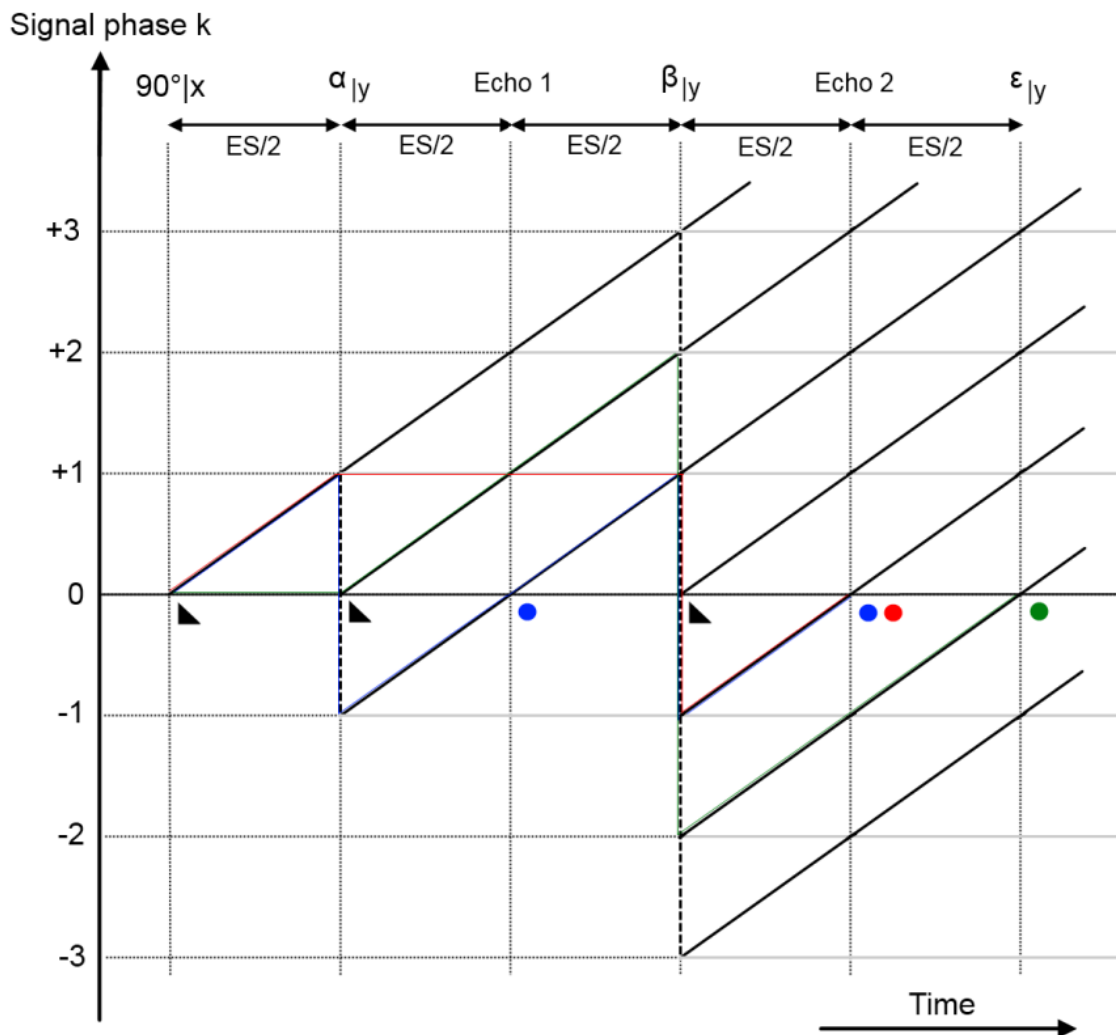


**Figure 1.7:** RF refocusing pulse train and its associated Extended Phase Graph (EPG). Each line represents a particular pathway of a magnetization component. These pathways are often referred to as signal pathways or signal coherence pathways. The effect of imaging gradients is not considered here, thus only  $B_0$  field inhomogeneities induce phase accumulation. Horizontal lines (gray) represent longitudinal magnetization, vertical lines (dashed) indicate phase reversal, and diagonal lines (solid) denote the phase accumulation

of the transverse magnetization. Whenever the phase of a coherence pathway crosses zero, an echo is produced. If a coherence pathway experiences a phase reversal at every refocusing pulse, the echoes it generates are primary spin echoes (blue circles). If a coherence pathway is initially in the transverse plane after the excitation, an  $\alpha$ -pulse brings one of its components on the longitudinal axis, and a second  $\beta$ -pulse further reverses it, giving rise to a stimulated echo (red circle). If a coherence pathway is initially along the longitudinal axis, it accumulates phase in the transverse plane after the  $\alpha$ -pulse and is likewise further reversed by the  $\beta$ -pulse to create a secondary spin echo (green circle). FIDs produced are denoted as black triangles. Both FIDs and secondary spin echoes are usually eliminated by crusher gradients.

As more non- $180^\circ$  refocusing pulses are included, the number of echoes increases. These echoes produced by various coherence pathways are generally not in phase and can cause signal cancellation. Therefore, it is crucial to design the sequence to ensure that echoes only occur at the desired temporal positions with similar phase. The CPMG condition ([Carr and Purcell, 1954](#); [Meiboom and Gill, 1958](#)) is a set of three conditions to ensure that these two requirements are met:

**Condition 1:** The refocusing pulses must be  $90^\circ$  out of phase with respect to the excitation pulse, and evenly positioned with equal spacing between any two consecutive pulses, this spacing must be twice the one between the excitation pulse and the first refocusing pulse.

**Condition 2:** The phase accumulated by a spin isochromat between any two consecutive refocusing pulses must be equal.

**Condition 3:** If a pulse has a non-uniform yet smooth phase distribution across the sample, then all other pulses must share the same phase pattern to fulfill everywhere both condition 1 and 2.

Reduced flip angle refocusing approaches lengthen the usable echo train length, since the complex combination of spin and stimulated echoes introduces  $T_1$  dependence to the signal evolution. Significantly reduced SAR at comparable SNR can be obtained using a variable flip angle pulse train designed to produce constant echo amplitude ([Alsop, 1997](#); [Le Roux and Hinks, 1993](#)). The spin echo amplitude approaches a temporary steady state which then slowly decays due to  $T_1$  and  $T_2$  relaxation. Because this “steady state” is actually only temporary, it will be referred to as a Pseudosteady State (PSS). The empirically determined pseudosteady state echo amplitude is well approximated by the sine of half the refocusing flip angle ([Alsop, 1997](#)). A method for optimizing the flip angles of the first few refocusing pulses to achieve a constant amplitude echo train was presented in ([Le Roux and Hinks,](#)

1993). It demonstrated that beginning the RF pulse train with higher amplitude pulses that slowly decrease and approach a constant, or asymptotic, flip angle can produce constant echo amplitude from the very first echo.

Among the other strategies employed to manipulate signal along a very long echo train one could also cite Hyperechoes (Hennig and Scheffler, 2001) or TRAPS (Hennig et al., 2003), which enable the central line of k-space to be acquired with full signal strength.

A different approach using variable flip angles has been suggested for 3D applications (Mugler, 2000). By keeping the refocusing angle below  $100^\circ$ , the fractional  $T_2$  contribution is kept low and magnetization is efficiently stored in stimulated echo pathways. This allows quite long echo trains at the cost of some penalty in signal intensity. The increased contribution of stimulated echoes combined with the use of very long echo trains will also lead to a somewhat reduced  $T_2$  contrast (Hennig et al., 2003). It is therefore possible to obtain an almost constant signal from the tissue of interest for the main part of the signal acquisition, by using prescribed signal evolutions which include relaxation effects in the calculation of refocusing flip angles. Flip angles need to be optimized for only one tissue of interest as the prescribed signal evolutions depend only weakly on the  $T_1$  and  $T_2$  relaxation times and are therefore similar for many other tissues. Using an initial exponential decay, a constant and then another exponential decay for the prescribed signal evolution produces images in which the contrast is quite similar to those obtained using conventional  $T_2$ -weighted Spin Echo sequences. This approach allows very long echo trains and 3D imaging, since the effective  $T_2$  of the echo train is longer than physical  $T_2$  for tissues with long  $T_1$ s ( $\geq 10 T_2$ ). In this way, acquisition times can be commensurately reduced, or sequence resolution increased. “ $T_2$ -weighted” 3D whole brain images with low SAR values thus can be acquired with echo train lengths of up to 250 echoes.

The Variable Flip Angle Turbo Spin Echo (VFA TSE) sequence, also called the SPACE sequence, for: Sampling Perfection with Application optimized Contrasts using different flip angle Evolution (Siemens manufacturer), is the MRI sequence born from this formalism. This acronym will be subsequently used in this manuscript. In the SPACE sequence, an excitation pulse is used followed by a long variable angle refocusing pulse train acquiring multiple k-space lines per TR, as each echo is distinctively spatially encoded. Careful adjustment of the targeted angles and the echo spacing between the acquisition blocks, as well as the usual imaging parameters, allow excellent contrast between gray matter (GM), white matter (WM) and Cerebrospinal fluid (CSF) (Busse et al., 2006). Other names of the sequence depend on the manufacturer: CUBE for General Electric and VISTA for Phillips. A chronogram of the sequence is provided in Figure 1.8.

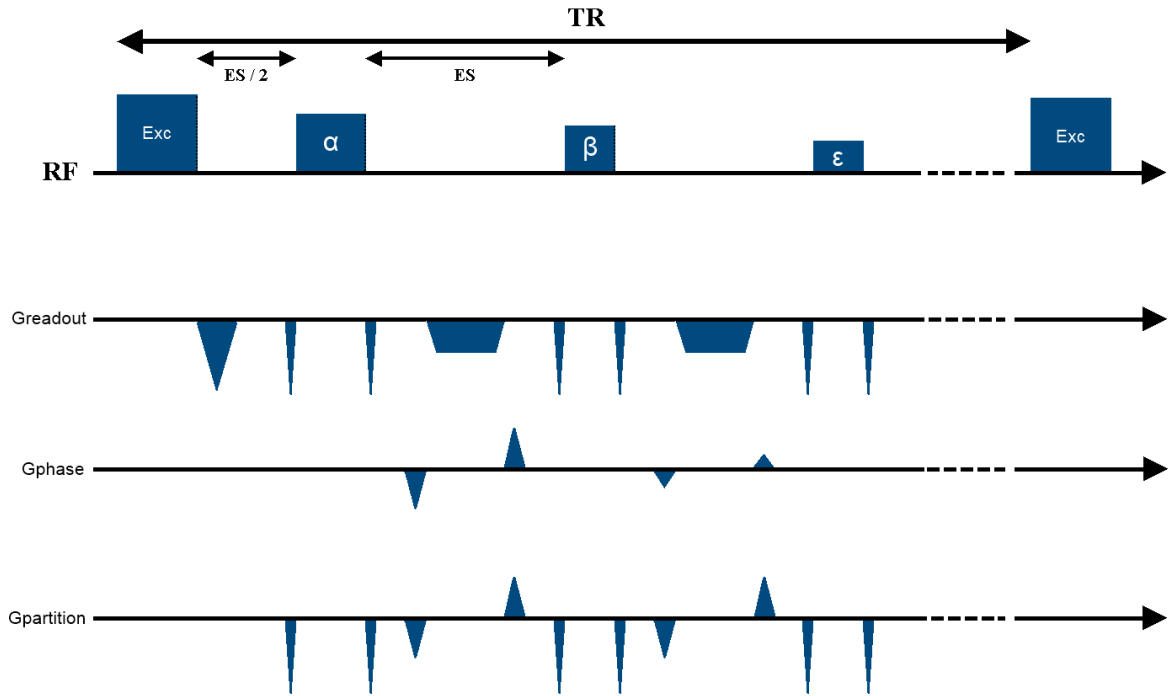


**Figure 1.8:** The SPACE sequence chronogram (3D rectilinear Fourier imaging). A slab is selected by the  $90^\circ|_x$  excitation pulse. Refocusing pulses ( $\alpha|_y$ ,  $\beta|_y$ ,  $\epsilon|_y$ , etc.) whose rotation angle values are determined by the EPG formalism, are not selective. The primary phase encoding is performed during the echo train, whereas secondary phase encoding is performed every TR. For both, phase-rewinding gradients follow the readout gradient. Crusher gradients surrounding the RF refocusing pulses in readout and partition direction are used to cut undesired FIDs.

The hyperintense fluid signal in  $T_2$ -weighted images often complicates the detection of lesions with long  $T_2$ s, such as edemas surrounding brain tumors, or multiple sclerosis plaques. CSF signal can be nulled using the inversion-recovery phenomenon, because its  $T_1$  value is very high. Based on the RARE sequence, the fluid-attenuated inversion recovery (FLAIR) sequence ([Hajnal et al., 1992a, 1992b](#)) has become the key sequence for imaging pathologies in the central nervous system, including vascular diseases, multiple sclerosis, tumors, and degenerative diseases ([Bachmann et al., 2006](#)). The current drive toward detection of subcortical and intracortical lesions in multiple sclerosis and epilepsy requires images with sub-millimeter resolution in three dimensions, with high SNR and good contrast ([Mainero et al., 2009; de Graaf et al., 2012](#)). The intrinsic high SNR and good parallel imaging properties of UHF MRI have the potential to fulfill these requirements ([Visser et al., 2010; Zwanenburg et al., 2010](#)). Yet, this MRI sequence is particularly prone to the disadvantages of UHF (described in Section 1.4.2), including the lengthening of  $T_1$  constants

of GM and WM while the  $T_1$  of the CSF is relatively field independent, the increased inhomogeneity of the RF transmit field  $B_1^+$  and the constraints on the maximum allowed SAR which limits the use of high refocusing flip angles and adiabatic pulses for inversion.

The Double Inversion Recovery (DIR) (Bydder and Young, 1985; Madelin et al., 2010) MRI sequence combines two inversion pulses in order to simultaneously suppress signals from tissues with different longitudinal relaxation times. For the brain, DIR allows to selectively image GM by nulling the signal from WM and CSF at the time of the excitation pulse. Imaging GM structures is important in the study of many neurological disorders such as Alzheimer's disease, epilepsy and multiple sclerosis (Madelin et al., 2010). The loss of SNR due to the longitudinal magnetization preparation could be counteracted by the implementation of DIR on high field scanners, adopting a careful modification of sequence parameters.

Both FLAIR and DIR sequences can benefit from a variable flip angle turbo spin echo train of RF refocusing pulses. The implementations of the SPACE and FLAIR sequences with such an echo train, in a parallel-transmission setup at 7 Tesla, are addressed in Chapter 7.

## 1.3. Specific Absorption Rate

### 1.3.1. Definition

During an MRI exam, radiofrequency waves are transmitted to acquire images of a subject. These RF waves deposit energy into the tissues, resulting in an increase of temperature that could potentially lead to tissue damage. Therefore, regulation committees provide guidelines indicating the maximum allowed energy deposition in human subjects in the case of non-ionizing radiations (IEC, 2010). These guidelines refer to the energy deposition as the Specific Absorption Rate (SAR), given locally by:

$$SAR(r) = \frac{1}{T} \frac{\sigma(r)}{2\rho(r)} \int_0^T \|E(r,t)\|_2^2 dt \quad (1.14)$$

This power is expressed in W/kg and depends on the conductivity  $\sigma(r)$ , the density  $\rho(r)$ , the electric field distribution  $E(r,t)$  inside the subject, and the time of integration  $T$  during which instantaneous energy deposition is averaged.

### 1.3.2. Guidelines

The International Electrotechnical Commission (IEC) guidelines ([IEC, 2010](#)) refer to a set of 4 limits considering the maximum allowed energy deposition in the human head. These limits pertain to the global SAR, i.e. the SAR averaged over the entire head, and the local SAR, defined as the SAR averaged over any closed 10-g volume of tissue. The 4 limits provided by the guidelines consider both the T=10-second average and T=6-minute average. The following table provides a summary of the SAR limits as defined for diagnosis experiments exposing the human head to an RF field:

IEC 2010	10-s averaged	6-min averaged
Local SAR	20 W/kg	10 W/kg
Global SAR	6.4 W/kg	3.2 W/kg

**Table 1.2:** International guidelines on SAR limits acceptable for the human head, given for two spatial and temporal scales ([IEC, 2010](#)).

Remembering that the primary biological parameter of interest is the temperature, to avoid local thermal damage or thermoregulatory problems ([Collins et al., 2004](#)), it is also specified in these guidelines that the localized temperature in the head should never exceed 39 °C, and that care should be taken to limit the temperature rise in the eyes to +1 °C.

Considering the possible health hazard induced by the exposure to RF waves, a solid assessment of the energy sent into the subject tissue through the MRI coil is mandatory. Indeed, some indications of the heating effects from the energy emitted by radio transmitters appeared in the late 1930s. The phenomena became well known with the development of radar during World War II. Quite simply, people noticed that they got warm when they stood in front of radar antennas (which allowed Dr. Percy Spencer to invent the microwave oven). The first human exposure guidelines were developed by the U.S. military in the 1950s. The military funded most of the research at that time because they owned most of the high-power transmitters.

Nowadays, with the blossoming of wireless communications (Internet with WIFI, 4G mobile phones, etc.), fixing relevant guidelines is a public safety issue which should be considered wisely. Regarding the MRI systems case, several specifications like the duration of exposure or the position of the subject in the coil needs to be taken into account. Explanations of how conventional MRI works will be given in the 4<sup>th</sup> Chapter of this manuscript, as well as a dedicated methodology for parallel transmission-enabled MRI systems. In Chapter 5, the relationship between SAR and temperature is studied extensively.

## 1.4. Ultra High Field MRI

### 1.4.1. Advantages

So far, the impact of working with an ultra-high main magnetic field has not been considered in detail for MRI. The advantages of ultra-high field strength for MR imaging are twofold:

- a. Increased Signal-to-Noise-Ratio (SNR), which can be used to increase spatial resolution, to shorten scan time, and/or to enable imaging of low-sensitivity nuclei other than hydrogen.
- b. Enhanced contrast mechanisms such as those based on susceptibility-related effects.

The corresponding challenges associated with UHF MRI include increased inhomogeneity of the static and RF fields (resulting in artifacts in various MRI sequences) and increased RF energy deposition into tissues, as quantified by SAR, which can limit the range of sequence parameters to be employed safely during a clinical scan. These challenges and solutions deployed to mitigate their effects will be described in detail in the next sections.

Despite these challenges, over the years, UHF MRI has been shown to provide unique anatomical, functional and physiologic information beyond just gains in SNR. Enabling better resolution provides new information on very small structures in the brain, breast, torso, pelvic, cardiac, spine and osteoarticular imaging. Last, several imaging modalities such as fMRI, Magnetic Resonance Angiography (MRA), Magnetic Resonance Spectroscopy (MRS) and Magnetic Resonance Microscopy (MRM) have been shown to benefit from higher field strengths.

Demonstrating the first advantage, it can be shown that both the signal-to-noise ratio (SNR) and contrast-to-noise ratio (CNR) are dependent on the field strength. In general for 3D imaging, the SNR is proportional to:

$$\text{SNR} \propto M_0 B_1^- \Delta x \Delta y \Delta z \sqrt{\frac{N_{\text{phase}} N_{\text{partition}} N_{\text{read}} N_{\text{avg}}}{\text{BW}}} f_{\text{seq}}(\text{TR}, \text{TE}, \theta) \quad (1.15)$$

where  $M_0$  is the thermal equilibrium magnetization,  $B_1^-$  the receive sensitivity (RF magnetic field per unit current in the receive coil),  $\Delta x$ ,  $\Delta y$ ,  $\Delta z$  are the spatial dimensions of the voxels,  $N_{\text{phase}}$  the number of phase encoding steps,  $N_{\text{partition}}$  the number of partition encoding steps,  $N_{\text{read}}$  the number of samples in the readout,  $N_{\text{avg}}$  the number of averages, BW is the readout bandwidth, and  $f_{\text{seq}}(\text{TR}, \text{TE}, \theta)$  is a factor dependent on sequence parameters. Therefore,

once receive coils and sequence parameters are adjusted to their optimal performance, the only options left to improve the MR signal are to increase  $M_0$  or decrease the resolution. When high resolution images are desired, the only remaining possibility is to increase magnetization. Looking back at equation (1.3) the net magnetization can be increased in two ways: the temperature of the object under investigation can be reduced or the magnetic field can be increased. When considering living biological tissues, significantly decreasing the temperature is unrealistic, thus leaving only the magnetic field strength as a free parameter. In addition of direct improvement in SNR due to an increased  $M_0$ , pushing up the main magnetic field strength brings other advantages. Most notably are the enhanced  $T_2^*$  contrast, and performance boost when adopting parallel imaging methods (Sodickson and Manning, 1997; Pruessmann et al., 1999; Griswold et al., 2002).

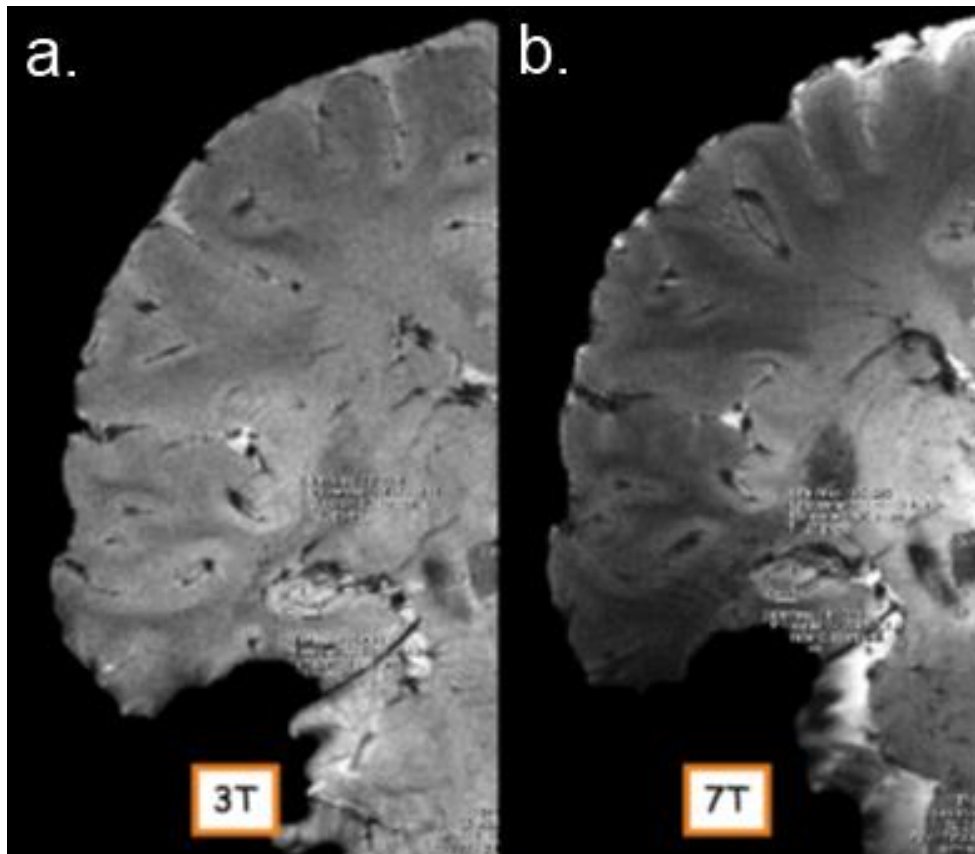


**Figure 1.9:** Comparison of  $T_2^*$ -weighted images of a coronal slice through the brain acquired with a quadrature head coil. CNRs are enhanced for the same acquisition time and the same spatial resolution. **a:** Image acquired at 3 Tesla, with  $FA=50^\circ$  ( $\sim$ Ernst Angle) and  $TE=40$  ms ( $\sim T_2^*$ ). **b:** Image acquired at 7 Tesla, with  $FA=35^\circ$  ( $\sim$ Ernst Angle) and  $TE=25$  ms ( $\sim T_2^*$ ).

Comparing  $T_2^*$ -weighted images obtained at different field strengths, large improvements in CNRs can be obtained when migrating from 3 to 7 Tesla (Figure 1.9), as increasing static



magnetic field strength allows better sensitivity to magnetic susceptibility ([Ciobanu et al., 2012](#)). This increased  $T_2^*$  contrast is not only beneficial for structural brain imaging but also for BOLD-based fMRI, as the physiological noise contributions (venous blood) are expected to decrease with increased resolutions while the BOLD signal increases nearly linearly with field strength ([Triantafyllou et al., 2005](#)).

UHF also provides benefits to the following imaging modalities:

- The prolonged longitudinal relaxation time of blood available at UHF is used in Arterial Spin Labeling (ASL) perfusion studies to visualize the tagged blood for a longer time during the passage through the tissue ([Zuo et al., 2013](#)).
- High field MR systems have allowed acquiring spectroscopic data sets with a better spectral differentiation of the individual metabolites ([Uğurbil et al., 2003](#)).
- One particular application that has also been shown to profit from higher field strengths is time-of-flight (TOF) MR Angiography, thanks to a longer  $T_1$  and higher SNR ([Schmitter et al., 2014](#)).
- The primary interest of MRM for biology and medicine is the visualization of small biological structures weighted by various MR contrasts. Access to high resolution information on MR relaxation times or other MR measurable quantities inside microscopic structures thanks to UHF is of great interest ([Jelescu et al., 2013](#)).

### 1.4.2. Challenges

Unfortunately, working at ultra-high field does not only come with advantages. The increase in  $T_1$  with field strength sometimes leads to longer scan times because repetition times need to be increased. Variations in magnetic susceptibility produce larger unwanted static field inhomogeneities, especially at interfaces, resulting in very short  $T_2^*$  and overall image degradation. Last but not least, increasing the field strength means working at higher radio-frequencies for excitation and reception.

The biggest challenge raised by the spreading of UHF MRI is thus the increased level of RF excitation non-uniformity. Indeed, when moving toward UHF (7 Tesla and beyond), the increased resonance frequency of proton nuclei (297 MHz at 7 Tesla) causes the RF wavelength to become smaller than the human brain, leading to an inhomogeneous distribution of the transmit magnetic field ( $B_1^+$ ) (Figures 1.10.a and 1.10.b). These spatial  $B_1^+$  inhomogeneities generate significant SNR and CNR variations for any given tissue across the brain (Figures 1.10.c and 1.10.d) ([Van de Moortele et al., 2005](#); [Visser et al., 2010](#); [Cloos et al., 2012a, 2012b](#); [Massire et al., 2014](#)). If not addressed, these can notably produce signal voids where all the information is lost, detrimental to medical diagnosis.

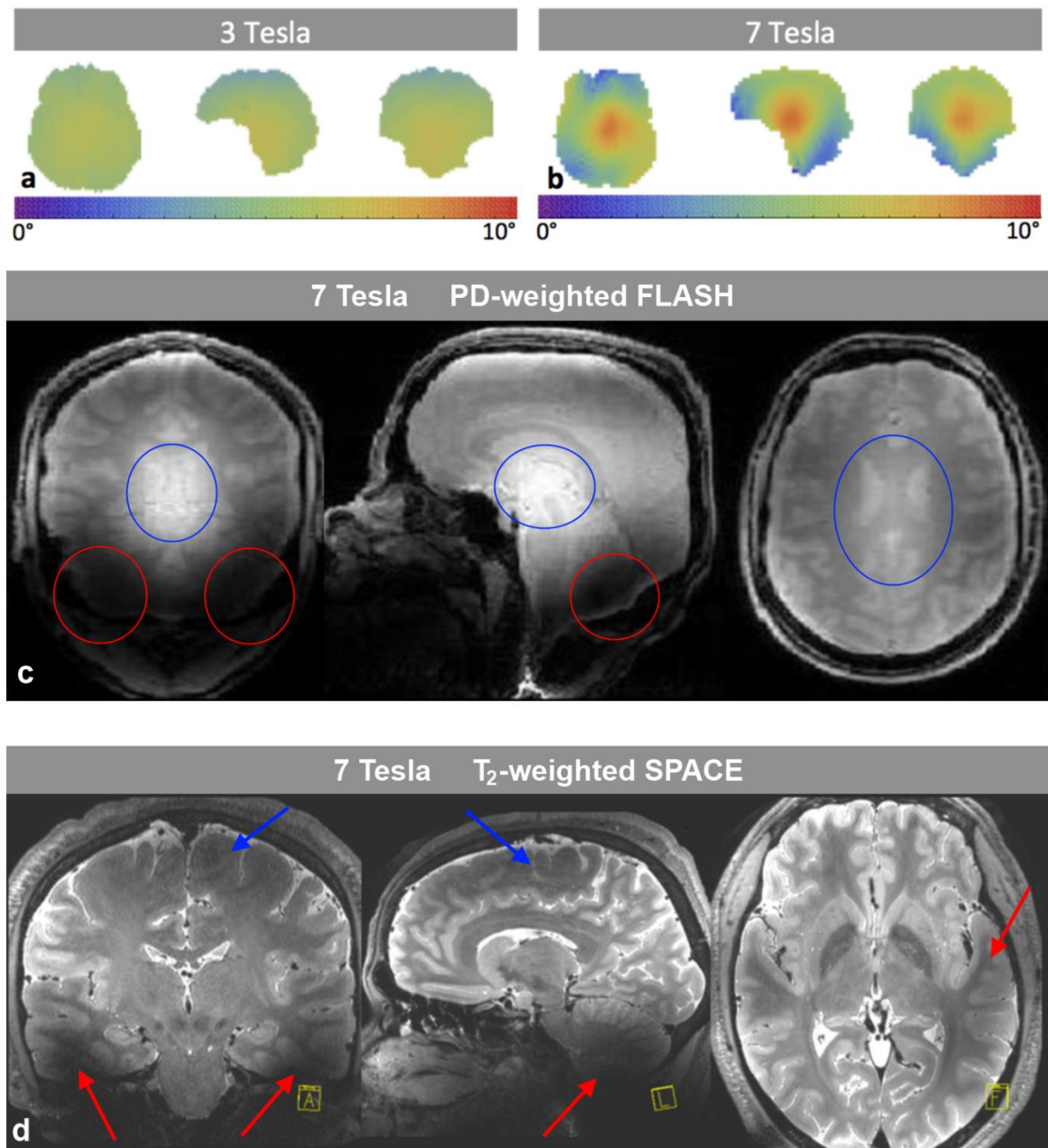


**Figure 1.10:** RF excitation non-uniformity at UHF. **a, b:** Comparison of the excitation uniformity in the small-flip-angle regime (expressed in flip-angle maps in degrees) obtained at 3 Tesla (low dispersion, Siemens Magnetom Tim Trio) and 7 Tesla (high dispersion, Siemens Magnetom), with a quadrature head coil. **c:** Image acquired with a proton density-weighted FLASH sequence at 7 Tesla equipped with a quadrature head coil. Blue rings indicate what is commonly referred to as the central brightening effect, whereas the red rings indicate the areas of signal loss. **c:** T<sub>2</sub>-weighted image acquired with the SPACE sequence at

7 Tesla (0.6 mm isotropic resolution, with 1Tx/32Rx Nova Medical head coil). Blue arrows refer to local losses of contrast, whereas red arrows show signal voids.

Besides the observed increased non-uniformity of the excitation field, energy deposition is proportional to the square of the frequency (Bottomley and Andrew, 1978). As an example, when considering the idealized case of a homogeneous spherical phantom centered in a quadrature coil, the following relation between the absorbed power (P) by the sphere and the Larmor frequency, and therefore the static field strength, is found (Hoult and Lauterbur, 1979):

$$P = \frac{2\omega_0^2 B_1^{+2} a^5}{15} \quad (1.16)$$

where  $a$  is the radius of the sphere. Moreover, depending on the setup at hand, the maximum local-SAR to global-SAR ratio may increase as a result of the reduced wavelength and enhanced interference effects.

Consequently, many SAR-demanding imaging protocols commonly adopted at low field strength need to be redesigned before application at UHF. It is however at the same time highly desirable to minimize the acquisition time of a MRI sequence, not only for patient comfort and cost efficiency, but also to limit motion artifacts. Indeed, as the acquisition time becomes longer, it becomes increasingly difficult for the subject to refrain from moving. Furthermore, even small artifacts due to involuntary movements such as swallowing and breathing can be problematic when considering ultra-high-resolution structural imaging.

### 1.4.3. Solutions

As mentioned earlier, unique information relevant to various disease processes is currently available at UHF. There has been some hesitation about clinical use of UHF, given concerns about whether traditional clinical information remained available at such field strengths despite changes in contrast, signal inhomogeneity, SAR and acquisition time limitations.

Yet, with appropriate RF coils, pulse sequence modifications, and imaging protocol optimizations, UHF scanners may be used without losing most of the key clinical information content present in traditional imaging protocols at lower field strengths. This means that unique information of new clinical value may now be accessed without sacrificing routine clinical information. Last, after a period of exploratory development, a variety of robust commercial UHF coils is now available.

Parallel imaging ([Sodickson and Manning, 1997](#); [Pruessmann et al., 1999](#); [Griswold et al., 2002](#)) is one of the most potent tools available to decrease the acquisition time while maintaining contrast and resolution. This technique exploits the different sensitivity profiles from multiple receive elements ([Roemer et al., 1990](#)) to reconstruct an under-sampled image. The key principle behind these methods is the complementarity between the different receive-sensitivities. With increased field strength, therefore shortened RF wavelengths, the receive profiles corresponding to each of the coil elements become more distinct. Consequently, higher acceleration factors can be reached with only limited image quality degradation ([Ohliger and Sodickson, 2006](#)).

Parallel-transmission (pTX) is the counterpart of parallel imaging, this time dealing with RF pulses. Subject-specific pulse design can be employed to mitigate  $B_1^+$  inhomogeneities at UHF and restore signal and contrast in the entire image. Combining the latter with the former enables better latitude to improve mitigation performances, as more degrees of freedom are considered. Indeed, Transmit-SENSE ([Katscher et al., 2003](#)), exploits the full potential of transmit-array coils by tailoring the RF waveforms to apply to each of the individual coil-elements. This transmission generally occurs in concert with magnetic field gradients. All these considerations will be described in the upcoming chapter.

## 2. MRI Pulse Design & Parallel Transmission

### 2.1. Radio-Frequency Pulse Design

In the previous chapter, we explained how MRI is based on the use of RF pulses to manipulate magnetization in order to achieve imaging contrasts useful to medical diagnosis. We also saw that UHF MRI could provide tremendous improvements, but also bring challenges to obtain desired improvement in image quality, the RF excitation non-uniformity and the increased energy deposition being the main targets to tackle in this work.

Analysis and design of RF pulses, as well as MRI sequence conception, is a stimulating field of investigation in MRI. When individual transmit sensitivities  $B_1^+$  are considered as inputs for the pulse design, we deal with RF-tailored pulses. These are no longer generic shaped-pulses but singular objects, designed thanks to optimization algorithms, which solve a subject-specific problem, and achieve better performance regarding spin excitation, and thus better image quality. In this chapter, the concepts, techniques, strategies and tools which were developed by the different research communities to face MRI methodological challenges will be investigated, ending with the key technique: parallel-transmission (pTX).

#### 2.1.1. Multi-dimensional RF Pulses and k-space interpretation

Multi-dimensional RF pulses ([Bottomley and Hardy, 1987](#)) are spatially selective in more than one direction, as opposed to familiar slice-selective RF pulses. These pulses have long duration and require gradient waveforms to be played in concert with. They could be used for excitation, but also saturation, inversion and refocusing ([Pauly et al., 1989b](#)).

By making an analogy with the Fourier encoding used in the imaging process, the concept of k-space can also be extended to the domain of multi-dimensional RF pulse design ([Pauly et al., 1989a](#)). Indeed, the spin excitation may be seen as scanning the applied RF energy across the same k-space as used for acquisition. This statement can be verified by studying the small-tip-angle approximation (STA), which assumes that the longitudinal magnetization remains equal to its equilibrium value during RF exposure ([Hoult and Lauterbur, 1979](#); [Pauly et al., 1989a](#)). This assumption allows linearizing the Bloch equation (Equation 1.4), whose first two components could be written as a single complex differential equation, ignoring relaxation:

$$\frac{\partial}{\partial t} M_T(\mathbf{r}) = -i\gamma[\mathbf{G}(t) \cdot \mathbf{r} M_T(\mathbf{r}) - B_1^+(\mathbf{r}, t) M_0] \quad (2.1)$$

where  $\mathbf{G}$  and  $B_1^+$  are the time-dependent gradient and complex transverse magnetic field, respectively. If the system is initially in the state  $\mathbf{M} = (0, 0, M_0)$ , solving this differential equation for the final magnetization at time  $T$  and using the STA results in:

$$M_T(\mathbf{r}) = i\gamma M_0 s(\mathbf{r}) \int_0^T b(t) e^{i\gamma \Delta B_0(\mathbf{r})(t-T)} e^{-i\gamma \mathbf{r} \cdot \int_t^T \mathbf{G}(s) ds} dt \quad (2.2)$$

The first exponential term represents the phase accrued due to main field inhomogeneities  $\Delta B_0$ . Similar to the spatial frequency covered during image encoding, we can define the k-space trajectory  $\mathbf{k}(t)=[k_x(t) \ k_y(t) \ k_z(t)]$ , weighted by a complex RF pulse shape  $b(t)$  and the coil complex transmit sensitivity  $s(\mathbf{r})$ , as:

$$\mathbf{k}(t) = -\gamma \int_t^T \mathbf{G}(s) ds \quad (2.3)$$

Hence the “k-space interpretation” is found, where  $\mathbf{k}(t)$  constitutes a trajectory corresponding to a set of pre-defined gradient waveforms. This expression then gives explicit weighting of k-space by the RF excitation (Pauly et al., 1989a). With this interpretation, we can see that the resulting transverse magnetization is simply the Fourier transform of the k-space-weighted RF waveform.

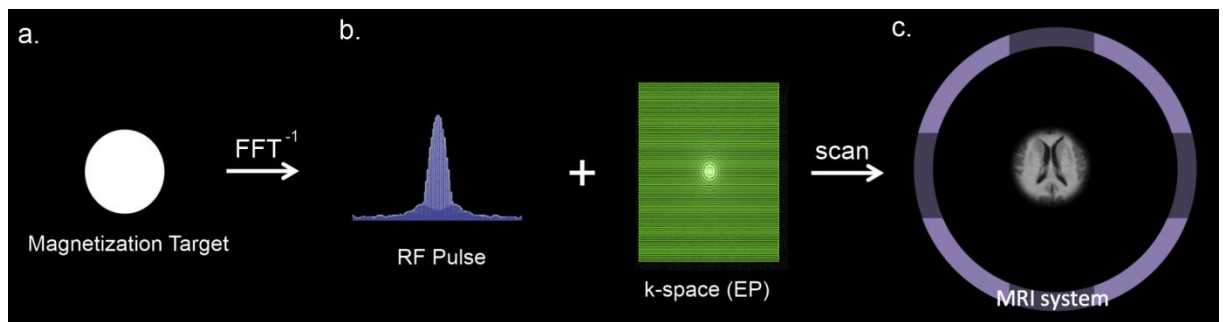


**Figure 2.1:** Schematic overview of the different steps involved in the design of a single-channel Fourier-based small-tip-angle 2D pulse. **a:** The desired target magnetization. **b:** The RF-waveform corresponding to the inverse Fourier-transform of target excitation pattern, added to gradient waveforms played during transmission to get an Echo-planar (EP) k-space trajectory, super-imposed in green on top of the inverse Fourier-transform of the target

magnetization. **c:** Final image after application of the designed RF and gradient waveforms in a suitable imaging sequence.

On the other hand, when considering the target  $M_T(r)$  distribution shown in Figure 2.1.a, the RF pulse is simply its inverse Fourier-transform, as it follows the Cartesian trajectory in Figure 2.1.b. This implies the RF-waveform is played in concert with the gradients, resulting in an excitation with the desired characteristics (Figure 2.1.c). This procedure begins to fail for pulses with larger flip angles due to the non-linearity of the Bloch Equation. In those cases, the RF pulse can be determined by iterative numerical optimization methods, such as the Shinnar-Le Roux (SLR) algorithm (Pauly et al., 1991).

Albeit a powerful tool for spatial selection, most potential applications involving multidimensional RF pulses are hampered by hardware limitations. In particular, gradient slew-rate and amplitude limits constrain the minimal pulse duration due to the wide spatial-spectral range necessary to facilitate an arbitrary excitation profile. Although a judiciously chosen k-space design may help reduce hardware limitations, highly selective excitations generally still result in unacceptably long pulse durations. These may not only exceed the repetition time desired, but also deteriorate image quality due to off-resonance, relaxation, and magnetization transfer effects during the pulse. Thanks to the introduction of array coils, accelerated multidimensional RF pulses can be considered. Equation (2.3) now suggests many different k-space trajectories to achieve specific spin excitations.

### 2.1.2. Trajectories through k-space

Just like EPI readout, echo planar (EP) trajectories are used to generate 2D RF pulses. 2D spiral (Pauly et al., 1989a) is another popular k-space trajectory for 2D RF pulses (Figure 2.2.a), because it uses two oscillating gradients to cover efficiently k-space. Spiral pulses have excellent immunity to flow artifacts, whereas EP pulses provide control of the slab thickness in the two dimensions (Bernstein et al., 2004). Apart from these two conventional strategies, several interesting designs have been published. Each of these techniques addresses a different goal, ranging from non-selective RF non-uniformity mitigation to selectively exciting an arbitrarily shaped three-dimensional sub-volume.

Among the above-mentioned methods, the “fast-kz” trajectory (Saekho et al., 2006) has been studied extensively (Setsompop et al., 2008c). The sparse design of this trajectory allows slice-selective uniform excitations with relatively short pulse durations. The key principle of this method resides in the combination of a dense k-space sampling along the slice direction interleaved with a few short gradient blips orthogonal to this direction. When viewed as a



path through k-space, the fast-kz trajectory resembles a set of spokes, hence their nickname: “Spokes” (Figure 2.2.b). Thanks to pTX-enabled k-space acceleration (see Section 2.4.) there has been a renewed interest in multidimensional RF pulse design dedicated to volumetric imaging. Designs that selectively excite an inner-volume are explored to facilitate un-aliased “zoomed” MRI. Instead of a sparse k-space distribution, the 3D-selectivity necessitates sampling an extensive portion of 3D k-space by adopting accelerated stacks of 2D-spirals (Saekho et al., 2005) or 3D-spirals (Schneider et al., 2013) (Figure 2.2.c). Finally, non-selective uniform excitations can benefit from the multidimensional tailored RF pulse design approach by only exploring a few locations in k-space. This method, the so-called “ $k_T$ -points” (Figure 2.2.d) was initially introduced in 2010 (Cloos et al., 2012a). For a homogeneous 3D excitation, the  $k_T$ -points embody a limited number of excitation sub-pulses, interleaved with gradient blips, to travel between transmission sites in three-dimensional k-space. Sub-pulses can simply be square or more elaborate shapes and no gradient is played a priori while pulsing RF. The name “ $k_T$ -points” indicates that RF-power is applied only while stationary in k-space, “ $k_T$ ” standing for transmission k-space. It therefore operates in a way so as to not waste time and energy at spatial frequencies which need not be addressed in the context of smooth RF inhomogeneities. Indeed, only a few locations in the vicinity of the k-space center are excited. When applied in conjunction with parallel transmission, sub-millisecond pulses are made possible, leading to a broad spectrum of potential applications in 3D-acquired sequences. The  $k_T$ -point framework will be used in the pulse design methods presented in this manuscript.



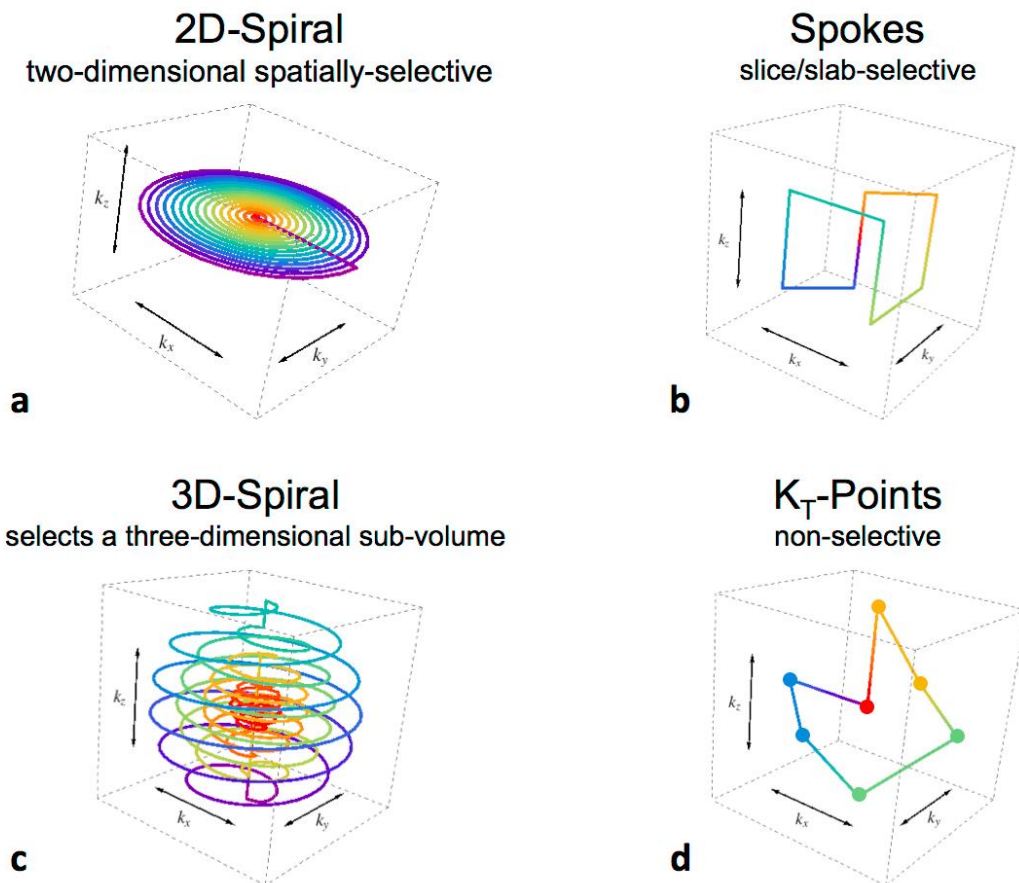


**Figure 2.2:** Several k-space trajectories considered for multi-dimensional RF pulses, each one addressing a different goal (Cloos, 2012). **a:** 2D-Spiral: 2-dimensionnal excitation pattern. **b:** Spokes: uniform selective excitation. **c:** 3D-spiral: inner-volume selection. **d:**  $k_T$ -points: uniform non-selective excitation.

## 2.2. MRI Coils

### 2.2.1. Types of MRI coils

Radiofrequency coils are a central part of the radiofrequency hardware system in MRI. Most clinical MRI scanners use volume coil to perform whole-body imaging, and smaller volume coils have been constructed for the head and other extremities.

- **Volume coils:** Volume coils have a better RF homogeneity than surface coils. The most commonly used design is a birdcage coil (Hayes et al., 1985). This consists of a number of rods running along the z-direction, arranged to give a sine current variation around the circumference of the coil.

- **Surface coils:** A surface coil is essentially a loop of conducting material, such as copper. This type of receiver coil is placed directly close to the region of interest for increased magnetic sensitivity. The loop may form various shapes and be bent slightly to conform to the imaged object. Surface coils have a good SNR for tissues adjacent to the coil and their sensitivities decrease with distance.
- **Transceiver coils:** An RF coil that acts as a transmitter, producing the  $B_1^+$  excitation field, and as a receiver ( $B_1^-$ ) of the MRI signal, is called a transceiver coil. Such a coil requires a T/R switching circuit to switch between the two modes. A body coil is typically a T/R coil, but smaller volume T/R coils (head/extremities) are also used.

As mentioned in the previous chapter, RF inhomogeneity increases with  $B_0$ , progressively introducing a stronger bias in the acquired images, which can become problematic for diagnosis purposes above 3 Tesla.

### 2.2.2. Multiple channel coils

To mitigate the above-mentioned effects, transmit-arrays consisting of multiple independent coil-elements, exhibiting spatially different sensitivity patterns, were introduced ([Ibrahim et al., 2001](#); [Adriany et al., 2005](#)). In contrast with the phased arrays used for reception ([Roemer et al., 1990](#)), most modern MRI systems are not equipped with multi-transmit capabilities. Those investigational devices fitted with a multi-transmit extension are typically limited to 8 independent channels, whereas the latest clinical MRI systems already offer up to 128 receive channels (for example: Magnetom Skyra, Siemens Medical Systems, Erlangen, Germany).

Cylindrically symmetric transmit-coils, such as the birdcage ([Hayes et al., 1985](#)) and TEM resonator designs ([Vaughan et al., 1994](#)), are driven in their Circularly Polarized (CP)-mode by simply adjusting the relative phase between the transmit-elements according to their azimuthal angle ([Adriany et al., 2005](#)). A multi-transmit array system however is not limited to the above-mentioned CP-mode. In addition, an N-channel design supports N-1 additional and orthogonal eigenmodes ([Alagappan et al., 2007](#)). A pseudo-Circularly-Polarized mode with constructive interferences of the  $B_1^+$  in the center of the imaged object is often used as an initial setting of a multi-transmit coil.

Yet at UHF, none of the eigenmodes of a multi-transmit array system demonstrates a homogenous RF-field. Some improvement can be obtained by adjusting the relative phases

and amplitudes of the RF pulses between the coil-elements. This method, referred to as RF-shimming, can substantially reduce the RF non-uniformity in several conditions (Van de Moortele et al., 2005). Yet in practice at 7 Tesla, RF-shimming with a typical 8-channel multi-transmit configuration does not allow the desired level of FA uniformity to be reached throughout large regions of interest such as the entire human brain (Cloos et al., 2012a, 2012b; Massire et al., 2013). However, recent advances in the field of transmit-array coil design (with more coil elements or different element geometries) could yield more flexible solutions (Kozlov and Turner, 2009; Wu et al., 2013). Parallel transmission (pTX), which will be the subject of Section 2.4, provides more latitude than RF-shimming to reach desired excitation uniformity and is consequently used throughout this thesis.

### 2.3. $B_1^+$ Mapping

When considering an MRI exam with a transmit-array coil and before any subject-specific RF optimization can be computed, the spatially-dependent transmit sensitivities  $B_{1,n}^+$  (where  $n$  is the coil channel index) have to be estimated. These transmit-sensitivities quantify the amplitude and relative phase of the co-rotating RF-field produced by each coil-element and can be then be deduced from a dedicated MRI measurement. This should take as little time as possible and requires good accuracy. To this end, numerous techniques have been proposed over the years (Yarnykh, 2007; Fautz et al., 2008; Nehrke and Börnert, 2012). Recent endeavors known as to MRI fingerprinting (Ma et al., 2013) propose an alternative method to evaluate the transmit sensitivities in a short duration.

Although  $B_1^+$ -mapping sequence development is still a very active field of research, the actual flip-angle imaging (AFI) sequence (Yarnykh, 2007), including various improvements (Amadon and Boulant, 2008; Nehrke, 2009; Boulant et al., 2010), is currently among the most popular methods. Due to its steady-state implementation, short repetition times are feasible without the need for a SAR intensive reset pulse. Nevertheless, the AFI sequence applied to transmit-arrays is still relatively time-consuming and SAR-demanding. Considering that these calibrations have to be repeated for each subject before clinically relevant measurements can be started, various faster yet less accurate methods have been proposed, such as the DREAM sequence (Nehrke and Börnert, 2012).

The XFL sequence (Fautz et al., 2008; Amadon et al., 2012) is a 2D multi-slice magnetization-prepared turbo-FLASH sequence. Magnetization preparation is achieved using a very selective VERSE'd saturation pulse, which produces a spatially-dependent FA to be measured (partial saturation). This preparation pulse is immediately followed by a gradient spoiler and a centric-ordered FLASH readout train. Non-prepared FLASH scans

acquire the transmit phase maps. The XFL sequence produces 3D  $B_1^+$  maps in less than 5 minutes for 8-channel coil arrays with excellent correlation and identical resolution compared to the ones produced by the AFI sequence. This is why this sequence was used for all in vivo experiments in this thesis.

In any case, with a transmit-array, regions far away from the transmitting element under investigation are usually dominated by noise. To counteract this problem, the matrix-based field mapping approach (also known as the interferometric method) was proposed ([Brunner and Pruessmann, 2009](#)). This procedure combines the transmit-channels in different linear combinations, allowing the transmit-sensitivities corresponding to the individual transmit-channels to be retrieved after adapted post-processing, that is to say a matrix inversion. To this end, typically the pseudo-CP mode is considered as a “reference”, which is perturbed by cyclically adding  $\pi$  to the phase on each one of the channels. The advantage of this method is that the peak power per channel can be reduced while simultaneously obtaining a more favorable signal-to-noise distribution. This method can be combined with any of the above-mentioned sequences.

## 2.4. Parallel Transmission

### 2.4.1. Origins

The development of parallel imaging began with the introduction in the 1980s of the phased array coil concept ([Roemer et al., 1990](#)) as a suitable hardware platform to increase the SNR and/or to shorten the acquisition. Parallel imaging makes use of the spatially varying sensitivities of individual coil elements forming a receive coil array that can be used to encode spatial information during signal reception. This signal encoding allows for the reduction of the number of necessary phase-encoding steps conventionally required and thus the acceleration of scanning and/or the increase of spatial resolution. Different algorithms have been elaborated in order to combine the individual coil data and to compensate for the residual reception inhomogeneities ([Roemer et al., 1990](#)). In contrast to some early ideas, which tried to overcome conventional phase encoding completely, these approaches to accelerated parallel imaging perform sensitivity and phase encoding simultaneously. Consequent subsampling in k-space makes image reconstruction more complicated than just using the Fourier transform. These different techniques can be divided according to the k-space and the image-space domains, in which the processing is mainly performed. SMASH (Simultaneous Acquisition of Spatial Harmonics) ([Sodickson and Manning, 1997](#)) was proposed as an approach to perform parallel imaging in k-space. The

same holds for GRAPPA (Generalized Autocalibrating Partially Parallel Acquisition) (Griswold et al., 2002), a further refinement that incorporates the idea of autocalibration. In contrast to these, the processing in SENSE (for Sensitivity Encoding) (Pruessmann et al., 1999) is performed in the spatial domain. Numerous generalizations and refinements have been further elaborated, making nowadays the strict distinction between k-space and image domain rather impractical. As shown in Figure 2.3., the SENSE imaging method takes advantage of the distinct receive-sensitivity profiles of the coil-elements to reconstruct an un-aliased image from a reduced k-space acquisition.

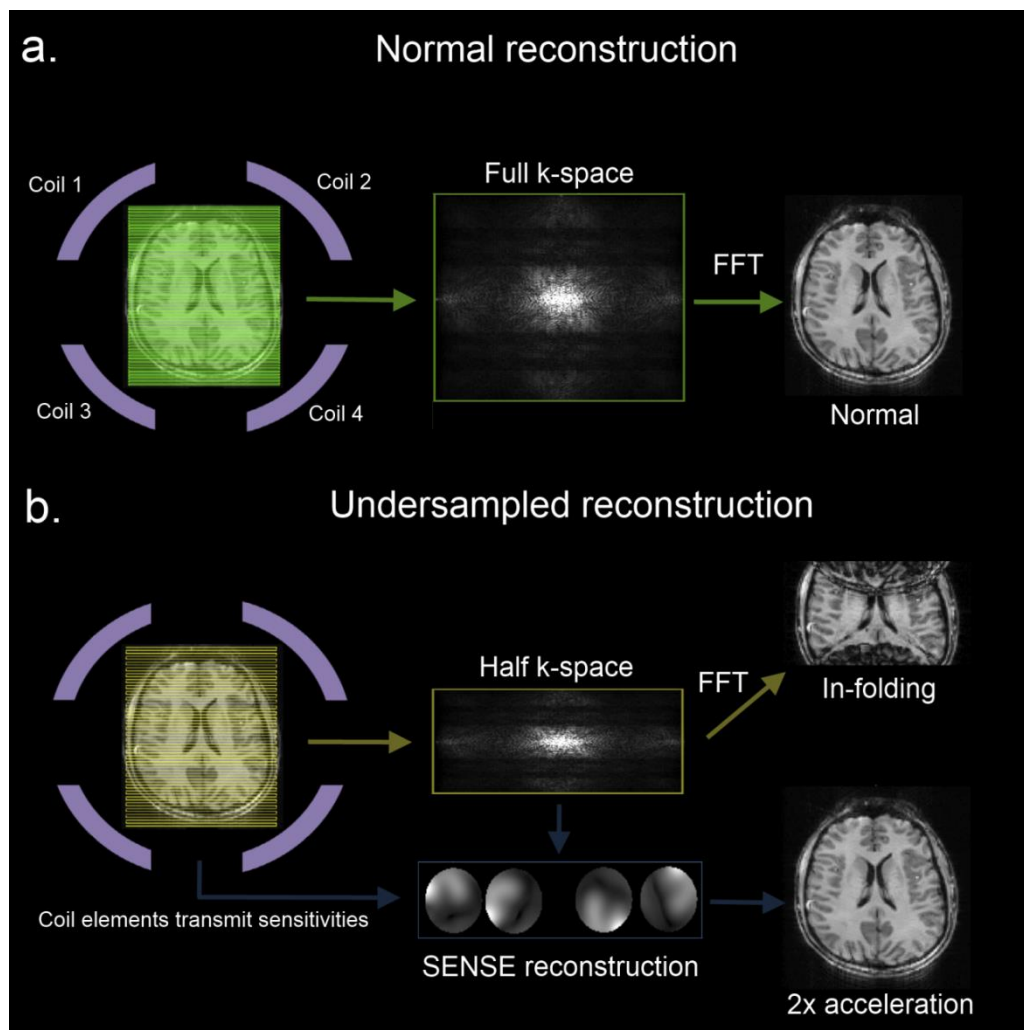


**Figure 2.3:** Schematic overview of two imaging and reconstruction strategies. **a:** The standard reconstruction method, sampling the full k-space (green). **b:** A 2x under-sampled acquisition, resulting in an aliased image with conventional reconstruction (yellow). Parallel imaging (SENSE), using the receive sensitivities corresponding to the different coil-elements (blue), enables correct data reconstruction with the corresponding acceleration factor.

The young history of pTX shows some similarities with the developments in parallel imaging. With the introduction of human UHF proton MRI systems, problems of  $B_1^+$  inhomogeneities caused by dielectric resonance effects came into focus. Multiport excitation for birdcage-type coils was proposed as a measure to improve the RF homogeneity in the excited volume (Ibrahim et al., 2000). The underlying hardware could thus be considered as a multi-element transmit coil array, which allows independent adjustment of the phase and amplitude of the otherwise identical waveforms for the individual ports (i.e. performing RF shimming) (Adriany et al., 2005). Inspired from parallel imaging, multiple transmit coils can be utilized to perform parallel transmission. Again, the two initial approaches proposed for parallel transmission differ in the central matrix inversion. Either it is performed in the Fourier space (Katscher et al., 2003) or in the spatial domain (Zhu, 2004). The so-called “Transmit-SENSE” (Katscher et al., 2003) method allows a desired target excitation to be reached with a reduced k-space sampling during RF transmission, using multiple transmit coil elements, each of which exhibiting a spatially different sensitivity pattern and being driven by a specific time-dependent RF waveform (Figure 2.4.). The pTX additional degrees of freedom offer the possibility to improve spatially selective multidimensional RF pulses (Pauly et al., 1989a), for example by shortening the pulse duration, enhancing their spatial definition, or reducing their required RF power. This enables multidimensional RF-pulses to be included in fast sequences with short repetition times, while simultaneously reducing the impact of relaxation and off-resonance effects during the RF pulse. Furthermore, it facilitates the application of 3D pulses, which are limited by the finite lifetime of the transverse magnetization and the main field homogeneity. Finally, the compensation of patient-induced RF inhomogeneities is a major application of the approach, particularly at UHF.



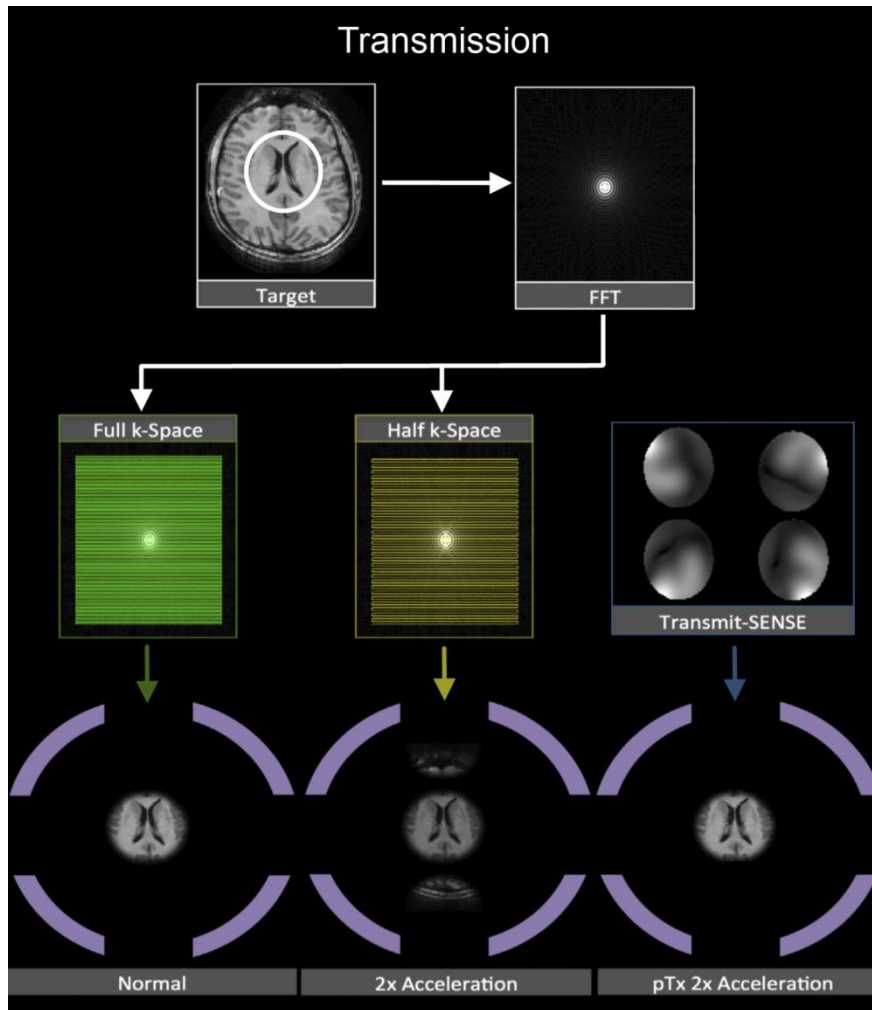


**Figure 2.4:** Schematic overview of 3 transmission strategies, each one indicated with arrows of a different color. **Green:** The standard single-channel-tailored multidimensional RF-excitation, as described in section 1 of this chapter. **Yellow:** The effect of under-sampling k-space by a factor 2 during transmission, resulting in non-desired excited magnetization. **Blue:** When adopting parallel transmission and taking into account the transmit-sensitivity of each coil-element, the same target magnetization is produced while under-sampling the k-space by a factor of 2.

Parallel transmission is not simply the reciprocal of parallel imaging. Both approaches are a combination of a forward and an inverse matrix problem. Parallel imaging and parallel transmission can be applied during an MRI sequence without any interference. Parallel imaging is based on the acquisition k-space whereas parallel transmission is based on the excitation k-space. Thus, the main goal of parallel imaging is the shortening of acquisition times, and the main goal of parallel transmission is the shortening of RF pulse durations. These considerations can be expressed as two central questions, individually related to parallel imaging and parallel transmission, respectively:

- In parallel MRI, given multiple measured, undersampled  $k$ -space data sets from the individual receive coils, how does one get a single, entire image?
- In pTX, given a single, entire spatial excitation pattern as a target, how does one get the individual, undersampled spatial patterns for each of the transmit coils coming with their individual sensitivity profiles?

When dealing with multi-element coil design, it is observed that an array geometry suitable for parallel imaging is generally also suitable for parallel transmission. Thus, the use of coil arrays capable for both is possible, which therefore eases coil array design. Nevertheless, for parallel imaging, a suboptimal geometry of the coil array leads to a nonlinear enhancement of the noise in the reconstructed image ([Pruessmann et al., 1999](#)). On the other hand, for parallel transmission, a suboptimal geometry of the coil array leads to a nonlinear enhancement of the SAR ([Zhu, 2006](#)). Last, a negligible influence of the geometric coil-array configuration on the resulting quality of the excitation pattern reproduction has been shown with simulations ([Katscher et al., 2005](#)), this result only being affected for extreme cases, for example when coil elements are lying almost on top of each other.

For an elegant and concise review of the different parallel imaging and parallel excitation techniques and frameworks, the reader is directed to ([Katscher and Börnert, 2006, 2007](#)).

#### 2.4.2. Spatial Domain method

The Spatial Domain Method (SDM) ([Grissom et al., 2006](#)) is a formulation of transmit-SENSE in the spatial domain. It allows for spatially variant excitation error weighting and thus ROI specification. Main field inhomogeneity  $\Delta B_0$  is easily incorporated in the design. Last, this method does not require computation of a Jacobian for compensation of  $k$ -space velocity and density, nor does it require interpolation between excitation  $k$ -space trajectories. It is a multi-coil generalization of the iterative pulse design method ([Yip et al., 2005](#)), optimization is based on the minimization of a quadratic cost function that consists of an excitation error term, which quantifies excitation error in the spatial domain, and a choice of regularization terms. The regularization terms can be used to control the integrated and peak RF power. The minimization problem can be solved iteratively via the conjugate gradient method or brute-force inversion.

As shown in equation (2.2), the STA transverse magnetization  $\mathbf{M}_T$  resulting from a single coil could be rewritten as the Fourier Transform of the  $k$ -space trajectory traversed and weighted by the RF excitation. This formalism can be extended to analyze the parallel excitation induced by a transmit-array, based on the property of linearity:



$$\mathbf{M}_T(\mathbf{r}) = i\gamma M_0 \sum_{n=1}^N s_n(\mathbf{r}) \int_0^T b_n(t) e^{i\gamma \Delta B_0(\mathbf{r})(t-T)} e^{i \mathbf{r} \cdot \mathbf{k}(t)} dt \quad (2.4)$$

where  $N$  denotes the total number of coil elements,  $s_n$  the transmit spatial sensitivity and  $b_n$  the complex RF shapes of the element  $n$ . The use of a multiple transmit coil, with each element exhibiting a spatially different sensitivity pattern and driven by a specific RF waveform, could therefore be used to reduce the path to be traversed in excitation  $k$ -space, thereby shortening the RF pulses without sacrificing spatial definition.

The  $k$ -space trajectory is equal to the time-reversed integration of the gradient waveforms to be played during excitation. By discretizing space and time with  $N_s$  and  $N_t$  samples respectively, we may write the transverse magnetization as a  $N_s$ -length column vector, via horizontal concatenation of the matrices  $\mathbf{D}_n \mathbf{A}$  and vertical concatenation of the vectors  $\mathbf{b}_n$ , resulting in:

$$\mathbf{M}_T = [\mathbf{D}_1 \mathbf{A} \ \dots \ \mathbf{D}_N \mathbf{A}] \begin{bmatrix} b_1 \\ \vdots \\ b_N \end{bmatrix} = \sum_{n=1}^N \mathbf{D}_n \mathbf{A} \mathbf{b}_n = \mathbf{A}_{full} \mathbf{b}_{full} \quad (2.5)$$

where  $\mathbf{D}_n(\mathbf{r}) = \text{diag}\{s_n(\mathbf{r})\}$  is a  $N_s \times N_s$  diagonal matrix containing spatial samples of the transmit sensitivity map of coil element  $n$ ,  $\mathbf{b}_n$  is a  $N_t$ -length vector of RF pulse samples for coil-element  $n$ , and  $\mathbf{A}$  is a  $N_s \times N_t$  matrix, whose elements are:

$$a_{rt} = i\gamma M_0 \Delta t e^{i\gamma \Delta B_0(\mathbf{r})(t-T)} e^{i \mathbf{r} \cdot \mathbf{k}(t)} \quad (2.6)$$

Given a target transverse magnetization profile vector  $\mathbf{m}_{des}$  containing  $N_s$  samples, finding the RF pulse  $\mathbf{b}_{tot}$  is a linear inverse problem. In order to produce a well-conditioned convex optimization problem, a Tikhonov regularization is often introduced. Effectively, it adds to the least squares residual a cost function proportional to the RF power integrated over time and coil elements, thereby suppressing solutions with large integrated RF powers. The standard method uses the same Tikhonov parameter for all the elements in the coil to reduce the overall RF power by solving the following minimization problem:

$$\min_{\mathbf{b}_{full}} \left\{ \|\mathbf{A}_{full} \mathbf{b}_{full} - \mathbf{m}_{des}\|_2^2 + R(\mathbf{b}_{full}) \right\} \quad (2.7)$$

The regularization method was subsequently refined with channel-dependent Tikhonov parameter values, in order to reduce the maximum local SAR (Cloos et al., 2010a).

### 2.4.3. Magnitude Least Square Problem

The previously introduced SDM considers a Least Square (LS) optimization, that is to say a cost function with a complex magnetization target to aim at. The associated optimization method is convex, but selecting an alternative target phase distribution results in a different and possibly more optimal RF-solution. Yet for many excitation applications, the quantity of interest is only the magnitude of the magnetization and the optimal solution among all possible phase distributions is desired. Indeed, as long as they are not too large within a voxel, low-order spatial phase variations do not impose a significant penalty.

The Magnitude Least Squares (MLS) optimization was therefore subsequently applied to improve excitation magnitude profile and reduce the required RF power, taking advantage of relaxed constraints on the phase profile (Setsompop et al., 2008a). In the SDM minimization formulation above (Equation 2.7), RF waveforms that are found will reduce the deviations from the target profile in both the magnitude and phase. However, when only magnitude images are of interest, the primary metric of interest is the fidelity of the magnitude profile while the phase profile is relatively unimportant, leading to the following minimization problem:

$$\min_{\mathbf{b}_{full}} \left\{ \left\| |\mathbf{A}_{full} \mathbf{b}_{full}| - \mathbf{m}_{des} \right\|_2^2 + R(\mathbf{b}_{full}) \right\} \quad (2.8)$$

Here,  $\mathbf{m}_{des}$  is specified as a real-valued vector. Unlike the LS, the MLS optimization is not convex and generally cannot be solved with a guarantee of global optimality.

To perform MLS optimization, the variable exchange method, which iteratively resets the target phase to the previously obtained phase pattern, is generally used. As a result, MLS optimization procedure greatly reduces the RF power while enhancing the excitation fidelity. Yet selecting an alternative initial target phase distribution may still result in a different RF pulse, whose performance may vary significantly. In particular, some of the initial targets may not work well at all. Therefore, the initial phase distribution has to be selected with some care. Although not necessarily the optimal solution, selecting the phase distribution corresponding to the CP-mode as an initial target generally performs well (Kerr et al., 2007). Very recently, several other strategies dedicated to solve the MLS problem in 3D were investigated (Hoyos-Idrobo et al., 2013), both in the small and the large FA regimes. These strategies consist of two stages: initializations and nonlinear programming approaches. Hard

constraints on SAR and power were also introduced, instead of commonly used regularization parameters. Small tip angle and inversion pulses are returned in less than 10 seconds in both cases, while respecting the constraints, allowing the use of the proposed approaches in routine.

#### **2.4.4. Large Tip Angle design and Optimal Control theory**

In the previous sections, various methods to design pTX-enabled RF-waveforms dedicated to many different applications have been presented. Most of these approaches rely on the STA approximation ([Pauly et al., 1989a](#)), which assumes that the longitudinal magnetization remains constant during the RF pulse (Section 2.1.1.). Albeit not an exact representation of the physics involved, this simplification can be applied to small or moderate FA excitations because in this domain the FA demonstrates an approximately linear dependence on the applied excitation field. Therefore, excitations pulses based on the STA approximation generally perform well when targeting a FA up to  $90^\circ$  ([Boulant and Hoult, 2012](#)).

Beyond this domain, the non-linear behavior of the Bloch equations must be considered. Nonetheless, a careful analysis of this non-linear system revealed that under certain conditions, the STA approximation may also yield viable large tip-angle (LTA) results ([Pauly et al., 1989b](#)). Consequently, when designing LTA pulses based on the STA approximation, sub-optimal levels of excitation fidelity are often obtained.

Large-tip-angle multidimensional pulses have been proposed for refocusing, transmit field inhomogeneity mitigation and 3-D volume-selective tagging. In the aforementioned applications, pulses are often designed either by segmenting the pulses into many successive STA pulses, or weighted by a 1-D envelope designed with a 1-D large-tip-angle pulse design method (SLR pulses). The emergence of pTX recently drove a renewed interest in multidimensional LTA pulse design. Yet, adhering to constraints imposed by the linear class of LTA (LCLTA) requires additional pulse length to correct LTA distortions in small-tip-designed RF pulses ([Xu et al., 2007](#)). Therefore, optimization techniques have been subsequently proposed to mitigate excitation defects that arise due the non-linear behavior of the Bloch equations in this regime ([Grissom et al., 2008](#)). Although not ensuring a global optimum, LTA excitations designed via optimal control methods ([Conolly et al., 1986](#)) have been demonstrated to provide robust results ([Xu et al., 2008](#); [Grissom et al., 2009](#)). These methods are iterative algorithms that design RF pulses by minimizing a cost function. The Bloch equation is iteratively evaluated using the current pulses. Gradients with respect the cost function are computed, and the pulse is updated by stepping in the negative gradient direction. The cost function framework used in optimal control also allows the user to include

regularizers and to refine gradient waveforms. Though the method is efficient in terms of convergence and pulse quality, evaluation of the Bloch equation at every iteration is computationally expensive.

Recasting the problem formulation into the spin-domain ([Pauly et al., 1991](#)) as proposed in ([Grissom et al., 2009](#)) reduces the computational load, and provides valuable tools to design refocusing pulses. Ultimately a direct LTA pulse design method, omitting the STA and including a direct k-space optimization routine, is desired to approach a truly optimized RF solution. An optimal control algorithm for the design of unitary propagators ([Khaneja et al., 2005](#)), originally dedicated to MR spectroscopy and quantum computing, and herein formulated into the spin-domain, is the core of the pulse design method developed in this thesis.

## 3. Experimental Setup

### 3.1. MRI system

#### 3.1.1. Magnet

All experimental results presented in this manuscript were obtained using the Siemens Magnetom 7 Tesla MRI system (Siemens Medical System, Erlangen, Germany) (Figure 3.1.a) equipped with parallel transmission capabilities and located at NeuroSpin, a CEA research center on brain imaging. As opposed to 3 Tesla MRI systems like the Trio, this system was built around an unshielded 90-cm-diameter-bore superconducting magnet (Magnex Scientific, Oxford, England) (Figure 3.1.b). The entire setup is enclosed in a 500-ton steel room to suppress stray fields outside the confines of the magnet room and in a Faraday cage to minimize RF noise from the outside. Each of the subsequent sections provides details concerning the MR components most relevant to the work presented in the succeeding chapters.



**Figure 3.1:** a: Siemens Magnetom 7 Tesla MRI system. b: 90-cm-diameter-bore superconducting magnet.

### 3.1.2. Gradient & Shim Coils

Since its installation in 2007, the above-mentioned MRI system is equipped with two complete gradient sets, a whole-body gradient system (Siemens) and a head-only gradient insert (AC84, Siemens). The first closely resembles what is typically available on a high-end clinical MR system (max slew-rate: 200 T/m/s, max amplitude: 45 mT/m). However, this whole-body gradient is not operational for imaging purposes at NeuroSpin. Nevertheless, it is currently used in static mode for shimming.

The gradient insert, on the other hand, can reach higher slew-rates (400 T/m/s) and larger gradient amplitudes (80 mT/m)<sup>1</sup>. However, due to its asymmetric design and smaller diameter (40 cm), gradient linearity is limited to a head-sized elliptical volume oriented along the main axis of the magnet. Bearing in mind NeuroSpin's exclusive focus on brain imaging and particular interest in diffusion MRI, the benefits provided by the head gradient insert are generally considered to outweigh the constraints imposed by the restricted inner radius.

However, with such a configuration, care needs to be taken not to introduce parasitic excitations. Particularly at ultra-high field, where the loaded magnet bore acts somewhat as a waveguide ([Brunner et al., 2009](#)), most head-only RF-coils demonstrate an increased sensitivity in the shoulder and chest regions. Due to the relatively small dimensions of the gradient insert and its dropping spatial encoding capacity beyond the above-mentioned ellipse, signal arising from these areas are aliased into the region of interest (Figure 3.2.a). To mitigate these “third-arm” artifacts, the shim coils from the body gradient set can be utilized to dephase the signal originating from the shoulder regions ([Wiggins et al., 2010](#)). This technique, referred to as the “double-shim” method, applies opposing currents on the second order Z-shim coils of both gradient sets, effectively spoiling the signal arising from the shoulder regions (Figure 3.2.c).

An alternative strategy currently studied consists in placing a jacket (Accusorb® MRI) on the subject which acts as an RF shield and absorbs RF waves ([Favazza et al., 2013](#)) (Figure 3.2.b). This jacket is made of a patented material (made of absorbent passive RF circuits and a thermal protection for patient safety) and was originally dedicated to military applications such as radar camouflage. This solution is already adopted in many clinical sites around the world for standard applications. Combination of both methods results in nearly complete parasitic artifact suppression (Figure 3.2.d).

---

<sup>1</sup> The slew-rate and the maximum gradient amplitude were willingly limited to 333 T/m/s and 50 mT/m respectively.

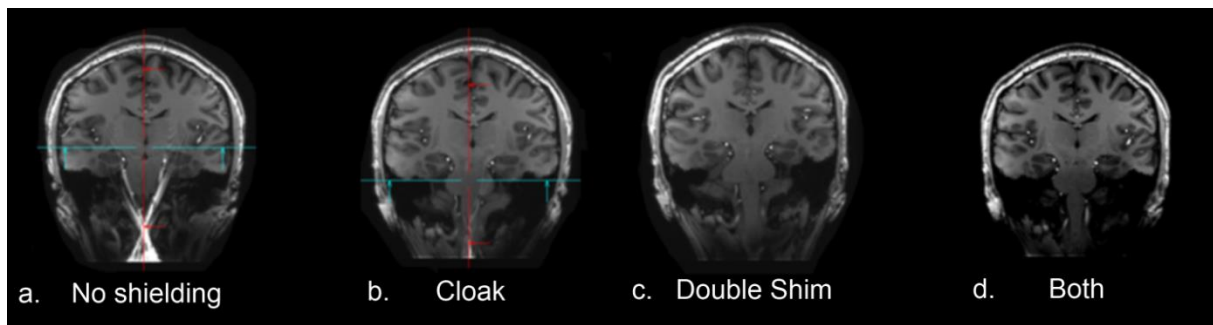


**Figure 3.2:** Coronal views from a 3D MP-RAGE sequence, with several configurations (courtesy from A. Vignaud). **a:** Without any correction, the “V”-shaped signal artifact aliased from the neck region is clearly visible. **b:** Image acquired on same volunteer without repositioning, with the vest around the subject neck. **c:** Image acquired with almost same positioning, but this time with opposing currents set in the body and head gradient z-shim coils. **d:** Same image with both correction methods.

### 3.1.3. Radio-Frequency Chain

In contrast to current clinical MR systems, typically equipped with only a single transmit-channel, the 7-Tesla system at NeuroSpin has been equipped with a pTX-extension including eight independent RF-pathways. The console used to operate the pTX-enabled system consists of 2 computer systems referred to as master and slave. The master controls a single transmit-channel (channel 8), and provides all the necessary tools to configure and prepare a new acquisition. The slave system allows any protocol prepared on the master system to be dispatched to all 8 transmit-pathways.

Eight independent modulators are each attached to their own power amplifier, providing up to 1-kW peak power each (Dressler, Fort Collins, USA). Via a directional coupler, the forward power coming from each amplifier is monitored in real-time by the Transmit Antenna Level Sensor (TALES) component, allowing the 20- $\mu$ s, 100-ms, 1-s, 10-s, and 6-min averaged power to be constrained (reflected power is not considered in the switch-off mechanism). In the event that one of the pre-specified limits is exceeded, the acquisition is terminated. However, it should be noted that currently, it remains the research institution’s responsibility to derive the appropriate time-averaged power limits such that compliance with the SAR guidelines is ensured. This work will be described in the next chapter. A brief description of the architecture involved here is provided in Figure 3.3.



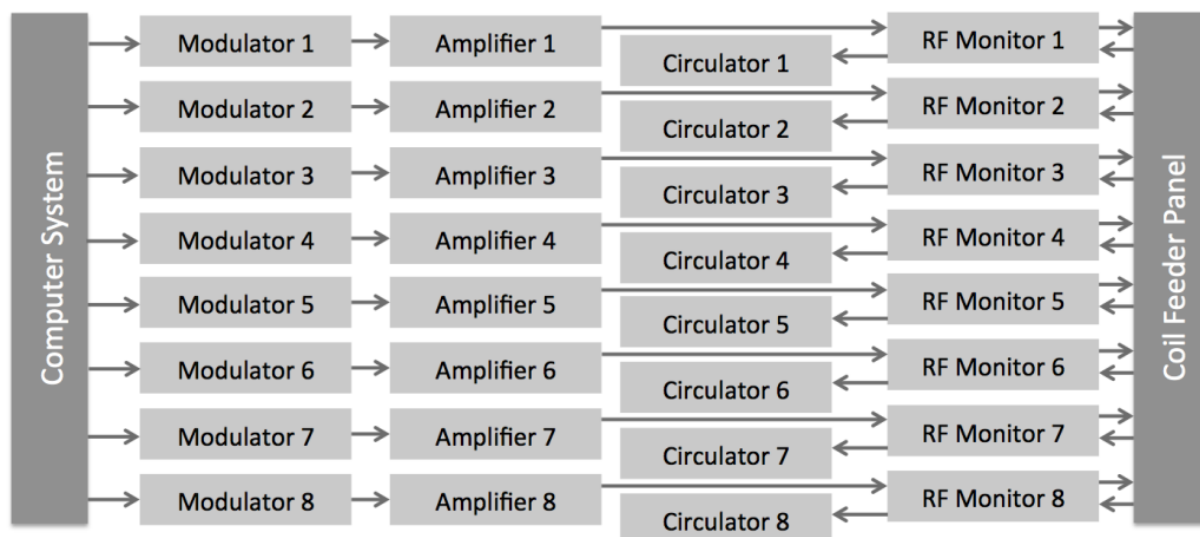


**Figure 3.3:** Schematic representation of the RF-chain corresponding to the 8-channel pTx-extension. Each of the individual transmit-channels is provided with its own modulator and amplifier. The forward power sent by each of the amplifiers is monitored. Reflected power and contributions from mutual coupling between coil-elements are dissipated in circulators.

### 3.1.4. Transmit-Array Coil

For pTX MRI scans, an array coil is necessary, which raises the question of the coil architecture: either a transmit-receive-array (transceiver) where dipoles (or loops) are used for both transmission and reception, or two dedicated sets of coils where dipoles are used only in transmission and reception loops are placed closer to the subject to receive MR signal. Coil design is a very complex and challenging matter and is beyond the scope of this work, however a transceiver coil is presumably easier to build in terms of architecture, mutual coupling between coil elements and spatial congestion.

This is why a home-made transceiver-array head coil was developed in collaboration with the *Institut de Recherche des Lois Fondamentales de l'Univers*<sup>2</sup> at CEA ([Ferrand et al., 2010](#)). The coil itself consists of 8 stripline dipoles distributed every 42.5° on a cylindrical surface of 27.6-cm diameter, leaving an 8.2-cm-wide window in front of the subject's eyes. The housing for the dipoles is made out of two polyoxymethylene half cylinders milled to provide close-fitting slots to hold each of the coil-elements. The dipoles themselves consist of a 280 x 28 x 2 mm<sup>3</sup> high purity solid copper strip (Figure 3.4.e). Each of them is fed via a BALUN (BALanced UNbalanced transformer) that acts as an electrical transformer between the

<sup>2</sup> Design and implementation by Michel Luong and Guillaume Ferrand at Commissariat à l'Energie Atomique, Direction des Sciences de la Matière, Institut de Recherche des lois Fondamentales de l'Univers, Service des Accélérateurs, de la Cryogénie et du Magnétisme.



coaxial feed line and the symmetrical central feeding points. Air is used as the dielectric between ground plane and dipole. To first order, each element was tuned using capacitive disks; subsequent fine-tuning is provided via the pi-circuit incorporated into each element. At the end of the coil, a semi-circular polyoxymethylene “crown” is attached (Figure 3.5) to provide the enclosure for the in-house-developed transmit/receive switches (-56 dB isolation between transmit and receive paths) and preamplifier circuits (23 dB amplification, 1.1 dB noise figure)<sup>3</sup>.

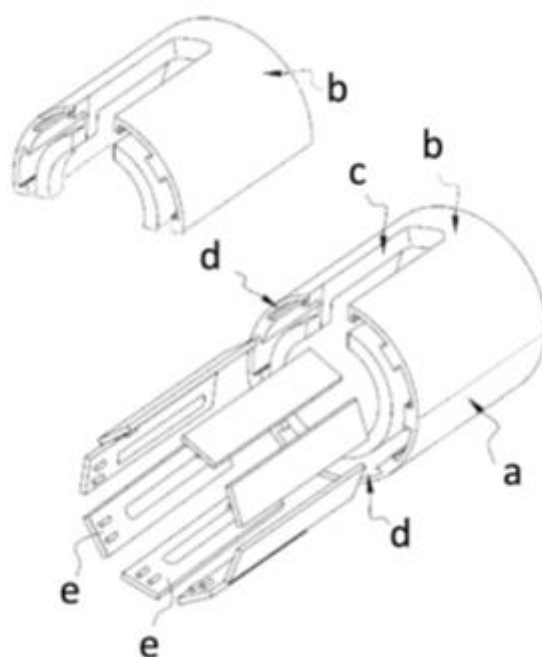


**Figure 3.4:** Exploded view of a dipole antenna and the transmit-array coil used throughout this thesis. The body of the coil consists of two halves (a & b). The top half (b), contains an opening (c) allowing the subject to look backwards out of the magnet bore via a mirror. Both parts of the coil body contain close-fitting slots to hold four dipoles in place (d). Each coil-element (e) consists of a substrate that supports the BALUN. The auxiliary circuit has its own tracks to connect the elements used for frequency tuning and impedance matching.

<sup>3</sup> Design and implementation by Marie-France Hang and Eric Giacomini at Commissariat à l'Energie Atomique, Direction des Sciences du Vivant, Institute d'Imagerie Biomédicale, NeuroSpin, Unité d'Imagerie RMN et de Spectroscopie.

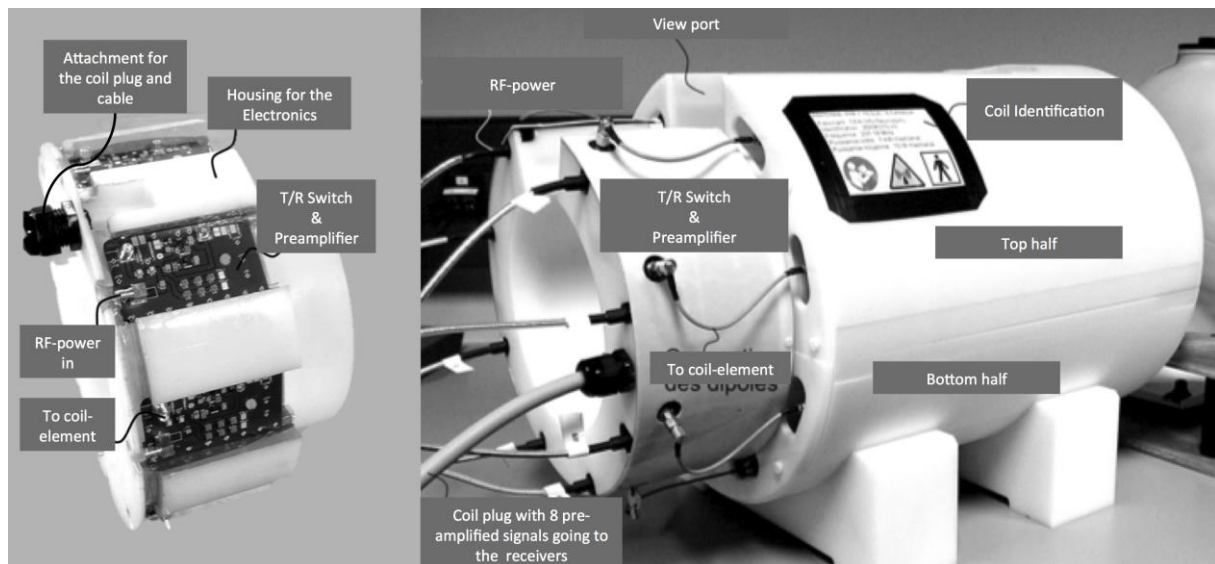


**Figure 3.5:** T/R switches on the crown and complete home-made coil used in this thesis.

To provide the necessary resources for SAR assessment (see next chapter), Finite Element (FE)-based simulations were performed. To this end, the coil was modeled with HFSS (ANSYS, Canonsburg, PA, USA) along with a human head load. Since the FE method allows volume elements of variable size and shape, it is particularly important to use a fine mesh near the coil-elements where strong spatial variations in the conservative electric fields are expected. This, in combination with the complexity of the human head model, requires a large number of tetrahedrons. Therefore a dedicated computer system equipped with 64 GB of working memory and 8 CPU cores was used (Dell, Precision T7500), thus allowing complex models made of approximately 1 million tetrahedrons to be evaluated within a reasonable time (approximately 10 hours for all eight channels simultaneously).

Future work includes the manufacture of a 12-channel transceiver coil, with better efficiency and smaller weight. In parallel, addition of 10 surface loops interleaved between transmission dipoles is considered to increase reception capability of the coil.

## 3.2. Other Materials

### 3.2.1. MRI phantom manufacturing

Imaging phantoms, or simply phantoms, are specially designed objects that are scanned or imaged in the field of medical imaging to evaluate, analyze, and tune the performance of

various imaging devices. These objects are more readily available and provide consistent results, avoiding exposing a living subject to possible risk.

In order to perform relevant electromagnetic and thermal simulations that will be used for SAR assessment and safety studies (Chapters 4 & 5), as well as MRI pilot scans for sequence design (Chapters 6 & 7), several properties of the human brain at 297 MHz need to be considered in making an MRI phantom (Figure 3.6.):

Longitudinal relaxation	$T_1$	$\sim 1680$ ms
Transverse relaxation	$T_2$	$\sim 50$ ms
Electrical conductivity	$\sigma$	$\sim 0,55$ S/m
Relative permittivity	$\epsilon_R$	$\sim 52$
Thermal conductivity	$k$	$\sim 0,54$ W/m/K
Material density	$\rho$	$\sim 1030$ kg/m <sup>3</sup>
Heat capacity	$C_p$	$\sim 3650$ J/kg/K

**Table 3.1:** Several physical properties of the human brain at 297 MHz. All these values are extracted from (Visser et al., 2010; Massire et al., 2012) and averaged for a mix of gray and white matter, assuming a ratio of  $\sim 1.0$  in the brain.

To get a solution with these properties, several chemical compounds easily available could be used in a distilled water solution:

- The classic chemical compounds used for  $T_1$  doping are:  $\text{CuSO}_4$ ,  $\text{MnCl}_2$ ,  $\text{GdCl}_3$  or Ni-DTPA.
- Agar powder reduces  $T_2$  relaxation whilst hardly affecting  $T_1$  relaxation.
- Realistic electrical conductivity can be achieved with the addition of NaCl, but this improves  $B_1^+$  homogeneity at the expense of  $B_1^+$  magnitude, the phantom diameter (here 16 cm) also needs to be considered.
- Addition of sucrose mostly decreases  $T_1$  and  $\epsilon_R$ .

Of course, all these physical properties are affected at different levels by all chemical compounds. To prevent any degradation of the phantom due to the presence of sucrose, diazolidinyl urea could be used as an anti-bacterial and anti-fungal agent. Last, the phantom must be sealed to prevent any external contamination, as well as water evaporation.

As an example, a concentration of NaCl of 4 g/L and a concentration of Agar of 10 g/L produced an electrical conductivity of 0.78 S/m and a relative permittivity of 74,3.

$T_1$  relaxation of the phantom was measured with the DESPOT1 method (two 3D GRE sequences with different flip angles ( $5^\circ$  and  $20^\circ$ ) and a 3D AFI sequence to measure  $B_1$ ).  $T_2$  relaxation was evaluated thanks to various 2D SE-EPI sequences (central coronal slice) with different TE ranging from 10 ms to 500 ms. Signal was fitted with an exponential decay and corrected for  $T_1$ . Electric properties were measured with a dedicated device (EpsiMu®, Institut Fresnel, Marseille, France).



**Figure 3.6:** Picture of one of the MRI phantoms made (16 cm diameter).

### 3.2.2. Computational Resources

To run electromagnetic simulations and pulse design software, a powerful desktop station equipped with two Intel Xenon E5-2670 CPUs (128 GB of RAM) paired with two high-performance-computing graphics card CUDA-enabled Tesla® Kepler™ K20 (NVIDIA Corporation, Santa Clara, CA, USA). These cards, equipped with a Graphics Processing Units (GPUs) GK110 containing 2496 cores, and 5 GB of errorcode-correction DDR5 memory, facilitate massive numbers of concurrent threads for the parallel evaluation of both SAR and Bloch equations. All the software tools developed in-house on GPU are based on a combination of C++ and Compute Unified Device Architecture (CUDA®, NVIDIA Corporation, Santa Clara, CA, USA). They are detailed in the subsequent chapters.

## 4. Specific Absorption Rate Assessment

### 4.1. Ensuring patient safety

#### 4.1.1. Aims

As stated in the first chapter of this manuscript, RF exposure could lead to local thermal damage or thermoregulatory problems. MRI systems are therefore subject to safety concerns, just like telecommunication devices are. For MRI, a rational way to ensure patient safety would be to:

- Predict the temperature increase in all the tissues due to a specific RF exposure, corresponding itself to a particular MRI sequence and a particular individual, prior to the exam.
- Ensure that the local temperature never exceeds the safety thresholds, thanks to a direct local temperature control during the MRI exam.

This optimal procedure is not achievable for several reasons. First, an accurate prediction of the local temperature rise requires:

- A. A subject-specific model to account for inter-individual variability and subject position in the coil.
- B. Dedicated software and powerful hardware capabilities to perform quasi-instantaneous simulation of the deposited energy.
- C. A proven theoretical temperature increase model in biologic tissues for accurate predictions.

Second, to perform a real-time monitoring of the patient exam, one would want:

- D. Both theoretical framework and dedicated technology to monitor efficiently the local temperature in the subject.
- E. Insurance that the system is working without failure.

Conditions A, C and D cannot be entirely fulfilled and alternative strategies were established as a consequence.

#### 4.1.2. Strategies

The current gold standard consists in performing simulations of the interaction between the MRI coil and the subject body to produce accurate maps of the electric and magnetic fields generated and thus quantify the RF exposure of the body. However, when considering typical tissue dimensions, field maps with at least 5 mm of isotropic resolution seem the extreme minimum acceptable, and more precise maps are necessary to represent accurately layers of bones, cartilage, liquid, fat and other tissues, which own various electric and thermal properties (see for example Table 5.1). Moreover, head dimensions and brain properties have large inter-subject variations. This is due for instance to: 1/ age: electrical conductivity, as well as WM/GM/CSF proportions evolve through normal aging ([Ge et al., 2002](#))), 2/ gender: women usually have smaller heads than men; and of course children and babies heads are significantly smaller than adults ones, or 3/ a pathology's presence: neurodegenerative diseases alter the brain composition, tumors have higher electrical conductivity ([Restivo et al., 2014](#)), ischemia and strokes locally change blood perfusion of the tissues. Given all these reasons, the subject-specific aspect of condition **(A)** seems mandatory. Nevertheless, getting a personal model for each individual is very laborious, as it requires several time-consuming stages to build the model and several hours of electromagnetic simulations. This is why generic (simplified yet representative) models of the human head ([Makris et al., 2008](#); [Christ et al., 2010](#)) are more practical, yet with an appropriate safety margin. The reasonable approach is therefore to select several relevant models to account for a broad spectrum of inter-individual variability, perform all simulations with them and take the worst-case. For instance one can choose: a male adult in the center of the coil, a female adult in the same position and a third one with the subject's head closer to the RF coil, then simulate the SAR deposition for any given MRI sequence and last ensure that the worst case scenario is still under the threshold recommended by the international committees.

A solid but still perfectible alternative method to model-based SAR estimation, based on the postprocessing of  $B_1^+$  maps ([Katscher et al., 2012](#); [Voigt et al., 2012](#)), could fulfill condition **(A)**. This procedure automatically includes the individual patient and the current status of the transmit-channels, overcoming corresponding problems of the generic model-based SAR estimation. The advantage of this  $B_1^+$ -based SAR estimation is counterbalanced by the incomplete knowledge of the spatial magnetic field components, required to accurately

calculate local SAR. Therefore, performing a generic model-based SAR estimation still remains the most frequently used method.

Not satisfying condition **(A)** however makes achievable the fulfillment of condition **(B)**, because as described in ([Graesslin et al., 2012](#)) the SAR prediction concept could be divided in two independent subsequent steps. In the first preparatory step, which is carried out only once, model-related data (e.g. the normalized electric and magnetic fields) are determined via relatively time-consuming numerical simulations. These simulated fields are appropriately pre-processed and stored for the subsequent SAR calculation step. In the second phase, the actual SAR is simulated, as this time the MRI sequence-related parameters are introduced (e.g. RF waveforms). This evaluation is, as opposed to the first one, very short and takes less than a second. SAR prediction and monitoring in the case of pTX will be fully explained and discussed in the next sections.

Condition **(C)** fulfillment is more arduous, as finding an accurate model of temperature increase in biologic tissues is a challenging task. The gold standard method is known as the bioheat Pennes model ([Pennes, 1948](#)), which is basically a generalization of the heat equation of Fourier, applied to living tissues. This model (described in Chapter 5) assumes a constant blood temperature, and was experimentally verified on the living human arm ([Wissler, 1998](#)). This model could presumably work for MRI, yet other safety studies suggest considering the blood temperature as a time-dependent function ([Shrivastava et al., 2011](#)). Temperature simulation could be run quickly with any numerical method available, including the Finite-Difference-Time-Domain (FDTD) method.

Experimental proof of the Pennes' model relevance for MRI could be achieved thanks to MRI thermometry. Still, the temperature increases induced by MRI scans are small and the Proton Resonance Frequency Shift (PRFS) method ([Hindman, 1966](#)) is sensitive to any source of phase disturbance, e.g. breathing ([Boulant et al., 2014](#)). In any case, this method requires some MRI scan time. These concerns lead to lower one's ambitions about the fulfillment of condition **(D)**, because direct temperature measurements thanks to optical probes are clearly invasive. If temperature is right now too difficult to predict and monitor, alternative ways therefore need to be considered.

On the other hand, monitoring the SAR is technically feasible. The key principle is to measure the transmitted power and this way ensures that the predicted global SAR is the energy actually delivered in the subject's tissues. These methods will be detailed in the next section.

Last, condition **(E)** is the responsibility of the system manufacturer, yet the case when the MRI coil is damaged must also be considered.

## 4.2. Methods for SAR prediction and assessment

### 4.2.1. Conventional MRI systems

As previously introduced, conventional MRI systems (without parallel transmission) evaluate the SAR based on the anticipated transmitted power. This assessment typically relies on a single simulation of the RF coil in use, loaded with a human model exposed to a CP mode. This leads to a fixed scaling factor (the so-called “k” factor) between the transmitted power and the maximum local/global SAR, which is tabulated on the console so the system can validate the compliance with a set of pre-defined limits such as those summarized in Section 1.3.2. When the proposed acquisition is expected to exceed these SAR limits, the system will prevent the user from starting the measurement. If the requirements are met, the transmitted power is monitored to ensure that the RF-power remains within the appropriate limits. In the event that any of these power limits is exceeded, the acquisition is terminated. SAR prediction and monitoring for conventional MRI systems is therefore straightforward and only relies on model relevance and power monitoring accuracy.

### 4.2.2. pTX-enabled MRI systems

Introducing a pTX-extension however complicates the SAR evaluation due to the multiplicity of interference scenarios that can occur between the fields produced by the different transmit-channels playing in concert. For a given set of RF-sources in the array, the combination of incident amplitudes and phases can vary over time depending on the pulse design. Consequently, a generalized version of the single-channel SAR Equation (1.14) must be considered:

$$SAR(r) = \frac{1}{T} \frac{\sigma(r)}{2\rho(r)} \int_0^T \left\| \sum_{n=1}^N \alpha_n(t) E_n(r) \right\|_2^2 dt \quad (4.1)$$

This equation now includes a summation over the electric field distributions produced by the N RF sources. For a given pTX excitation pulse, i.e. a combination of complex coefficients  $\alpha_n(t)$ , the ratio between peak local and global SAR can be quite high (Collins et al., 2007). Therefore, in contrast to the conventional systems, it is no longer viable to derive the local and global SAR from a concise set of parameters (Mao et al., 2007). Nonetheless, based on the maximum ratio between peak local and global SAR, a conservative generalization of the



conventional RF safety method is possible (Collins et al., 2007). However, this results in a large overestimation of the actual SAR, severely restricting pTX applications. To remedy this situation, Equation (4.1) has to be evaluated for every RF pulse scenario, and the results compared to the guidelines. In theory, only those acquisitions that are in compliance with the RF safety limits then should be allowed by the system.

In practice, only predicting the SAR before the measurement is not sufficient to fully guarantee patient safety. Indeed, without validating the implemented RF waveforms on the scanner, the actual interference patterns may deviate from the anticipated and result in substantially different SAR distributions. This is true not only for the amplitudes but also for the relative phases of the independent channels. This is why simply limiting the transmitted power is not sufficient, unless some extra safety margins are taken (see Section 4.4.1.)

Many methods for SAR assessment are available in the literature (Collins et al., 2007; Brunner et al., 2008; Gagoski et al., 2009; Graesslin et al., 2009a; Boulant et al., 2011), with some deriving more conservative power limits than others. The resulting safety margins in general depend on the monitoring equipment available, which must confirm all the information used in the SAR calculation (amplitude, phase, power, etc.), and on the accuracy of the simulated field maps.

The next section of this chapter describes NeuroSpin's endeavors to validate the electromagnetic simulations and characterizations of the transmit array coil presented in Section 3.1.4. via  $B_1^+$  measurements (remembering that  $B_1^+$  is the only electromagnetic field easily measurable with MRI) and magnetic resonance thermometry, in order to provide accurate anticipation of SAR levels during parallel transmission MRI scans.

In a second time, considering that during this thesis, the only monitoring method available was based on the TALES measurements, the online SAR assessment based on time-averaged power measurements method adopted at NeuroSpin will be described.

## **4.3. SAR prediction validation**

### **4.3.1. $B_1^+$ measurements and electromagnetic simulations**

Throughout this work, the finite element method (FEM) was adopted to provide full-wave simulations (HFSS, ANSYS, Canonsburg, PA, USA) corresponding to our home-built 8-element transceiver-array coil (Section 3.1.4) and a MRI phantom (Section 3.2.1). All coil-elements were tuned ideally at 297 MHz corresponding to the proton Larmor frequency at 7 Tesla and matched identically to a 50 Ohm line impedance. However, each dipole resonated at a slightly different frequency due to the interaction with the subject-model placed in the

coil. Electric and magnetic field maps thus obtained were normalized to 1 W incident power for each coil-element and projected onto a 5x5x5 mm Cartesian grid. In contrast to the FDTD method, where the field distribution can significantly be affected by the mesh size, the tetrahedron density relates to the accuracy of the volume boundaries. HFFS has a reliable mesh adaption tool to optimize the mesh density, ensuring reliable field simulations.

The MRI coil is simulated and loaded with a MRI phantom containing a gel with known electromagnetic properties ( $\sigma=0.78$  S/m and  $\epsilon_R=74.3$ ). The position of the phantom is (-0.4cm; 0cm; -0.5cm). The plinth used is made of RF-unabsorbent blue foam. The simulation was stopped after 13 passes of tetrahedrons mesh refinement:

- Final  $\Delta S = \sim 0.01$
- Memory used:  $\sim 112$  GB
- Final number of tetrahedra:  $\sim 2280000$
- Total duration:  $\sim 13$ h

Last, an interpolating frequency sweep was performed in the 280-320 MHz range.

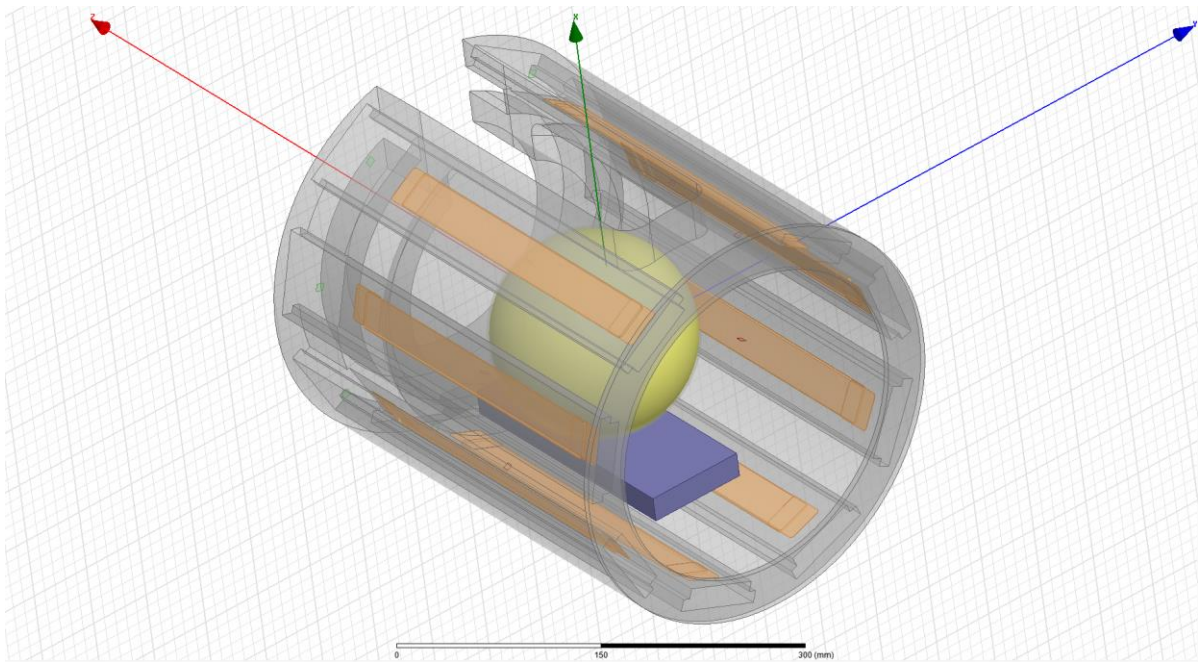


**Figure 4.1:** Screenshot of the simulated MRI coil and phantom in the HFFS software. Position of the phantom ( $\sigma=0,78$  S/m and  $\epsilon_R=74.3$ ) in the coil was set carefully (-0,4cm;0cm;-0,5cm). Simulation characteristics were: 13 iterations,  $\Delta S_{\text{Mag}} = 0.01$ ,  $\Delta S_{\text{Phase}} = 4.5^\circ$ .

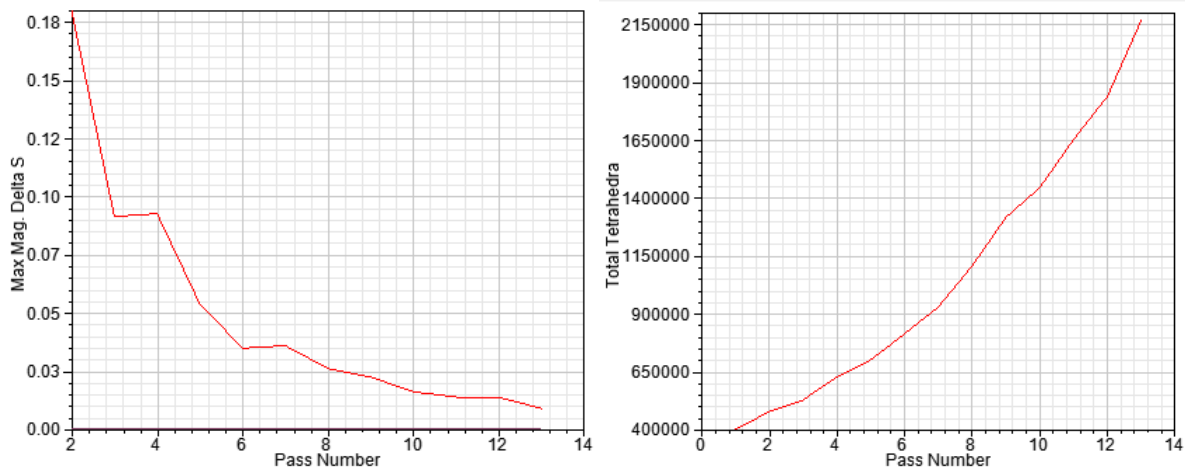


**Figure 4.2:** Electromagnetic simulation characteristics with iterations. **a:** Convergence. **b:** Number of tetrahedra.

The actual flip-angle imaging sequence (Yarnykh, 2007) was employed to map the transmit sensitivity corresponding to each of the coil-elements using an interferometric acquisition method (Brunner and Pruessmann, 2009).  $B_0$  inhomogeneity effects were corrected as proposed in (Boulant et al., 2010). Sequence parameters were: TR: 250 ms, TE: 1.1/2.2/3.2 ms, 5mm isotropic resolution. Comparing the simulated and measured  $B_1^+$  amplitude maps (Figure 4.3.) resulted in correlation factors between simulated and experimental maps well above 0.9 for all coil-elements (Figure 4.4.).

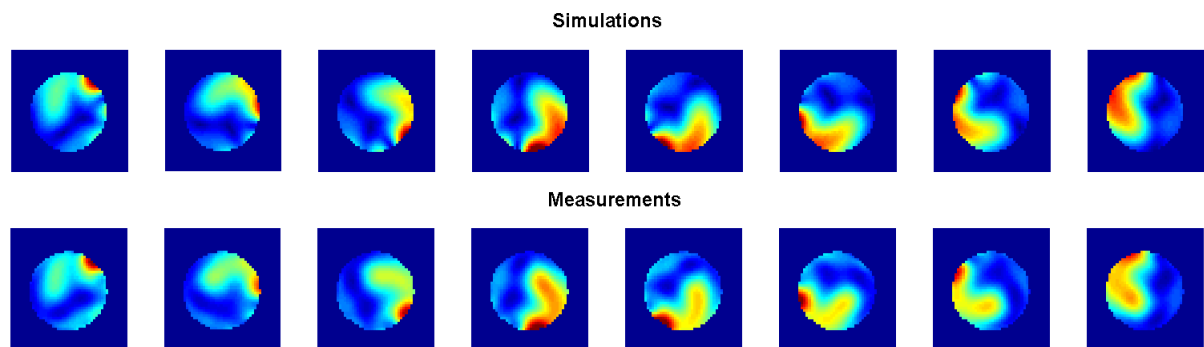


**Figure 4.3:** Simulated (top line) and measured (bottom line) individual magnitude  $B_1^+$  maps for all channels (central axial slices of an agar-gel MRI phantom, first to eighth channel, from left to right). Sequence parameters were: TR: 250 ms, TE: 1.1/2.2/3.2 ms, 5mm isotropic resolution. Simulation characteristics were: 13 iterations,  $\Delta S_{\text{Mag}} = 0.01$ ,  $\Delta S_{\text{Phase}} = 4.5^\circ$ .

The magnitude of these correlation factors is invariant under scalar multiplication. Therefore, this metric only concerns the comparability of the relative spatial variations. To determine the

unknown scalar, the slopes between the measured and simulated maps were calculated. Indeed, whereas during simulation, exactly 1 W of incident power was applied per channel, in practice the actual incident power depends on the amplifier output and cable losses. Because the aforementioned parameters were not included in the simulation, a set of calibration factors must be obtained before the SAR can be evaluated accurately for an arbitrary pulse.

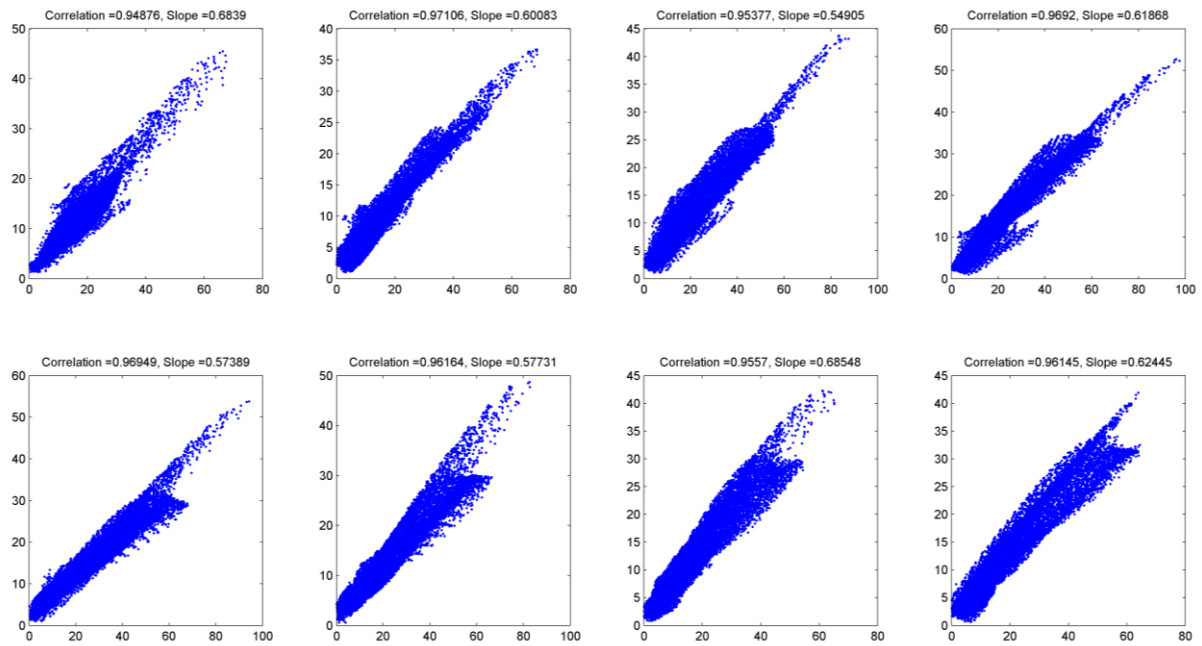


**Figure 4.4:** Correlation between the simulated and measured transmit-sensitivity maps (magnitudes). The scatter plots are showing the correlation for every voxel of the phantom. Corresponding correlation factors and slope are included in the top of each subfigure (first to eighth channel, from left to right).

Nevertheless, demonstrating excellent correspondence between measured and simulated magnitude distributions alone is not sufficient to validate the electromagnetic simulations with high confidence (Alon et al., 2011). Therefore, additional verifications were performed by incorporating the relative transmit-phase, for which good correspondences were found:

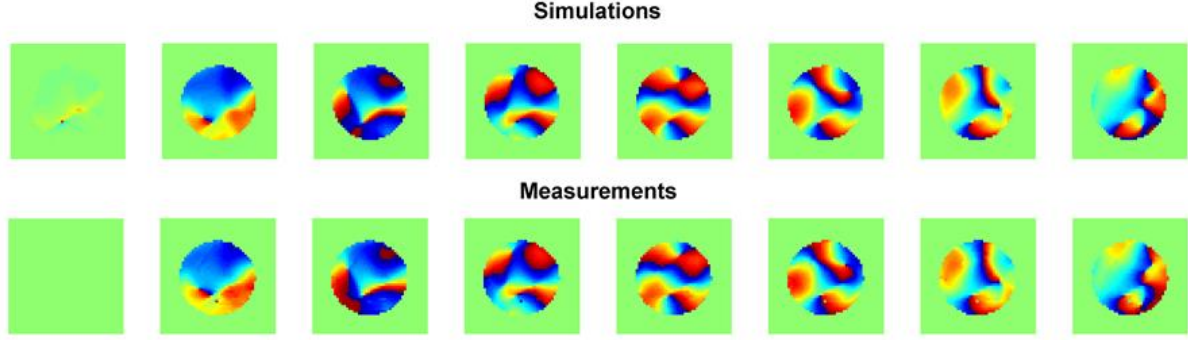


**Figure 4.5:** Simulated (top line) and measured (bottom line) individual relative phase  $B_1^+$  maps for all channels (central axial slices of an agar-gel MRI phantom, first to eighth channel, from left to right). Sequence parameters were: TR: 250 ms, TE: 1.1/2.2/3.2 ms, 5mm isotropic resolution. Simulation characteristics were: 13 iterations,  $\Delta S_{\text{Mag}} = 0.01$ ,  $\Delta S_{\text{Phase}} = 4.5^\circ$ .

#### 4.3.2. MRI Thermometry and temperature simulations

Incorporating the previously found calibration factors, the simulated E-fields corresponding to the phantom were adopted to simulate the expected temperature rise in the phantom by solving numerically (FDTD method) the heat equation:

$$\rho(r)C_p(r)\frac{\partial T(r)}{\partial t} = k\Delta T(r) + \rho(r)\text{SAR}(r) \quad (4.2)$$

where  $\rho$  is the density in  $\text{kg/m}^3$ ,  $C_p$  the specific heat in  $\text{J/kg/K}$ ,  $T$  the local temperature in Kelvin and  $k$  the thermal conductivity in  $\text{W/m/K}$ . Corresponding measurements based on the proton resonance shift method (Equation 4.3) ([Hindman, 1966](#); [Kuroda et al., 1997](#)) were performed on the phantom:

$$\Delta T = \frac{\Delta\phi}{2\pi\alpha TE} \quad (4.3)$$

The frequency shift coefficient  $\alpha$  was first measured for our setup thanks to several temperature measurements with thermal probes. MRI phase measurements stability was evaluated acquiring ten consecutive GRE sequences, with no significant drift reported. The heating protocol was then as following:

- Phantom brought at thermal equilibrium.

- One “Reference” GRE sequence (TR: 33 ms, TE: 24 ms).
- RF only without imaging gradients (V= 180 V, 5% duty cycle, duration: 10 minutes).
- One “Final” GRE sequence (similar to reference).

When comparing data (Figure 4.6.), simulations underestimate the peak rise by 5%, in agreement with the discrepancies observed in the  $B_1^+$  measurements.

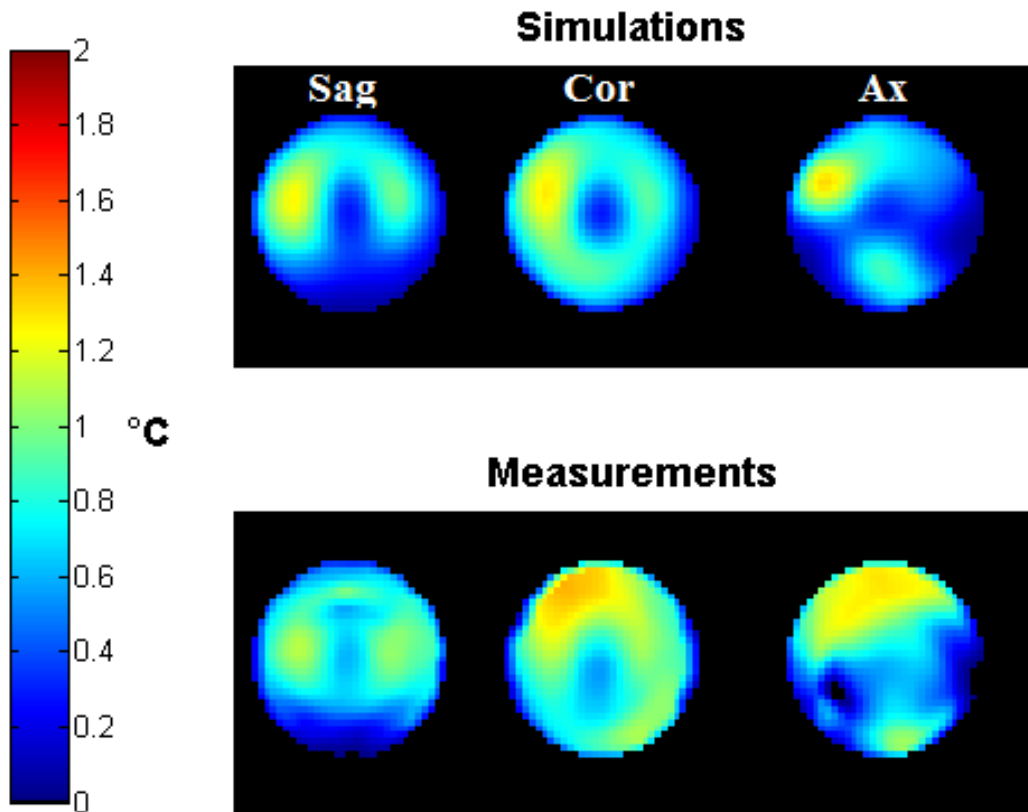


**Figure 4.6:** Temperature rise comparisons between simulated temperature rise maps and measured ones thanks to MRI thermometry (PRFS method). Simulations underestimate the peak rise by 5%.

#### 4.4. Online SAR assessment based on time-averaged power measurements

After validating the simulations necessary to assess the SAR distribution corresponding to our particular setup, the electric fields produced in realistically positioned anatomically accurate human head models were evaluated. For this purpose, the head and shoulders of

the Ansoft human body model (Aarkid, East Lothian, Scotland) were extracted to provide an 8-anatomical-tissue human head model. In addition, the “Ella” (26-year-old woman) model from the “Virtual Family” (Christ et al., 2010) was converted for use in HFSS. Last, a realistic man model was generated thanks to MRI data (Makris et al., 2008), as fully described in Chapter 5. For each of these objects the outer-surface was triangulated by means of in-house-developed code. Consequently, decimation and file conversion were performed with the commercial tool VR-Mesh Studio (VirtualGrid, Seattle, WA, USA) before loading the models into HFSS. Based on these simulated field-maps, the SAR was evaluated with the following method to derive appropriate time-averaged power limits.

#### 4.4.1. Methods

Because the time-averaged power monitors do not allow the relative phase between RF-channels to be evaluated, all possible phase combinations have to be covered so as not to underestimate the true deposited SAR. One way to facilitate this is to assume constructive interference of the E-fields at every point in space. Starting from Equation (4.1) the corresponding upper limit of the SAR expressed in W/kg is the following:

$$\text{SAR}(r) \leq \frac{1}{T} \frac{\sigma(r)}{2\rho(r)} \int_0^T \left( \sum_{n=1}^N \|\alpha_n(t) \mathbf{E}_n(r)\|_2 \right)^2 dt \quad (4.4)$$

This expression depends on the conductivity  $\sigma$ , the density  $\rho$ , the electric field distribution  $\mathbf{E}$  inside the subject, the complex coefficients  $\alpha_n$  of the RF-waveform played on the  $n$ th coil channel, and the time of integration  $T$  during which instantaneous energy deposition is averaged.

A first quite simple safety assessment considers the two following quantities: the worst-case local 10g-averaged SAR when assuming constructive interference of the E-fields at every point ( $\text{SAR}_L$ ), and the global SAR corresponding to the cumulative forward power divided by the exposed body mass ( $\text{SAR}_W$ ). The factor  $k$  between the aforementioned parameters is:

$$k = \frac{\text{SAR}_L}{\text{SAR}_W} \quad (4.5)$$

Assuming that the power is equally distributed over all available transmit-channels, a conservative time averaged power limit ( $P_{\text{lim}}$ ) can be deduced if  $k$  is already known for a given RF coil:



$$P_{\text{lim}} = \frac{0.9 \text{ SAR}_{\text{lim}}}{N} M \quad (4.6)$$

where  $N$  is the number of transmit-pathways,  $M$  is the head mass, and  $\text{SAR}_{\text{lim}}$  is the local SAR limit specified in the guidelines (IEC, 2010). To take the approximately  $\pm 10\%$  accuracy of the power meters into consideration, the enforced limits are scaled down by a factor 0.9. For simplicity, and to provide an additional safety margin, both the 10-s and 6-min time averaged power limits are restricted to the more conservative guidelines corresponding to the 6-min SAR limits. Furthermore, a conservative average head mass of 5 kg is assumed to provide a subject independent power limit. Assuming constructive interference, no cable loss, a complete absorption of the incident power by the head, and a relatively light average head, is clearly unphysical but allows deriving a very conservative but usable time-averaged power constraint.

Omitting the assumption that the energy is distributed evenly among channels, a less restrictive yet also conservative approach can be derived to enforce compliance with the SAR guidelines (Boulant et al., 2011). Expanding equation (4.4) gives:

$$\text{SAR}(r) \leq \frac{\sigma(r)}{2\rho(r)} \left( \sum_{i=1}^N \|\mathbf{E}_i(r)\|_2^2 \frac{1}{T} \int_0^T \alpha_i(t)^2 dt + R(r, t) \right) \quad (4.7)$$

where the second term  $R$  is the sum of the cross products for all channels:

$$R(r, t) = \frac{2}{T} \left( \sum_{i \neq j}^N \|\mathbf{E}_i(r)\|_2 \|\mathbf{E}_j(r)\|_2 \int_0^T |\alpha_i(t)| |\alpha_j(t)| dt \right) \quad (4.8)$$

Calling  $P_n$  the average power of the  $n^{\text{th}}$  RF pulse:

$$P_n = \frac{1}{T} \int_0^T \alpha_n^2(t) dt \quad (4.9)$$

and using the Cauchy-Schwartz inequality, the following upper bound of the SAR is obtained:

$$\text{SAR}(r) \leq \frac{\sigma(r)}{2\rho(r)} \left( \sum_{i=1}^N \|\mathbf{E}_i(r)\|_2^2 P_i + 2 \sum_{i \neq j}^N \|\mathbf{E}_i(r)\|_2 \|\mathbf{E}_j(r)\|_2 \sqrt{P_i P_j} \right) \quad (4.10)$$



This way, tailored to the set of RF waveforms at hand, a set of appropriate average power limitations can be derived for each one of the available transmit-channels. The calculation depends only on the average power of each pulse so that their shape is irrelevant and real-time amplitude monitoring is not required. This computation constitutes an upper bound of the SAR that yields in general a mild 25% overestimation of the value that would be obtained if the true waveforms (but still ignoring the phases) were taken into account (Boulant et al., 2011). Although this approach again results in an overestimation of the SAR, it is significantly less restrictive than considering the maximum local to global SAR ratio.

#### **4.4.2. Practical implementation**

In order to use the above proposed SAR assessment method for pTX MRI scans, the time-averaged power limits for every coil channel have to be re-evaluated based on the tailored RF pulses to be played. To this end, the team SAR assessment tool (Figure 4.7.), referred to as “CEASAR” (Cloos et al., 2010b), evaluates both the global and local 10g-averaged SAR over several pre-simulated data sets. Each one of them contains the simulated fields corresponding to all of the transmit elements in the presence of several human head models. In addition, a pre-calculated “averaging-matrix” is included to facilitate rapid evaluation of the corresponding 10g-averaged SAR. Here the cuboid approach has been retained, to create an averaging matrix from the density distribution with a simple region-growing algorithm. First the borders of a cuboid centered on the voxel of interest are expanded cyclically in all 6 directions. When more than 10-g is contained, the other 5 extension directions are probed to provide a volume as close as possible to 10-g. The averaging matrix is calculated only once.

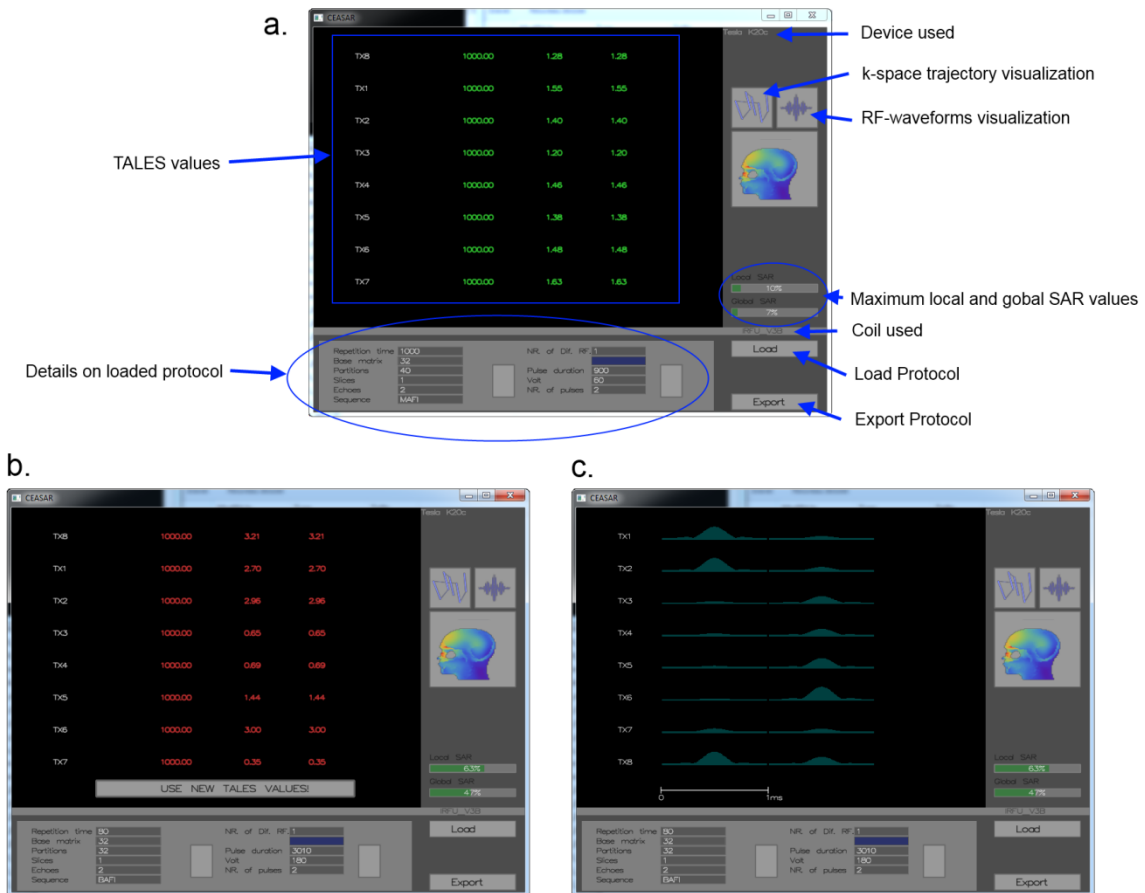


**Figure 4.7:** Screenshots taken from CEASAR. **a:** The main screen, showing a default protocol, in compliance with the SAR guidelines. Main features are indicated with arrow and labels. **b:** Example of a protocol with arbitrary pTX RF-waveforms in compliance with the SAR guidelines, but which requires the time-averaged power-limits to be updated. **c:** Alternative screen with the arbitrary pTX RF-waveforms. The k-space trajectory could also be shown.

Before the exam, a default protocol is first evaluated to obtain a set of initial time-averaged power limits for each of the individual transmit-channels (same energy on all channels). These limits typically facilitate all the initial calibration acquisitions such as  $B_0$ -shimming or transmit-sensitivities mapping. Nevertheless, every time a new protocol including tailored pTX RF pulses is prepared, CEASAR evaluates the corresponding SAR and, if necessary, provides an appropriate set of alternative time-averaged power limits. The possibility to set different average power limits on different channels gives additional flexibility in pulse design, while strictly enforcing safety. When excessive SAR is predicted, the option to increase the repetition time or decrease the voltage is provided. In any case, only protocols that passed the CEASAR evaluation could be played on the scanner. This is effectively enforced by only

copying validated protocols to the slave-system used to operate the pTX extension. During acquisitions, the power out of the amplifiers is measured through the TALEs. In the event that one of the limits is exceeded, the acquisition is terminated.

#### **4.4.3. Future SAR monitoring**

As more and more parallel-transmission-enabled 7 Tesla MRI scanners are available in the world, a robust and less conservative method for local SAR prediction and monitoring (and associated hardware technology) is needed. To answer to this need, the recently updated pTX-systems now provide new means for online RF supervision, whose capabilities consist of two subsystems. One subsystem is dedicated for global power supervision, the other for local SAR supervision. The first subsystem relies as before on the TALEs, which measures global power and are phase insensitive. The forward and backward power of each transmit channel is detected and average power is updated every 10  $\mu$ s. Whole body SAR is calculated from the absorbed RF power divided by the body weight.

As explained above, evaluating peak local SAR for a particular waveform, with the help of pre-simulated anatomical models, is conventionally performed by superposing the time-dependent electrical field vectors that are caused by the individual transmission channels, evaluating the power density and the local averaging values for peak spatial SAR according to the SAR standards (IEC, 2010). The VOPs (Virtual Observation Points) (Eichfelder and Gebhardt, 2011; Lee et al., 2012) concept helps to perform this evaluation very rapidly, by using only a limited set of matrices that still provide a conservative estimation of local SAR when the actual multi-channel RF waveform is evaluated, and was therefore adopted. The VOPs are generated by expressing the local power density as a quadratic form. The simulated local electrical fields and the local conductivities are combined to local matrices (Graesslin et al., 2012). Local SAR prediction as well as online supervision is then based on these VOPs. The forward and reflected RF signals (phase and amplitude) are measured with directional couplers in order to monitor the system. Even if this method is provided by the manufacturer, it is still the responsibility of the user to ensure a true prediction of the local SAR with accurate simulated models.

## **5. Thermal simulations in the human head for high field MRI using parallel transmission**

This Chapter has been accepted for publication as: Massire A, Cloos MA, Luong M, Amadon A, Vignaud A, Wiggins CJ, Boulant N. Thermal simulations in the human head for high field MRI using parallel transmission. *Journal of Magnetic Resonance Imaging* 35, 1312-1321 (2012).

The methods & principles contained in this chapter were also published as an abstract in the proceedings of the Annual Meeting of the International Society for Magnetic Resonance in Medicine 2012.

## Abstract

**Purpose:** To investigate, via numerical simulations, the compliance of the specific absorption rate versus temperature guidelines for the human head in magnetic resonance imaging procedures utilizing parallel transmission at high field.

**Materials and Method:** A combination of finite element and finite-difference time-domain methods was used to calculate the evolution of the temperature distribution in the human head for a large number of parallel transmission scenarios. The computations were performed on a new model containing 20 anatomical structures.

**Results:** Among all the radiofrequency field exposure schemes simulated, the recommended 39 °C maximum local temperature was never exceeded when the local 10-g average SAR threshold was reached. On the other hand, the maximum temperature barely complied with its guideline when the global SAR reached 3.2 W/kg. The maximal temperature in the eye could very well rise by more than 1 °C in both cases.

**Conclusion:** Considering parallel transmission, the recommended values of local 10-g SAR may remain a relevant metric to ensure that the local temperature inside the human head never exceeds 39 °C, although it can lead to rises larger than 1 °C in the eye. Monitoring temperature instead of SAR can provide increased flexibility in pulse design for parallel transmission.

## 5.1. Introduction

For any clinical applications exposing the subject to radiofrequency (RF) electromagnetic fields including Magnetic Resonance Imaging (MRI), regulating committees such as the International Electrotechnical Commission (IEC) have issued guidelines to ensure patient safety. The primary biological parameter of interest being the temperature, to avoid local thermal damage or thermoregulatory problems, it is specified in the latest guidelines (IEC, 2010) that the localized temperature in the head should not exceed 39 °C in the “normal” mode, and that care should be taken to limit the temperature rise in the eye to 1 °C when localized transmit-coils are used (IEC, 2010). Because local temperature is generally difficult to assess, more tractable specific absorption rate (SAR) thresholds were derived to ensure compliance with the temperature guidelines. For volume coils, head average (or global) and 10-g average SAR limits of 3.2 and 10 W/kg respectively were redundant quantities, the former being implied by the latter via calculations based on a simplified model (Athey, 1989; Hoult and Lauterbur, 1979; ICNIRP, 2004). The model thereby predicted that the temperature rise of any small unperfused sphere such as the eye would not exceed 1 °C and that global SAR was a good guide to ensure safety. It was furthermore in agreement with measurements performed on anesthetized sheep at 64 MHz (Barber et al., 1990). Although these thresholds have been challenged at different field strengths via numerical simulations (Collins et al., 2004; Wang et al., 2007a), the SAR limits seem to have remained conservative compared to the temperature ones. Consistent with the IEC guidelines, it was shown that compliance with the global SAR limit only was no longer sufficient when using surface coils (Collins et al., 2004).

Performing MRI experiments with higher static magnetic fields allows larger signal to noise ratios to be obtained. Due to the shortening of the RF wavelength corresponding to the proton Larmor frequency, the community has been facing the increasingly challenging problem of  $B_1$  field inhomogeneity. This phenomenon, if not addressed, can yield zones of shade and significant losses of contrast across the image (Van de Moortele et al., 2005). A substantial methodological leap to overcome this problem occurred with the development of parallel transmission (Grissom et al., 2006; Katscher et al., 2003; Zhu, 2004), which consists of placing an array of transmit-elements around the subject and whose corresponding waveforms can be independently modulated in amplitude and phase. The additional degrees of freedom provided by this method then allow for improved mitigation of the  $B_1$  inhomogeneity via optimization algorithms, but significantly complicate SAR management. Nonetheless, driven by the potential applications of parallel transmission, considerable efforts in the predictions, control and optimizations of SAR have been made (Brunner and

[Pruessmann, 2010](#); [Graesslin et al., 2008](#); [Zelinski et al., 2007](#)). Despite this new complex technology and the multifactorial dependence of temperature on SAR ([Collins et al., 2004](#)), to our knowledge little has been done to confirm whether or not the SAR guidelines were still applicable in this context to guarantee that the temperature limits were not exceeded.

In this paper, we attempt to answer this question via numerical simulations on a human head model at the RF frequency used at 7 Tesla, i.e. 297 MHz, using finite elements and finite difference time domain (FDTD) techniques for the electromagnetic and temperature calculations respectively. The model of the coil used was a home-made eight-channel transceiver coil that has been used at numerous occasions in vivo ([Cloos et al., 2012a](#)). Temperature evolution throughout the head was calculated by integrating the Pennes' bioheat equation ([Pennes, 1948](#)), including the physiological responses with respect to temperature, for 1000 parallel transmission scenarios corresponding to random static RF configurations. For comparison, we also simulated the synthesized circularly polarized (CP) mode as a tentative approach to reproduce some results obtained previously for volume coils. Finally, we computed the evolution and distributions of the temperature during realistic parallel transmit RF exposures corresponding to standard sequences not only to gain additional understanding of heating during a real MRI exam, but also to foresee possible benefits in using temperature monitoring rather than SAR monitoring in parallel transmission.

## 5.2. Materials and Methods

### 5.2.1. Head model

In this study, a high-resolution MRI-based numerical model of the human head was adopted based on the data reported in ([Makris et al., 2008](#)). This original model was constructed from T1-weighted images acquired on a 1.5 T scanner, with a spatial isotropic resolution of 1 mm<sup>3</sup>. Subsequently, 49 anatomical structures entities (ASE) were identified by a certified neurosurgeon and classified by their electrical properties at 300 MHz.

We converted this voxel-based model into a surface-based one so that it could be imported by the electromagnetic finite-elements simulation software we used (HFFS, Ansys, Canonsburg, PA). To this end, a surface reconstruction algorithm was implemented in Matlab (The MathWorks, Natick, MA). Each individual entity was identified by its relative permittivity. The resultant point cloud was hollowed out and then meshed using a triangulation algorithm based on Delaunay's method ([Szczerba et al., 2010](#)). In order to constrain the number of tetrahedrons required during finite-element simulation, decimation and smoothing were performed using VRMesh (Virtual Grid, Bellevue City, WA).

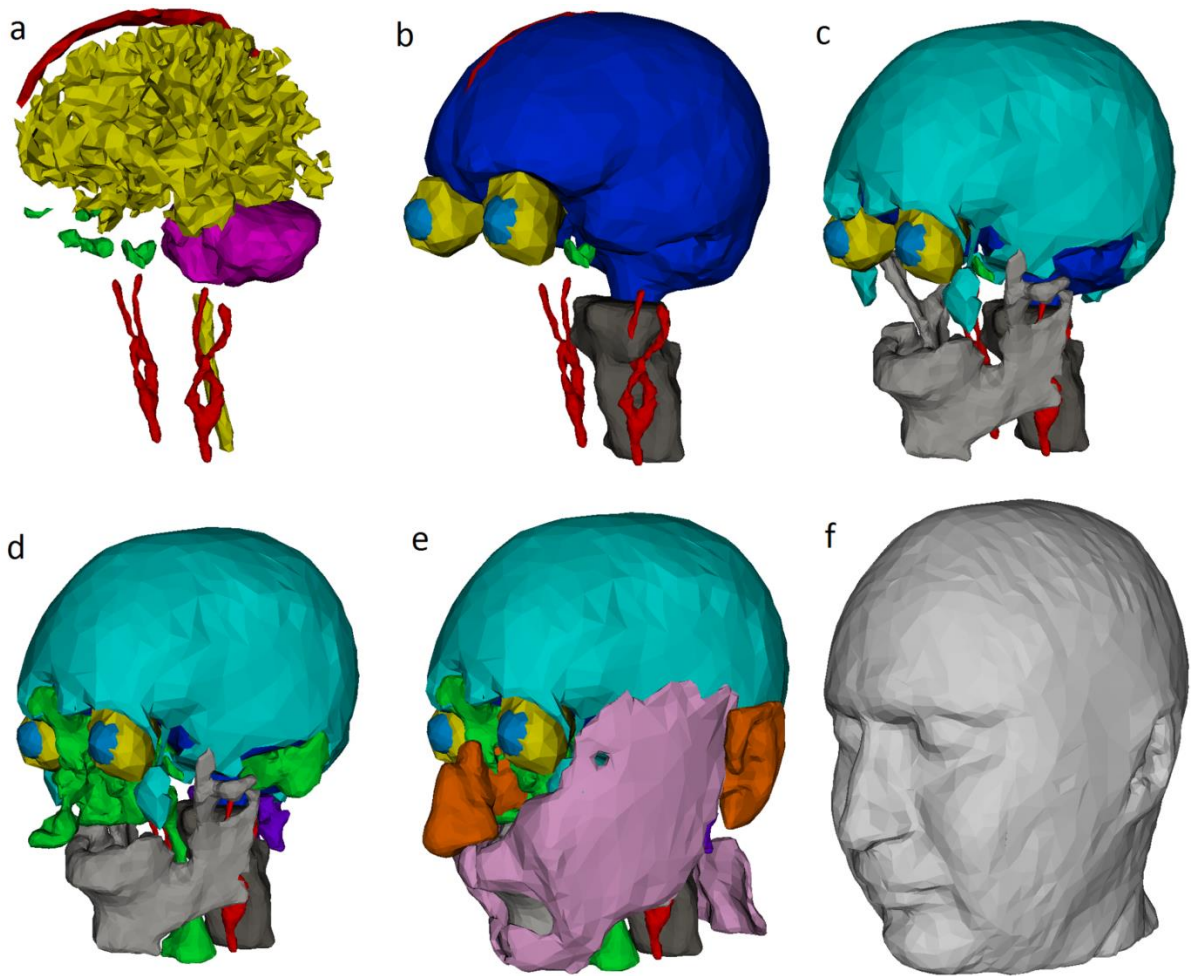


**Figure 5.1:** 3-D view of head model. **a:** White Matter (yellow), blood vessels (red), nerves (green) & Cerebellum (purple). **b:** Grey Matter (dark blue), orbital fat (yellow), eyes (blue), vertebral column (black). **c:** Skull (cyan), facial bones (gray). **d:** Air & mastoid cells (green), adipose (purple). **e:** cartilage (orange), subcutaneous muscles (pink). **f:** Whole model.

At this stage many ASEs could be merged because they shared identical electrical and thermal properties. Memory limitations during finite element simulation further constrained the number of ASEs to 20. In order to have a representative load in the coil, we also added shoulders using the model provided by Aarkid (East Lothian, Scotland) with single tissue properties that we chose to be those of the skin (whose properties appear to be the average ones), as it was shown recently that the precise anatomy in that region was relatively unimportant for SAR calculations in the head (Wolf and Speck, 2011). Electrical and thermal properties were taken from the literature (Makris et al., 2008; Wang et al., 2007a). The different layers of the skull bones were merged together and their physical constants were averaged according to their volume proportion. Figure 5.1 shows different views of the resulting surface-based model while Table 5.1 provides the 20 ASEs and their respective



electrical and thermal properties. In the end, because of the complexity of the procedure and the finite amount of memory available, the initial voxel-based model could not be exactly preserved. Despite the slight differences, it was however deemed realistic and relevant to conduct this study.

**Table 5.1:** Electrical and thermal properties of the 20 anatomical structures used in electromagnetic and thermal calculations

ASE	$\rho$ kg/m <sup>3</sup>	$\sigma$ S/m	$\epsilon_r$	k W/m/K	Cp J/kg/K	Q <sub>0</sub> W/m <sup>3</sup>	B <sub>0</sub> W/m <sup>3</sup> /K
Grey matter	1030	0.69	60	0.57	3700	7100	45090
White matter	1030	0.41	43.77	0.5	3600	7100	15925
Cerebellum	1030	0.97	59.7	0.57	3700	7100	37630
CSF	1010	2.22	72.73	0.62	4200	0	0
Adipose	920	0.07	11.74	0.25	2500	300	1700
Air	1.3	0	1	0.03	1005	0	0
Eyes (humors)	1010	1.51	69.01	0.6	4200	0	0
Blood vessels	1000	1.31	65.65	0.46	3553	1600	9000
Facial bones	1850	0.14	18.3	0.4	1300	590	3300
Skin	1100	0.64	49.82	0.42	3500	1620	8065
Ears	1100	0.55	46.77	0.47	3500	1600	9000
Skull bones	1830	0.12	16.57	0.4	1300	610	3400
Mastoid cells	1.3	0	1	0.03	1005	0	0
Muscles	1040	0.79	58.97	0.5	3600	480	3360
Nasal structures	1100	0.55	46.77	0.47	3500	1600	9000
Nerves	1040	0.41	36.9	0.46	3500	7100	40000
Orbital fat	920	0.07	11.74	0.25	2500	300	1700
Eyes (retina, sclera)	1170	0.95	58.9	0.58	4200	0	0
Spinal cord	1040	0.41	36.9	0.46	3500	7100	40000
Subcutaneous tissues	980	0.43	35.35	0.47	3550	900	4000

CSF = Cerebrospinal fluid.

ASE = Anatomical Structure Entities

## 5.2.2. Coil design and electromagnetic simulations

The head coil used in this study consisted of eight stripline dipoles distributed every 42° on a cylindrical surface with 27.6-cm diameter, leaving an open space in front of the eyes of the patient for fMRI studies. Each dipole corresponds to a balanced strip fed by a so-called geometric matching ([Magill et al., 2010](#)). Thanks to the fair stability of this design regarding

the loading conditions, each dipole does not need to be tuned and matched individually. A unique feed spacing was chosen to match at best all dipoles to a 50-Ohm line impedance when the coil was loaded with the head model. The tuning was obtained using an appropriate value for the two disk capacitors placed at the ends of the strip. Again, the same value was considered for all dipoles. Finally, all dipoles were tuned and matched ideally at 297 MHz corresponding to the proton Larmor frequency at 7 T. However, each dipole resonated at a slightly different frequency due to the interaction of the human head model placed in the center of the coil; but the reflected power coefficient for each channel and the strongest mutual power coupling coefficient were still maintained below 10% at the common field excitation frequency. For each channel, the electric and magnetic complex-valued maps were produced for an incident power of 1 W in HFSS. Results for an arbitrary excitation could then be calculated by linearity. Figure 5.2 presents the final model with the coil.

The mesh used by HFSS to perform the electromagnetic calculations consisted of 1 million tetrahedrons. Special care was taken to have a refined mesh adjacent to the copper surfaces in order to adequately represent potential steep rises in conservative E-fields. The resulting electric and magnetic field maps were interpolated by the software onto a Cartesian grid with a resolution of  $2.5 \times 2.5 \times 2.5 \text{ mm}^3$  for SAR and thermal calculations, which was chosen as a compromise between accuracy and computation time. Good convergence of the temperature at such a resolution was reported in ([Wang et al., 2009](#)). But because the convergence of the peak 10-g SAR appeared to be slower, we repeated SAR calculations at a resolution of  $5 \times 5 \times 5 \text{ mm}^3$  and compared the results.

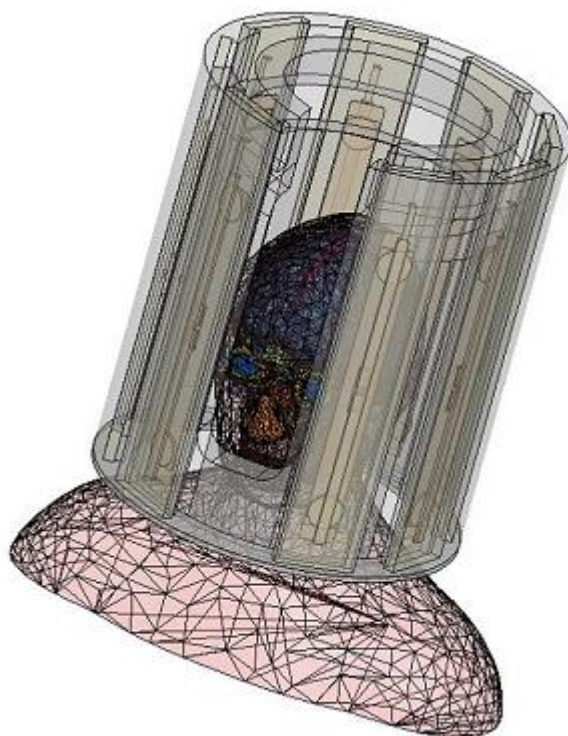


**Figure 5.2:** 3-D view of the whole model. The coil is an 8 channel-transceiver coil with 27.6 cm diameter. The head model includes 20 different anatomy structures entities. Shoulders were added to provide an appropriate load inside the coil.

### 5.2.3. SAR calculation

Local SAR is defined as a function of the local conductivity  $\sigma$ , local mass density  $\rho$ , the pulse duration  $T$  and the local electric field strength  $E$ :

$$SAR(r) = \frac{1}{T} \frac{\sigma(r)}{2\rho(r)} \int_0^T \|E(r, t)\|_2^2 dt \quad \text{with} \quad \vec{E}(r, t) = \sum_{k=1}^8 \alpha_k(t) \vec{E}_k(r) \quad (5.1)$$

where  $E_k$  is the electric field vector map obtained from the excitation of coil element  $k$  alone (1 W incident power) and  $\alpha_k$  is the corresponding waveform (in  $W^{-1/2}$ ). For a given set of  $\alpha_k(t)$ , the global SAR ( $SAR_W$ ) could then be calculated by integrating Eq. [1] over space while we used a region growing algorithm to calculate the SAR 10-g average ( $SAR_L$ ). For most locations, the masses enclosed in the averaging boxes resulted in masses between 9.5 and 10.5 g, thereby obtaining the 5 % required accuracy in the averaging mass (Kozlov et al., 2009). For those locations where we could not obtain such tolerance in the mass, we interpolated linearly two steps in the region growing procedure corresponding to masses smaller than 9.5 g and larger than 10.5 g.

### 5.2.4. Thermal calculations

The temperature within our human head model exposed to electromagnetic fields, was obtained by integrating numerically the Pennes' bioheat equation (Collins et al., 2004; Wang et al., 2007a; Pennes, 1948; Wang and Fujiwara, 1999):

$$\rho(r)C_p(r) \frac{\partial T(r)}{\partial t} = \vec{\nabla} \cdot (k(r) \vec{\nabla} T(r)) + \rho(r)SAR(r) + Q(r) - B(r)[T(r) - T_b] \quad (5.2)$$

where  $\rho$  is the ASE density in  $kg/m^3$ ,  $C_p$  the specific heat in  $J/kg/K$ ,  $T$  the local temperature in Kelvin,  $k$  the thermal conductivity in  $W/m/K$ ,  $Q$  the metabolic rate in  $W/m^3$  and  $B$  the perfusion coefficient in  $W/m^3/K$ . All the parameters in Equation [5.2] are tissue-dependent, and thus spatially dependent. For convenience, we will assume throughout the paper this dependence

and omit their explicit notation. The boundary conditions (convection, sweat and radiation) we used were:

$$k \frac{\partial T}{\partial n} = -h(T - T_a) + \text{SWEAT} \quad (5.3)$$

where  $n$  is the unit vector normal to the surface and  $h$  the effective convective heat-transfer coefficient in  $\text{W/m}^2/\text{K}$ . Due to the small temperature rises encountered here, contribution of the radiation was included in the convection coefficient by linearization for simplicity, yielding in the end a value of  $10.5 \text{ W/m}^2/\text{K}$  (54 % radiation, 46 % natural convection). The blood temperature is  $T_b$ , here considered to be constant in time and equal to the core temperature (i.e.  $37^\circ\text{C}$ ). The ambient temperature of the air surrounding the subject is  $T_a$ , and was set to  $24^\circ\text{C}$ .

Temperature-dependent formulations for sweat, perfusion and metabolic rates were used (Bernardi et al., 2003). Under a temperature of  $39^\circ\text{C}$ , the perfusion rate is only temperature-dependent for the skin. It can be expressed as:

$$B = [B_0 + W_1(T_H - T_{H0}) + W_2\Delta T_S] \cdot 2^{\frac{\Delta T}{6}} \quad (5.4)$$

where  $B_0$  is the basal perfusion rate (see Table 5.1). In this equation, two inputs are used to model the regulation of the blood perfusion coefficient in the skin through vasodilatation: the hypothalamic temperature rise  $T_H - T_{H0}$ , and the average skin temperature rise  $\Delta T_S$ . Coefficients  $W_1$  and  $W_2$  were set to  $17\,500 \text{ W/m}^3/\text{K}^2$  and  $1100 \text{ W/m}^3/\text{K}^2$ , respectively. The exponent in the equation is the local temperature rise. For internal tissues, the blood perfusion coefficient depended on the local tissue temperature only above  $39^\circ\text{C}$ :

$$B = [1 + S_B(T - 312.15)] \quad (5.5)$$

where  $S_B$  is a coefficient set to  $0.8 \text{ K}^{-1}$ . Sweat regulation was modeled similarly as skin perfusion:

$$\text{SWEAT} = [P + W_3(T_H - T_{H0}) + W_4\Delta T_S] \cdot 2^{\frac{\Delta T}{10}} \quad (5.6)$$

with  $W_3$  and  $W_4$  being equal to  $140 \text{ W/m}^2/\text{K}$  and  $13 \text{ W/m}^2/\text{K}$ , respectively. The basal evaporation heat loss from the skin  $P$  was set to  $4 \text{ W/m}^2$ . The metabolic rate was increased with temperature for all ASE as follows:

$$B = Q_0 \cdot (1.1)^{\Delta T} \quad (5.7)$$

An equilibrium temperature distribution was first calculated with no SAR source by integrating Eq. [5.2] (FDTD, 5 sec time-step) for 40 minutes after setting a uniform temperature through the head of 37 °C. We verified that the steady state regime was reached everywhere by inspecting the time evolution of the temperature at a few well-separated locations. This equilibrium temperature distribution was then saved and used as the initial temperature distribution for the RF exposure simulations. Lastly, our thermal simulator was validated via a comparison with an analytical solution on a sphere with uniform SAR, and for the spatial and time resolutions specified here.

### 5.2.5. Monte Carlo simulations

To have a representative sample of the possible SAR and heating patterns one may obtain in parallel transmission, we simulated 1000 static RF configurations by generating 8 random phases in  $\alpha_k$  (uniform distribution from 0 to  $2\pi$ ) while keeping their magnitude equal to 1 (see Eq. [5.1]). The SAR maps, with their corresponding global and peak 10-g averages were calculated and saved. The statistics of their ratio was also computed as it is sometimes used in worst-case scenarios ([Collins et al., 2007](#)) or to see possible trends between global-local SAR relationships. The temperature was calculated for ½ hour of RF exposure scaled to correspond either to the global SAR or the 10-g average local SAR limit (separate simulations) specified in the latest IEC guidelines ([IEC, 2010](#)) for the “normal” mode, i.e. 3.2 and 10 W/kg respectively. The maximal absolute temperature as well as the, maximal temperature rise in the head and in the eyes was recorded. The calculations were performed on a standard desktop workstation, with 3.2 GB RAM memory and Intel Xeon duo-core 1.6 GHz, using Matlab. A single run roughly took 7 minutes, yielding approximately a-10 days duration for the 2x1000 scenarios computation.

### 5.2.6. Circularly-polarized mode simulations

As a special case, the CP mode was synthesized by incrementing the phase of each transmitting element according to their azimuthal angle in the transverse plane, with equal magnitudes. The corresponding SAR map, as well as the head and peak 10-g average values were then calculated. Likewise, the temperature throughout the head was computed with respect to time for an RF exposure of 30 minutes after having scaled up the SAR map

so that whatever limit, i.e. global or local, was reached first. With this a comparison of our simulated results with certain theoretical idealizations ([Athey, 1989](#)) and other simulations ([Collins et al., 2004](#); [Wang et al., 2007a](#)) could be attempted. We also repeated the same calculation by scaling up the SAR map so that a head average of 4 W/kg was obtained, to compare with some of the experimental results reported in ([Barber et al., 1990](#)).

### 5.2.7. Realistic parallel transmission RF exposure simulations

Although we assume that the Monte-Carlo studies mentioned above offer a representative sample of SAR scenarios, we have simulated the temperature evolution throughout the head for more standard sequences, namely a magnetization-prepared rapid gradient echo (MP-RAGE) ([Bernstein et al., 2004](#)) and an axial multi-slice  $T_1$  gradient recalled echo (T1-GRE) sequence. In the former case, the  $k_T$ -points method, which consists of a limited number of non-selective excitations distributed in 3D  $k$ -space ([Cloos et al., 2012a](#)), was used to design both the inversion (flip angle =  $180^\circ$ , duration = 3.5 ms) and the small tip angle (flip angle =  $12^\circ$ , duration = 380  $\mu$ s) pulses. Optimal control theory ([Xu et al., 2008](#)) was also used to complement the  $k_T$ -points method for the design of the inversion pulse. The parameters of the MP-RAGE sequence were: TR = 2.1 s, TI = 1.1 s, echo spacing of 9 ms and 360 partitions, while the parameters for the multi-slice T1-GRE were: flip angle =  $90^\circ$ , TR = 350 ms, number of slices = 24. For that second sequence, and for each slice, a pulse was designed to homogenize the flip angle using the spokes method ([Saekho et al., 2006](#)) combined with the magnitude least squares optimization technique ([Setsompop et al., 2008a](#)). Three sinc-shapes played back to back, apodized with Hanning windows, each of duration 1 ms and time-bandwidth product 2.7 therefore were optimized in amplitude and phase for each channel, and for each targeted slice. In all cases, the homogenization of the flip angle was targeted over the brain region only and yielded normalized root mean square errors around 5 %.

For both sequences, the SAR maps were calculated and then scaled up so that whichever SAR limit was reached first, i.e. the global or the 10-g average one. Physically, this could simply be obtained by adjusting the repetition time. The temperature was then calculated in six different scenarios: 1) MP-RAGE for 12 minutes, 2) T1-GRE for 12 minutes, 3) MP-RAGE for 6 minutes followed by T1-GRE for 6 minutes, 4) same as before with the time average (over 12 minutes) SAR map, 5) the MP-RAGE for 6 minutes, followed by no RF for 6 minutes, followed by the T1-GRE for 6 minutes, 6) same as before with the time-average (over 18 minutes) SAR map. These durations were chosen to encompass the 6 minute averaging window specified in the guidelines ([IEC, 2010](#)). For the 4<sup>th</sup> and 6<sup>th</sup> cases, the goal

was to check whether temporal averaging (Graesslin et al., 2009b), initially invented to lower SAR values, likewise could be used to lower temperature when considering larger time-scales. In each temperature simulation, the intermittent nature of the RF exposure was not considered as it has been shown that the timescales involved in the thermal dynamics were much longer than the ones involved in such scans (Wang et al., 2007b). As a result the SAR maps were averaged over their corresponding repetition times, and those were used as the source terms in Pennes' bioheat equation.

## 5.3. Results

### 5.3.1. SAR in the human head model

The histogram of the  $SAR_L/SAR_W$  ratios for our Monte-Carlo simulations is shown in Figure 5.3. The mean, standard deviation, maximum and minimum values were 9.2, 2.4, 19.5 and 4.2 respectively. Because of its proximity to the coil elements, the peak 10-g SAR was found in the skin in 66 % of the cases, the remaining 34 % being found in the CSF due to its high conductivity.

We also calculated the global and local SAR results based on the electromagnetic fields exported onto a  $5 \times 5 \times 5 \text{ mm}^3$  grid resolution for the 1000 parallel transmission scenarios. We found a root mean square of the relative error with the 2.5 mm isotropic Cartesian grid of 2.9 % for local 10-g SAR and 0.3 % for the global SAR. If there is a dependence of the results on the resolution, this indicates that they have pretty much converged at this finer resolution.

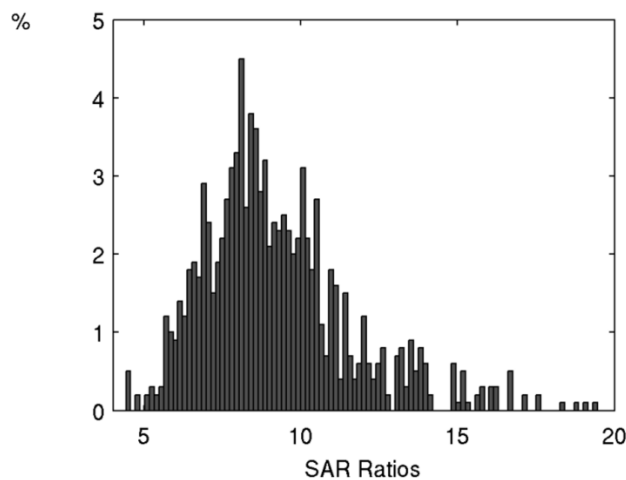


**Figure 5.3:** Histogram of local 10-g SAR over global SAR ratios for the 1000 static RF configurations (mean value: 9.21, standard deviation: 2.38).

### 5.3.2. Temperature distributions for random static RF configurations

Because the minimum  $SAR_L/SAR_W$  ratio was always larger than 10/3.2~3.1, the 10-g average SAR limit was always reached first. In such a case, the local temperature did not exceed 37.7 °C in more than 90 % of the 1000 scenarios (Figure 5.4.a), even after 30 minutes of RF exposure, which is a relatively long duration for an MRI exam, considering a typical scan duty cycle of 50 % (Brix et al., 2001). Only six scenarios yielded maximal temperatures that barely exceeded 38 °C. The corresponding maximum rises in temperature are shown in Figure 5.4.b. There is no clear correlation between these rises and the absolute local temperatures. As far as the eye is concerned, we found that the maximum temperature rise in that region was larger than 1 °C in 20 % of the cases, the shortest duration to reach this value being 7 minutes. As an example, we provide in Figure 5.5 the 10-g SAR maps and the corresponding temperature rises for two extreme  $SAR_L/SAR_W$  scenarios (4.4 and 19.5), where in both cases  $SAR_L = 10$  W/kg.

When the SAR maps were scaled up in order to reach 3.2 W/kg for the head average, over half of them exceeded 38 °C in just 6 minutes of RF exposure, the maximal temperature (Figure 5.4.c) usually rising up to 39 °C for 40 % of the cases after the 30 minutes period. The corresponding maximum rises in temperature are shown in Figure 5.4.d.

To investigate the impact of the dependence of the physical constants on temperature, we repeated a few randomly selected scenarios using only the basal rates. The maximum deviation was around 5 %, showing their small impact in mild RF exposure, in agreement with (Wang et al., 2008).



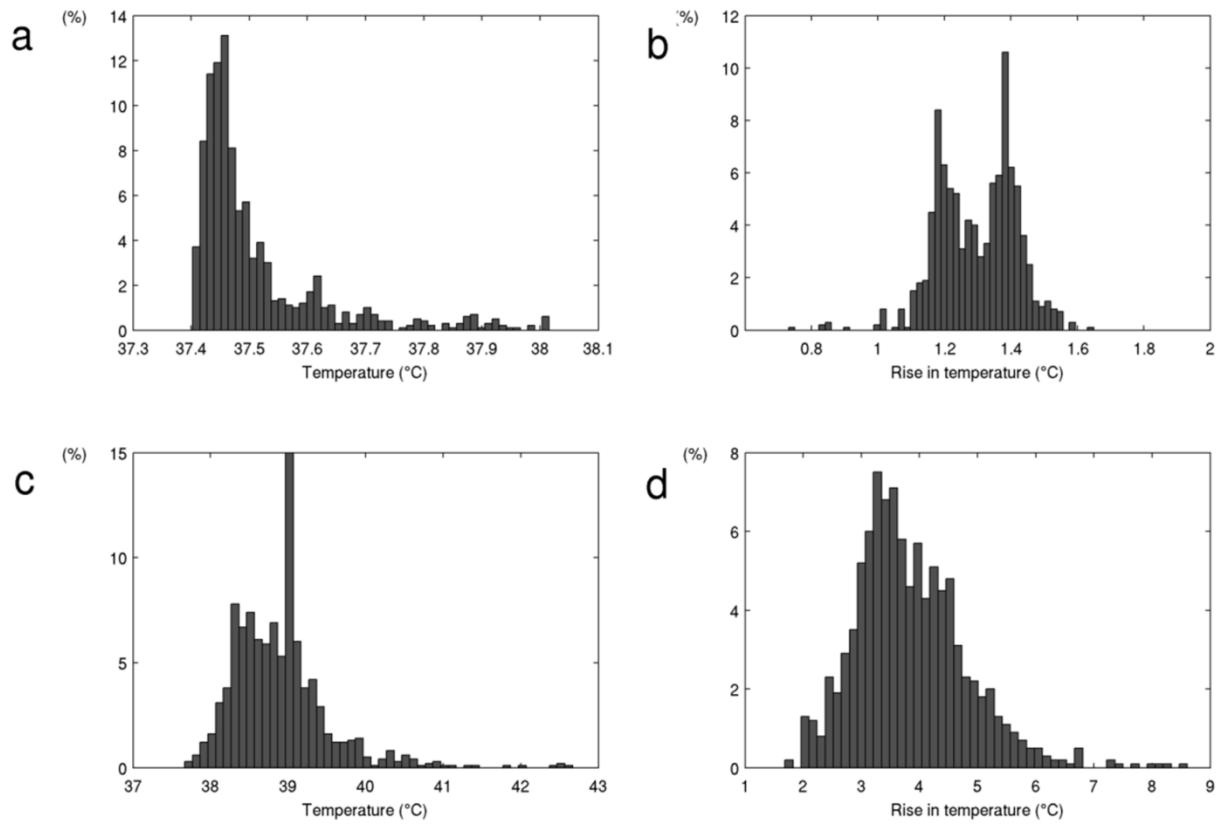


**Figure 5.4:** **a:** Maximum local temperature histogram after 30 minutes of RF exposure when  $SAR_L = 10$  W/kg for the 1000 static RF configurations. **b:** Corresponding maximum rises in local temperature. **c:** Maximum local temperature after 30 minutes of RF exposure when  $SAR_W = 3.2$  W/kg for the 1000 static RF configurations. **d:** Corresponding maximum rises in local temperature.

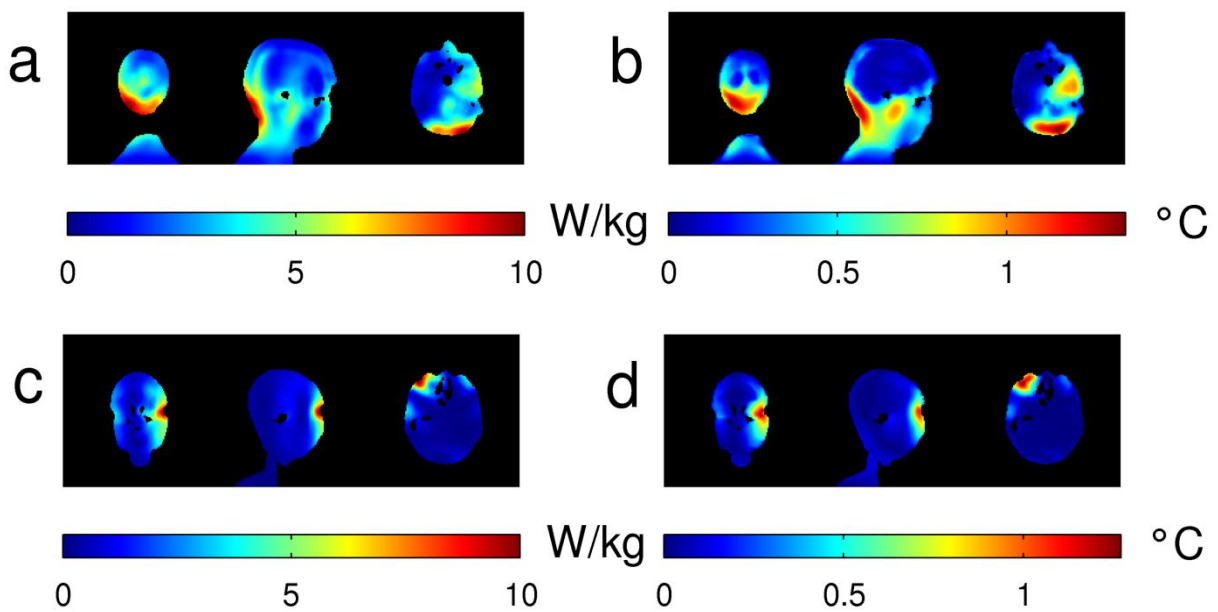


**Figure 5.5:** **a:** Local 10-g average SAR distribution (in W/kg) for a low  $SAR_L/SAR_W$  ratio (4.42) static RF configuration. **b:** Corresponding local rise in temperature (in °C) after a 30 minute RF exposure when  $SAR_L = 10$  W/kg. **c:** Local 10-g average SAR distribution (in W/kg) for a high  $SAR_L/SAR_W$  ratio (19.47) static RF configuration. **d:** Corresponding local rise in temperature (in °C) after a 30 minute RF exposure when  $SAR_L = 10$  W/kg. From left to right in each sub-figure are shown coronal, sagittal and axial slices going through the 10-g SAR hot spot.

### 5.3.3. CP-mode simulations

The SAR values and temperature evolutions were computed for the CP-mode (see  $B_1$  distribution in Figure 5.6.a) in the same conditions. For this particular case, the  $SAR_L/SAR_W$  ratio being found equal to 3.2, i.e. almost equal to  $10/3.2$ , scaling up the SAR map yielded a result where both the local and global SAR limits were equally attained to a good approximation. The CSF situated in the center of the brain absorbed a relatively high amount of power (see scaled local SAR map on Figure 5.6.b and 10-g average SAR map on Figure 5.6.c). Despite thermal conduction, the rise in the central brain region however remained moderate (0.5 °C max) due to perfusion (see Figure 5.6.d). Lastly, when the global SAR was scaled up to 4 W/kg, the maximum temperature rise in the eye was 0.71 °C after 20 minutes, and 0.79 °C after 30 minutes of RF exposure.

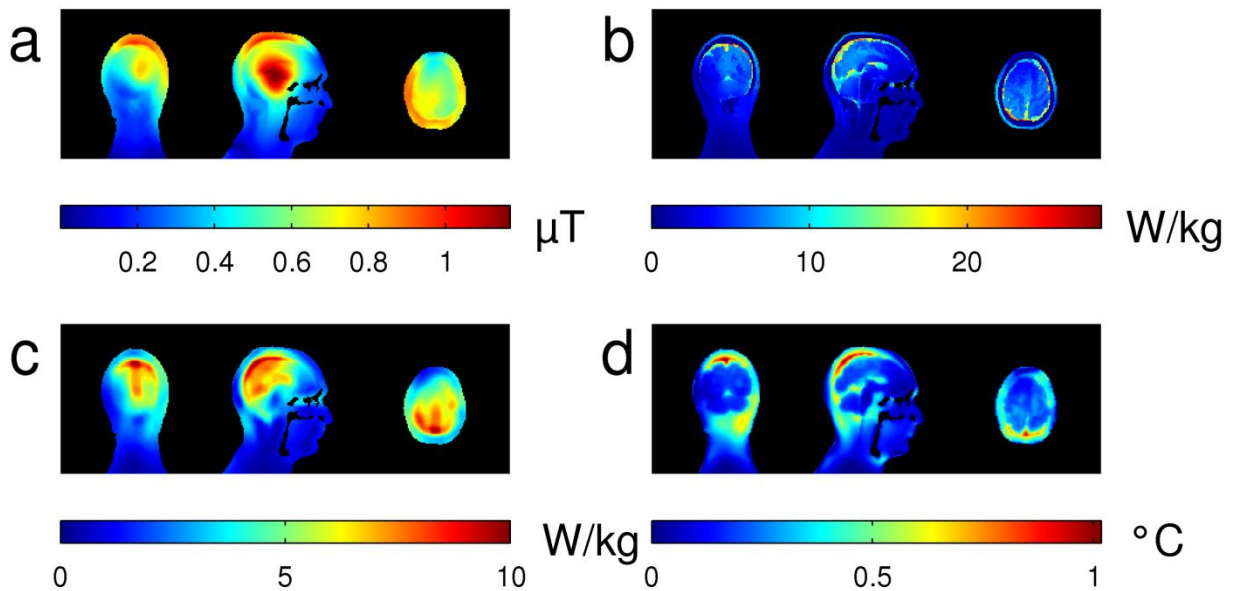


**Figure 5.6:** **a:**  $B_1$  distribution (in  $\mu T$ ) with 1 W of incident power for each coil element. **b:** SAR distribution (in W/kg). **c:** Local 10-g average SAR distribution (in W/kg). **d:** Local rise in temperature distribution (in °C) after a 30 minute CP-mode RF exposure when  $SAR_L = 10$

W/kg and  $SAR_W \sim 3.2$  W/kg. From left to right in each sub-figure are shown coronal, sagittal and axial slices going through the SAR hot spot. The increased SAR due to the high conductivity of the CSF is clearly visible on the sagittal slice.

#### 5.3.4. MRI sequence simulations

The two MRI sequences simulated did not yield temperature rises exceeding individually  $0.8^\circ\text{C}$  after 12 minutes (see Figure 5.7). Local SAR limits were for these two sequences more restrictive than the global ones, with  $SAR_L/SAR_W$  ratios of 3.8 and 5.3 for the MP-RAGE and the  $T_1$ -GRE respectively. All temperature recommendations, even those concerning the eyes, were ensured when the peak 10-g average SAR did not exceed 10 W/kg.

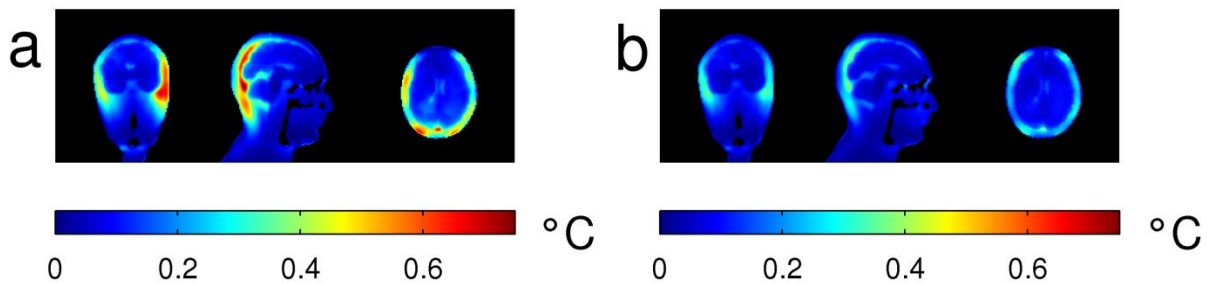


**Figure 5.7:** **a:** Local rise in temperature distribution (in  $^\circ\text{C}$ ) after a 12 minute MP-RAGE sequence. **b:** Local rise in temperature distribution (in  $^\circ\text{C}$ ) after a 12 minute  $T_1$ -GRE sequence. In both cases, the initial temperature was the equilibrium temperature.

When played back to back (6 minutes duration each), the final maximum temperatures were barely changed, due to a relatively rapid thermal equilibration time for the location at which the maximum occurred (see Figure 5.8.a). As shown in Figure 5.8.b, the irradiation including a six minute pause did not influence the final maximum temperature. Perhaps not surprisingly, one can also see that temporal SAR averaging over long time periods can yield different temperature trajectories during the course of the experiment, especially if there is a significant pause between the two acquisitions.

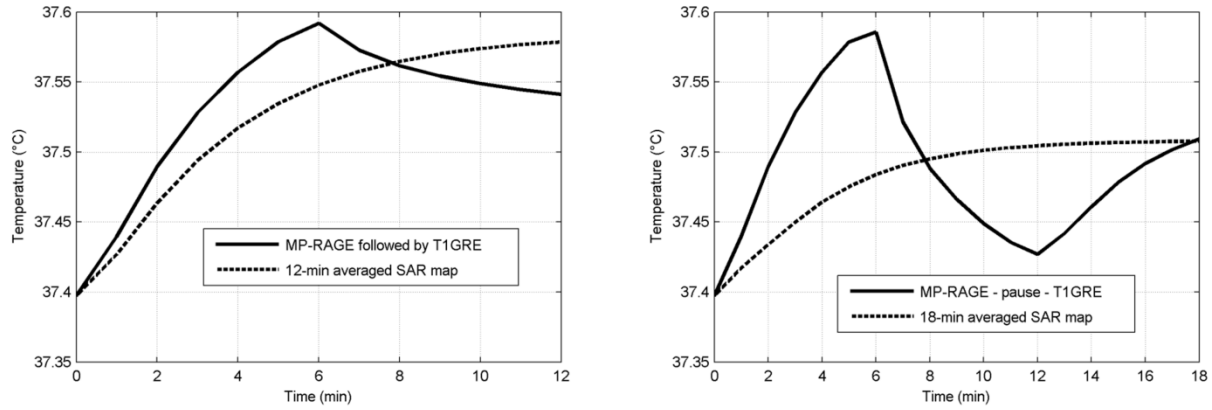


**Figure 5.8: a:** Evolution of the maximal local temperature (in °C) in the head for a 6-minutes MP-RAGE followed by a 6-minutes T<sub>1</sub>-GRE (solid line), and same as before but with the corresponding time-averaged SAR map (dashed line). **b:** Evolution of the maximal local temperature (in °C) in the head for a 6-minutes MP-RAGE followed by no RF for 6 minutes, and by a 6-minutes T<sub>1</sub>-GRE (solid line), and same as before but with the corresponding time-averaged SAR map (dashed line).

## 5.4. Discussion

In this study we have investigated SAR and temperature within the context of parallel transmission at 7 T on a new numerical head model. For that purpose, we have run a series of 1000 SAR and thermal simulations based on random static RF configurations. One could argue that these scenarios do not reflect real experiments. However, given the plethora of degrees of freedom available in Transmit-Sense, it was our hope that such procedure would sample reasonably well the space of SAR maps, the point being mainly to detect a possible flaw in the SAR guidelines.

In agreement with previous results (Collins et al., 2004; Wang et al., 2007a), it was again confirmed that the relationship between SAR and temperature is not straightforward. In areas of high perfusion, such as the brain, high SAR levels often leads to a minimal temperature increase, while in areas of lower perfusion rate, such as muscle or the eyes, temperature may increase significantly even with relatively low SAR inputs. Whereas the local 10-g limit of 10 W/kg throughout this study seemed to be a good guide to ensure that a temperature of 38 °C would almost never be reached, it certainly seems very conservative when considering the new temperature of 39 °C indicated in the latest edition of the IEC guidelines (IEC, 2010). If this temperature is now deemed a safe limit for the “normal” mode, the simulations reported here then show that the SAR constraints could probably be relaxed. On the other hand, we found that even with 10 W/kg as the maximum SAR 10-g average, the maximum

temperature rise in the eye could be above 1 °C. As with surface coils, the simplified model presented in (Athey, 1989) hence does not apply here. When using parallel transmission, this suggests extra caution regarding this organ. The SAR could be possibly decreased in that region by penalizing high powers on the coil elements the closest to it (Cloos et al., 2010a). A coil design may be also helpful in which the coil element spacing is increased near the eyes. The CP-mode was studied to allow us to compare our results to earlier work. When driven as such, the simulations reported here show that this particular coil behaves, as expected, as a volume coil, namely that global SAR is a good guide to ensure patient safety (Athey, 1989), the  $SAR_L/SAR_W$  ratio is close to the theoretical one for a homogeneous sphere (Hoult and Lauterbur, 1979), and that the calculated rise of temperature in the eye of 0.71 °C after 20 minutes is close to the measured value of  $0.8 \pm 0.1$  °C on anesthetized sheep when the global SAR was set equal to 4 W/kg (Barber et al., 1990). Although the measurement was performed on a different species and at a different frequency, this provides reasonable support for our simulated results. Moreover, already at 3 T, SAR demanding sequences such as the turbo spin echo sequence can force the user to implement less than 180° refocusing pulses (Hennig et al., 2003). The results presented here suggest that a higher local SAR threshold and thus 180° pulses could possibly be used, especially given the latest temperature guidelines with head volume coils.

The thermal simulations performed for more realistic MRI sequences revealed three important things. First, the SAR limits may be quite conservative compared to the temperature ones, especially if the new 39 °C limit is considered (IEC, 2010). Secondly, temporal averaging over longer time periods (see Figure 5.8) should not be used in general since the individual SAR maps used as power sources in Equation [5.2] for 6 minutes each yielded different temperature trajectories than observed for the corresponding time-averaged SAR maps. Finally, Figure 5.8 suggests that two MRI sequences whose corresponding thermal steady states do not exceed the recommended maximum temperature could likewise satisfy this criterion when played back to back. This is however merely based on our example and we cannot rule out for the moment the existence of a counterexample. But if this was more general, a thermal analysis could possibly be done separately for each sequence without tracking the whole scan history. Exploiting this principle for RF pulse design would require a deeper understanding of the SAR-temperature relationship. For a start, the dependence on the thermal equilibration time of the organ involved should be further studied (Brix et al., 2002). In pulse design and in parallel transmission, one often needs to make a trade-off between pulse performance and SAR. The first point mentioned above then suggests that significantly more latitude could be gained in pulse design if temperature, instead of SAR, was taken into account. However, because of a larger inter-

individual variability, one would likely need to monitor it online via magnetic resonance thermometry ([Rieke and Pauly, 2008](#)).

All conclusions and observations in this work cannot be guaranteed for other coils, head models and positions. They also rely on the validity of the Pennes' bioheat model. Alternatively, the generic bioheat transfer model reported by Shrivastava et al. ([Shrivastava et al., 2011](#)) likewise could be used. Despite its experimental success in predicting the temperature rise in pigs' brains at 296 MHz and using a head coil (heating period of 3 hours, global SAR of 3 W/kg), further investigations are needed to verify the validity of this model to humans under representative conditions. In particular, the effects of anesthesia, which is known to affect thermoregulatory thresholds and blood flow ([Mount, 1979](#); [Shrivastava et al., 2011](#)), should be isolated during experimental validation. For these reasons, and the good experimental results demonstrated in the human forearm ([Wissler, 1998](#)), we chose to use the Pennes' model.

In conclusion, based on Pennes' bioheat equation, using recommended values of 10 W/kg for 10-g average SAR in parallel transmission seems to indicate that, with our setup, the local temperature inside the human head never exceeds 39 °C (and barely 38 °C) but temperature rises larger than 1 °C may occur in the eye. Monitoring temperature during scans not only is safer but could also provide significantly more freedom in pulse design.

## **6. Design of non-selective refocusing pulses with phase-free rotation axis by gradient ascent pulse engineering algorithm in parallel transmission at 7 T**

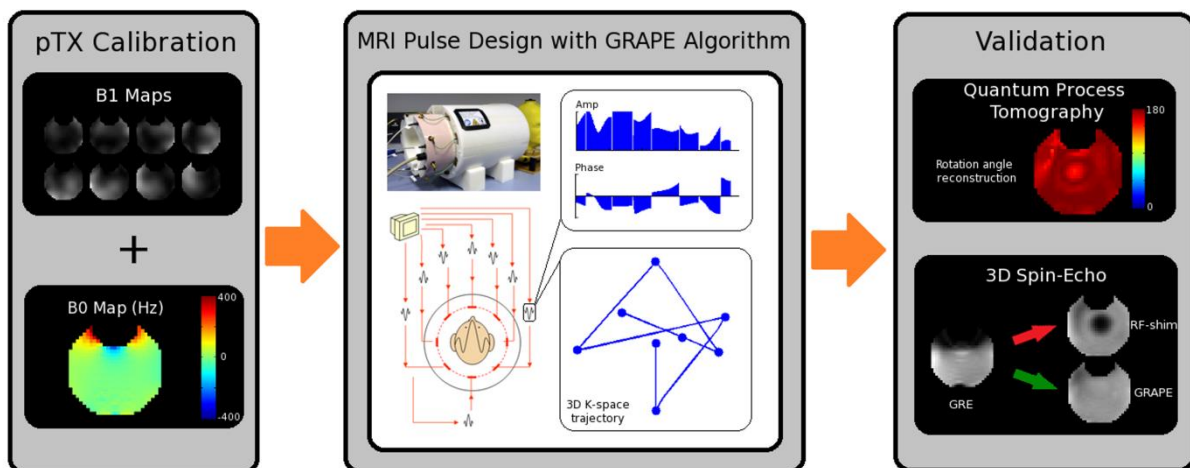
This Chapter has been accepted for publication as: Massire [A](#), Cloos MA, Vignaud [A](#), Le Bihan [D](#), Amadon [A](#), Boulant N. Design of non-selective refocusing pulses with phase-free rotation axis by gradient ascent pulse engineering algorithm in parallel transmission at 7 T. Journal of Magnetic Resonance 230, 76-83 (2013).

The methods & principles contained in this chapter were also published as an abstract in the proceedings of the Annual Meeting of the International Society for Magnetic Resonance in Medicine 2013.

The graphical abstract of this publication has been chosen to be the cover of the Journal of Magnetic Resonance, Issue No 230, 2013.

## Abstract

At ultra-high magnetic field ( $>7$  T),  $B_1$  and  $\Delta B_0$  non-uniformities cause undesired inhomogeneities in image signal and contrast. Tailored radiofrequency pulses exploiting parallel transmission have been shown to mitigate these phenomena. However, the design of large flip angle excitations, a prerequisite for many clinical applications, remains challenging due to the non-linearity of the Bloch equation. In this work, we explore the potential of gradient ascent pulse engineering to design non-selective spin-echo refocusing pulses that simultaneously mitigate severe  $B_1$  and  $\Delta B_0$  non-uniformities. The originality of the method lays in the optimization of the rotation matrices themselves as opposed to magnetization states. Consequently, the commonly used linear class of large tip angle approximation can be eliminated from the optimization procedure. This approach, combined with optimal control, provides additional degrees of freedom by relaxing the phase constraint on the rotation axis, and allows the derivative of the performance criterion to be found analytically. The method was experimentally validated on an 8-channel transmit array at 7 T, using a water phantom with  $B_1$  and  $\Delta B_0$  inhomogeneities similar to those encountered in the human brain. For the first time in MRI, the rotation matrix itself on every voxel was measured by using Quantum Process Tomography. The results are complemented with a series of spin-echo measurements comparing the proposed method against commonly used alternatives. Both experiments confirm very good performance, while simultaneously maintaining a low energy deposition and pulse duration compared to well-known adiabatic solutions.





## 6.1. Introduction

One of the main purposes of Ultra High Field (UHF) MRI is to improve spatial resolution, thanks to an increased signal to noise ratio. On the other hand, the applicability of most MRI sequences is challenged due to enhanced non-uniformities in the transmit-sensitivity ([Van de Moortele et al., 2005](#)). If not addressed, these can yield zones of shade and significant losses of contrast across the images, detrimental to diagnostics. Simple hard or sinc pulses are highly susceptible to RF field inhomogeneities, while adiabatic pulses ([Garwood and Ke, 1991](#); [Silver et al., 1984](#)) are generally considered too SAR intensive for practical use at 7 T and above ([Cloos et al., 2012a](#); [Moore et al., 2012](#)). On top of that, as the static magnetic field increases, MR scans become more prone to off-resonance effects resulting in susceptibility artifacts, with similar imaging consequences.

Over the last few years, a lot of research has been devoted to solve the above-mentioned problems, leading to an assortment of new powerful tools including shaped pulses, RF shimming ([Adriany et al., 2005](#)), Spokes ([Saekho et al., 2006](#)) and Parallel transmission (pTx) ([Katscher et al., 2003](#); [Zhu, 2004](#); [Grissom et al., 2006](#)). The latter, using tailored k-space trajectory designs, has been shown to produce highly uniform magnetization at UHF while maintaining a good slice selection profile and relatively short excitation duration ([Setsompop et al., 2008c](#)).

In this framework, whole-brain non-selective uniform excitations were recently demonstrated at 7 T with the  $k_T$ -point method ([Cloos et al., 2012a](#)). This technique proposes a minimalistic transmit k-space trajectory concentrated around the center of k-space to compensate for the smooth RF inhomogeneities present in large volumes such as the human brain, thus enabling energy efficient, sub-millisecond pulses yielding normalized root mean square errors (NRMSE) down to 6%. This method was then extended to large tip angles ([Cloos et al., 2012b](#)) using optimal control theory ([Xu et al., 2008](#)). When applied to  $T_1$ -weighted imaging (e.g. with the MP-RAGE sequence ([Mugler and Brookeman, 1990](#))) such pulses were shown to provide excellent spatial uniformity throughout the human brain, outperforming adiabatic pulses played in conventional Circularly-Polarized mode (CP) and subject-specific RF-shim, while simultaneously reducing the cumulative energy deposition ([Cloos et al., 2012b](#)).

On the other hand, to the best of our knowledge the non-selective refocusing pulses included in the 3D spin-echo (SE), turbo spin-echo (TSE) and gradient spin-echo (GRASE) sequences, all relevant for  $T_2$ -weighted imaging at UHF have not been addressed. Most work carried out so far has exclusively been in 2D and has relied on a state description of the dynamics and on the, not always fulfilled, linear class of large tip angle (LCLTA) criteria

(Pauly et al., 1989b) to presume consistent behavior for arbitrary states (Setsompop et al., 2008b; Xu et al., 2007).

In this manuscript, we evaluate the potential of the GRAdient Ascent Pulse Engineering algorithm (GRAPE) (Khaneja et al., 2005; Borneman et al., 2010) combined with the successfully demonstrated  $k_T$ -point method to design non-selective refocusing pulses. Using a dedicated phantom that produces strong  $B_1$  and  $\Delta B_0$  non-uniformities at 7 Tesla, the fidelity of these new refocusing pulses is assessed by incorporation into a 3D spin-echo sequence. For comparison, the performances of RF shim and BIR-4 adiabatic pulses are also evaluated. Finally, the rotation induced by the proposed pulse design is characterized via several magnetization measurements.

## 6.2. Theory

Due to its flexibility for systematically imposing desirable constraints and richness in efficient algorithms, the optimal control method has produced many interesting results regarding pulse design (Conolly et al., 1986; Xu et al., 2008). In the framework of refocusing pulses, formulating the problem by specifying a target propagator (i.e. a rotation matrix) is appealing as the initial magnetization state is not likely known accurately or it can simply be arbitrary. If the linear class of large tip angle approximation is omitted, a state description requires a predefined phase of the transverse RF field to determine the desired output state. Consequently, an unnecessary constraint is imposed, missing the fact that the dephased magnetization due to  $\Delta B_0$  gradients can be refocused regardless of that phase.

To alleviate the above-mentioned restrictions, we adapt the GRAPE algorithm (Khaneja et al., 2005; Borneman et al., 2010) to tailor excitations that approach the target propagator corresponding to a  $180^\circ$  rotation about a free transverse rotation axis. The procedure maximizes a wisely chosen performance criterion using optimal control theory, so that its derivatives with respect to the control parameters can be calculated analytically and that the phase of the rotation axis is left free. Although random initial guesses could possibly lead to good results, the starting point of the GRAPE algorithm here is a solution of the linearized Bloch equation, i.e. the so-called Small Tip Angle (STA) regime, rescaled to the refocusing rotation angle  $FA = 180^\circ$  (cf. the so-called “high tip angle approximation” (Boulant and Hoult, 2012)). For non-selective pulse design, the excitation  $k$ -space trajectory uses the  $k_T$ -point approach as in (Cloos et al., 2012b), where inversion pulses were targeted rather than refocusing pulses.

### 6.2.1. Spin-domain Bloch equation

To save computation time and memory requirements, the SU(2) group formalism is used. If relaxation effects are neglected, the Bloch dynamics of the magnetization is simply expressed by a 2 x 2 unitary matrix, the so-called spin-domain representation. In this domain, a rotation by an angle  $\Phi$  about a vector  $\mathbf{n}$  ( $n_x, n_y, n_z$ ) can be described by the complex-valued Cayley-Klein parameters ( $\alpha, \beta$ ) (Pauly et al., 1991):

$$U = \begin{bmatrix} \alpha & -\beta^* \\ \beta & \alpha^* \end{bmatrix}, \text{ with } |\alpha|^2 + |\beta|^2 = 1. \quad (6.1)$$

For a given RF pulse  $B_1(r, t)$  and gradient waveform  $\mathbf{G}(t)$ , a static field offset of  $\Delta B_0$ , the  $\alpha$  and  $\beta$  representing the rotation they induce at a spatial location  $\mathbf{r}$  is obtained by solving the spin-domain Bloch equation (Pauly et al., 1989b):

$$\begin{bmatrix} \dot{\alpha} \\ \dot{\beta} \end{bmatrix} = \frac{i\gamma}{2} \begin{bmatrix} \mathbf{G} \cdot \mathbf{r} + \Delta B_0 & B_1^* \\ B_1 & -(\mathbf{G} \cdot \mathbf{r} + \Delta B_0) \end{bmatrix} \begin{bmatrix} \alpha \\ \beta \end{bmatrix}. \quad (6.2)$$

When an array of  $m$  transmit coils is used, the total effective  $B_1$  field is a function of both space and time.  $S^R$  and  $S^I$  are the real and imaginary parts of the transmit sensitivities, while  $u_k$  and  $v_k$  are the control parameters, which represent real and imaginary parts of the RF shape of the  $k^{\text{th}}$  transmitter:

$$B_1(r, t) = \sum_{k=1}^m [S_k^R(r) + iS_k^I(r)][u_k(t) + iv_k(t)]. \quad (6.3)$$

Alternatively, the Bloch equation can also be recast as:

$$\dot{U} = -i \left( H_0 + \sum_{k=1}^m H_{uk} u_k(t) + \sum_{k=1}^m H_{vk} v_k(t) \right) U, \quad (6.4)$$

which is simply Schrodinger's equation. Here,  $H_0$  is the Hamiltonian corresponding to the  $\Delta B_0$  and gradient fields, both inducing rotations about the  $z$  axis, while  $H_{uk}/H_{vk}$  are the radiofrequency Hamiltonians corresponding to the available control parameters (i.e. real and imaginary parts of each RF waveform):

$$H_0 = -\frac{\gamma}{2}(\Delta B_0 + \mathbf{G} \cdot \mathbf{r})\sigma_z \quad H_{uk} = -\frac{\gamma}{2}(S_k^R \sigma_X + S_k^I \sigma_Y) \quad H_{vk} = \frac{\gamma}{2}(S_k^I \sigma_X - S_k^R \sigma_Y), \quad (6.5)$$

where  $\sigma_x$ ,  $\sigma_y$  and  $\sigma_z$  are the Pauli matrices, which together with the Identity matrix constitute a basis in  $SU(2)$ .

### 6.2.2. Performance criterion

The desired target and candidate propagators shall be denoted by  $U_F$  and  $U(T)$  respectively ( $T$  being the duration of our candidate pulse). A possible metric to measure their distance is:

$$\|U_F - U(T)\|^2 = \|U_F\|^2 + \|U(T)\|^2 - 2\text{Re}\langle U_F | U(T) \rangle. \quad (6.6)$$

Using the unitary property of these matrices, minimizing this distance corresponds to maximizing:

$$\text{Re}\langle U_F | U(T) \rangle = \text{Re} \left( \text{Tr} \left[ \frac{U_F^\dagger U(T)}{2} \right] \right), \quad (6.7)$$

where  $U_F^\dagger$  denotes the Hermitian conjugate of  $U_F$  and  $\text{Tr}$  is the trace operation. If a  $\pi$  rotation about the x axis is targeted ( $U_F = -i\sigma_x$ ), a candidate rotation  $U(T)$  parameterized by  $(\alpha, \beta)$  yields:  $\langle U_F | U(T) \rangle = \text{Im}(\beta)$  while if instead a  $\pi$  rotation about the y axis is targeted ( $U_F = -i\sigma_y$ ), we obtain:  $\langle U_F | U(T) \rangle = -\text{Re}(\beta)$ . As a result, by defining the target operator  $U_F = \sigma_x + i\sigma_y = \begin{bmatrix} 0 & 2 \\ 0 & 0 \end{bmatrix}$ , and taking the squared absolute value of the projection of  $U(T)$  onto  $U_F$ , we obtain our desired performance criterion:

$$\varphi = \frac{1}{N} \sum_{n=1}^N \varphi_n = \frac{1}{N} \sum_{n=1}^N |\langle U_F | U_n(T) \rangle|^2 = \frac{1}{N} \sum_{n=1}^N |\beta_n|^2, \quad (6.8)$$

where the summation is performed over all voxels ( $N$ ). That way,  $\varphi$  is equal to one, its maximum value, if and only if the rotation angle is  $180^\circ$  and the rotation axis is purely transverse everywhere. Note that  $U_F$  does not correspond to a physical rotation matrix, as it is not unitary. It is simply a convenient mathematical trick that removes the phase constraint on the transverse rotation axis. After discretizing the duration  $T$  in  $N_T$  time steps so that the final propagator  $U(T)$  is the product of  $N_T$  elementary  $U_j$  unitary matrices, we now need to take the derivatives of the resulting performance function with respect to all control parameters to compute its gradient. It reads ([Khaneja et al., 2005](#)):

$$\frac{\delta\varphi_n}{\delta u_k(j)} = -2\text{Re}\{\langle P_j | i\Delta t H_{uk} X_j \rangle \langle X_j | P_j \rangle\}, \quad (6.9)$$

where the products of rotation matrices for each time step  $j$  of the pulse are defined as:

$$X_j = U_j \dots U_1 \quad P_j = U_{j+1}^\dagger \dots U_N^\dagger U_F. \quad (6.10)$$

Using the conjugate gradient method, the new control parameters at the  $h^{\text{th}}$  iteration are:

$$u_k^{h+1}(j) = u_k^h(j) + \varepsilon \left( \frac{\delta\varphi}{\delta u_k^h(j)} + \beta_{\text{PR}} \frac{\delta\varphi}{\delta u_k^{h-1}(j)} \right). \quad (6.11)$$

The Polak and Ribiere coefficient  $\beta_{\text{PR}}$  ([Press et al., 2007](#)) was chosen, as we found that it returned here superior converge properties compared to the one of Fletcher-Reeves. Each iteration step size,  $\varepsilon$ , was determined via a line search algorithm.

### 6.2.3. GRAPE algorithm

The algorithm starts with the choice of the initial controls, which could be completely random. However, an educated guess generally leads to faster convergence. For this reason, we took the solution returned by the  $k_T$ -points method with a large flip angle approximation to start the iterative optimal control algorithm.

GRAPE algorithm steps:

- 1) Design initial pulse candidate.
- 2) Perform Bloch simulation, compute  $\varphi$  and store all the  $X_j$ .
- 3) Compute the gradient of  $\varphi$  by calculating its derivatives with respect to all control parameters.
- 4) Compute  $\beta_{\text{PR}}$ .
- 5) Determine the optimal  $\varepsilon$ .
- 6) Update all the controls.
- 7) Go to step 2 with the new controls and stops when the performance index is sufficient or if the maximum number of iterations has been attained.

#### 6.2.4. Extension to tailoring gradient waveforms

In the theory presented so far, the gradient waveforms were supposed to be given and fixed, i.e. they consisted of blips and led to a  $k_T$ -points trajectory. Likewise, magnetic field gradients could be considered as control parameters and the derivative of the performance criterion is given by:

$$\frac{\delta\varphi_n}{\delta G_x(j)} = -2\text{Re}\{\langle P_j | i\Delta t H_{Gx} X_j \rangle \langle X_j | P_j \rangle\}. \quad (6.12)$$

where  $H_{Gx} = -\frac{\gamma}{2}x\sigma_z$  is the Hamiltonian term for the gradient waveform along the x axis, and so forth for the gradients along the y and z axis. As in (Yip et al., 2007) for magnetization states, hence joint design of RF pulses and k-space trajectory can elegantly be integrated into the GRAPE algorithm to target this time rotation matrices. On the other hand, given that this increases the computational load, and as we have found in practice that it was not as critical, we chose to perform only ten alternate updates of the gradient waveforms at the beginning of the algorithm, limited to time points corresponding to the gradient blips. In other words, the location of the  $k_T$ -points was changed.

### 6.3. Experiments

#### 6.3.1. Experimental setup

Experimental validation was performed on a 7 Tesla Magnetom scanner (Siemens, Erlangen, Germany), equipped with an 8-channel transmit array (1 kW peak power per channel) and an AC84 head gradient system (Siemens, Erlangen) allowing amplitudes up to of 50 mT/m and a slew rate of 330 mT/m/ms. For both RF transmission and reception, a home-made transceiver- array head coil was used (Figure 6.1.a) (Ferrand et al., 2010). The array consists of 8 stripline dipoles distributed every  $42.5^\circ$  on a cylindrical surface of 27.6-cm diameter, leaving a small open space in front of the subject's eyes. All dipoles were tuned ideally at 297.18 MHz corresponding to the proton Larmor frequency at 7 T and matched identically to a 50 Ohm line impedance. A Dotarem-doped (0.25 mM) salted (6 g/L) distilled water phantom (16 cm diameter,  $T_1 \sim 600$  ms,  $T_2 \sim 500$  ms), was used to generate  $B_1$  inhomogeneities. In addition, a ping-pong ball was inserted in the phantom to generate substantial  $B_0$  field inhomogeneities due to the difference in susceptibility between air and water (Figure 6.1.b). Second order shims were used prior to any imaging sequences.

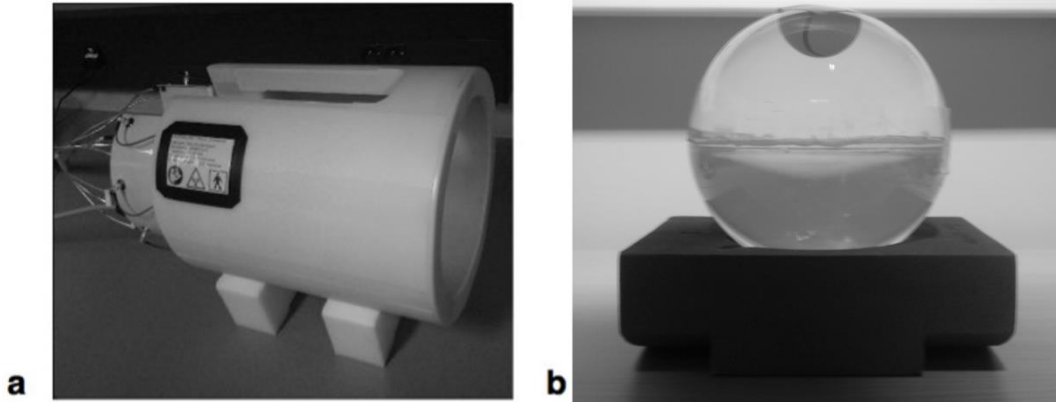


**Figure 6.1:** Experimental setup. **a:** Eight channels transmit-array coil used in this work. **b:** Spherical phantom with ping-pong ball.

### 6.3.2. $B_1$ and $B_0$ mapping

With an approximate CP-mode, the 3D spoiled steady-state actual flip-angle imaging (AFI) sequence (Yarnykh, 2007), including spoiling improvements (Nehrke, 2009), combined with the interferometry (Brunner and Pruessmann, 2008) and the  $\Delta B_0$  correction methods (Boulant et al., 2010), was used to map the  $B_1^+$  field. The amplitude maps were then smoothed using 3D polynomial fits. The sequence parameters were: TR1/TR2 20/100 ms, TE1/TE2 1ms, 5-mm isotropic resolution with a 48 x 48 x 36 matrix in transverse acquisition and eight simultaneous 250  $\mu$ s 180 V hard pulses. The maximum values of the  $\Delta B_0$  map reaching up to 800 Hz, and given our gradient capabilities, it was impossible to directly measure this map using a multi-echo sequence without inducing phase excursions larger than  $\pi$ . For this reason, the measurement of the  $\Delta B_0$  map was performed via three separate GRE acquisitions with different TEs (0.6, 1.1 and 1.6 ms). Finally, a mask was applied to all data, keeping only values of  $\Delta B_0$  approximately within the range of the values encountered in the human brain at 7 T (Cloos et al., 2012b). For the whole study, magnitude images from each channel were summed with the sum of squares method. Regarding the phase, the complex images were combined in such a way that the phases were aligned in the central voxel for a given reference first acquisition. The same linear combination was then kept throughout the study to remain consistent with this reference.

### 6.3.3. Pulse design

Our design started with initial guesses obtained from the  $k_T$ -points method targeting  $FA=90^\circ$  for the excitation pulse and an inversion pulse for the refocusing pulse, both to be used in the spin-echo sequence. Non-selective uniform excitation of the phantom was achieved by selecting a 7  $k_T$ -point trajectory surrounding the center of  $k$ -space. The peak amplitude of the designed waveforms was constrained to the maximum voltage available per channel (180 V). For the excitation, the magnitude least squares approach ([Setsompop et al., 2008a](#)), with an initial target transmit phase map obtained from the conventional CP mode, was employed. Subsequently, another optimal control approach (OCA) using magnetization state as opposed to rotation matrices was applied to optimize the  $90^\circ$  excitation pulse as described in ([Xu et al., 2008](#)). For the refocusing pulse, our GRAPE algorithm returned the result after 250 iterations, as described in the Theory section. The complete procedure was implemented in C++ including GPU-enabled CUDA extensions. Based on the performance of a 2.6-GHz Intel Xenon system paired with an NVIDIA Tesla C2050 GPU,  $180^\circ$  refocusing pulses, optimized with a 10  $\mu$ s sampling time, were typically found in about 5 minutes.

#### 6.3.4. Measurement of the rotation matrix induced by the refocusing pulse

A set of measurements was dedicated to evaluate the rotation generated by our refocusing pulse, using a procedure called Quantum Process Tomography ([Boulant et al., 2003](#); [Nielsen and Chuang, 2010](#)). The idea is to apply the refocusing pulse to different input magnetization states forming a set of linearly independent vectors, measure the corresponding output states, and retrieve the linear mapping via a mathematical recipe ([Havel, 2002](#)). Although in general the procedure can characterize non-unitary dynamics, here for simplicity and due to the fact that the RF pulse was short compared to  $T_1$  and  $T_2$ , we assumed the dynamics to be unitary, which reduced the number of necessary measurements.

First an AFI sequence was implemented to characterize, as accurately as possible, a given reference excitation pattern, in this case a pseudo CP-mode. Second, a GRE sequence with the same excitation pattern was implemented with  $TR = 2.4$  s. Because  $TR \gg T_1$ , the magnitude of the signal was simply  $\rho f(r) \exp(-TE/T_2^*) \sin(FA)$  where  $\rho$ ,  $f$  and  $FA$  are the spin density, reception sensitivity and flip angle respectively. Knowing the flip angle in every voxel thanks to the AFI sequence then allows to compute  $\rho f(r) \exp(-TE/T_2^*)$  and to normalize all subsequent data with it. Last, this allows to compute the magnetization state at the end of the pulse for each voxel:  $[M_x \ M_y \ M_z] = [\sin(FA)\cos(\phi) \ \sin(FA)\sin(\phi) \ \cos(FA)]$ , where  $\phi$  is the returned measured phase. This constitutes the first input state. Two other independent states were simply generated by shifting the phase of each RF transmitter, or equivalently  $\phi$ , by  $45^\circ$  and  $90^\circ$ , thereby yielding the second and third input states. Finally, the same pulses were



concatenated with our tailored 180° refocusing pulse and inserted into their respective GRE sequence. Likewise, the measured signal allowed to determine  $[M_x^{\text{out}} M_y^{\text{out}} M_z^{\text{out}}]$  in each case by using the output signal, phase and normalization condition, again assuming unitary dynamics. The procedure thus can be expressed with the following matrix equation:

$$\begin{bmatrix} M_x^{\text{Out},0} & M_x^{\text{Out},45} & M_x^{\text{Out},90} \\ M_y^{\text{Out},0} & M_y^{\text{Out},45} & M_y^{\text{Out},90} \\ M_z^{\text{Out},0} & M_z^{\text{Out},45} & M_z^{\text{Out},90} \end{bmatrix} = [\text{Rotation matrix}] \begin{bmatrix} M_x^{\text{In},0} & M_x^{\text{In},45} & M_x^{\text{In},90} \\ M_y^{\text{In},0} & M_y^{\text{In},45} & M_y^{\text{In},90} \\ M_z^{\text{In},0} & M_z^{\text{In},45} & M_z^{\text{In},90} \end{bmatrix}. \quad (6.13)$$

As long as the flip angle of the preparation pulse is neither zero nor 90°, the input matrix is invertible so that our first estimation of the rotation matrix simply is  $\text{Res} = [\text{Out}][\text{In}]^{-1}$ . Nevertheless, because of experimental errors, noise and not perfectly unitary dynamics, it is clear that  $\text{Res}$  is not strictly speaking a rotation matrix. Fitting procedures could be used to obtain the closest rotation matrix consistent with the data. However, a theorem by Fan and Hoffman ([Fan and Hoffman, 1955](#)) states that a (much faster) polar decomposition yields the closest unitary matrix  $\text{Rot}$  for any unitarily-invariant norm. This procedure returns:

$$\text{Rot} = \text{Res}(\sqrt{\text{Res}'\text{Res}})^{-1}. \quad (6.14)$$

Matrix inversions and polar decompositions were performed with MATLAB (The MathWorks, Natick, MA, USA). Cayley-Klein parameters and axis angle representation of the rotation were then extracted from the eigenvalues and eigenvectors of the rotation matrices.

### 6.3.5. Spin echo sequence

To evaluate the spatial uniformity and the refocusing performance, a 3D spin echo sequence was also modified to incorporate the proposed refocusing pulse design and several commonly employed alternatives. In all cases, crusher gradients surrounded the refocusing pulse. Repetition time and echo time were set to 800 ms and 25 ms respectively to generate significant intra-voxel dephasing artifacts in the absence of a refocusing pulse. Resolution was 5-mm isotropic, with a 48 x 48 x 32 matrix in transverse acquisition.

First the performance of the 90° excitation was qualitatively evaluated with a 3D GRE. Then 3D spin echo sequences including this excitation and either one of the following refocusing pulses were run for comparison. In all cases, the pulse voltage reached its maximum available (180 V) on at least one of the transmit channels:

- 1/ 630- $\mu$ s square pulses in pseudo CP-mode (FA=180° targeted in center of phantom).
- 2/ 1270- $\mu$ s square pulses in RF shim mode (the duration is doubled because FA=180° is targeted on average over the entire volume).
- 3/ our GRAPE-designed pulse.
- 4/ a 5-ms adiabatic BIR-4 ([Staewen et al., 1990](#)) with RF-shim phase configuration (~same duration as GRAPE pulse).
- 5/ a 10-ms adiabatic BIR-4 with phase RF-shim.

## 6.4. Results

### 6.4.1. Pulse design

Individual  $B_1^+$  maps obtained with our coil on the phantom at 7 T are shown in Figure 6.2.a. In pseudo CP-mode, the measured standard deviation divided by the mean value of  $B_1$  is around 25 %.

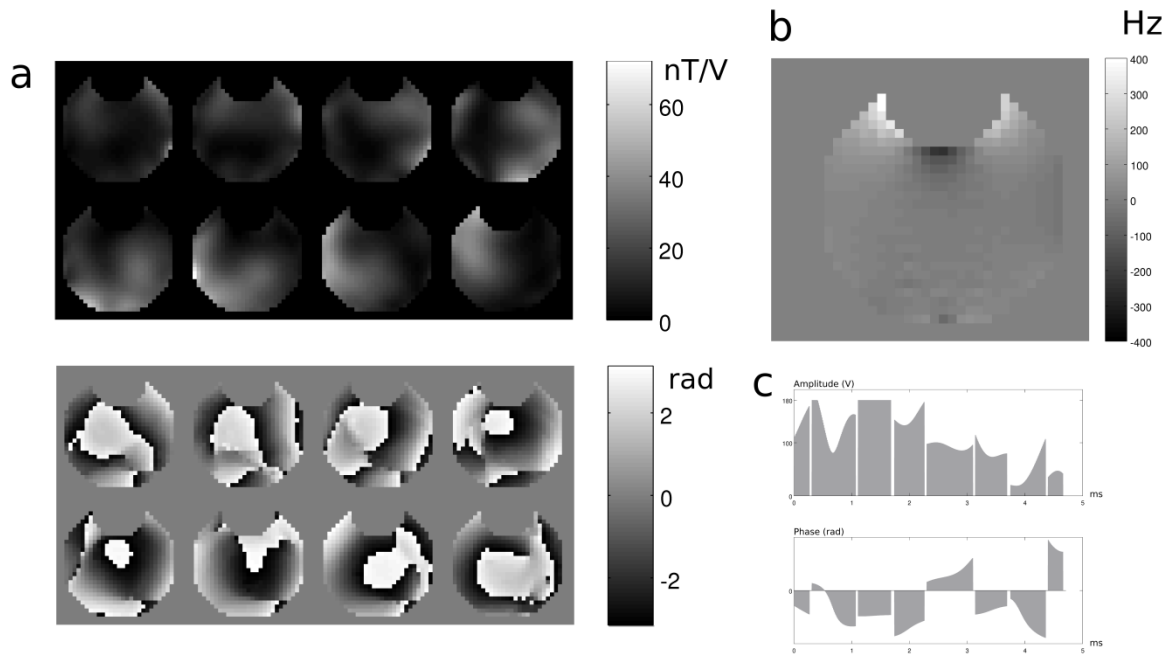


**Figure 6.2:** Radiofrequency and static field maps. **a:** Transmit sensitivity and relative phase maps measured for each of the eight transmit elements (central axial slices). **b:**  $\Delta B_0$  map measured in Hz, central sagittal slice. **c:** Example of tailored RF shape on one channel (amplitude and phase).

To stay consistent with human brain pulse design constraints, large values of  $\Delta B_0$  were cropped out of the ROI ( $B_0$  excursion was kept between -250 Hz and 500 Hz approximately).

One can see the dipolar pattern on the central sagittal slice in Figure 6.2.b due to the difference in susceptibilities between air and water. The excitation pulse tailored with OCA had a simulated 9.6 % NRMSE and therefore provided a fairly homogeneous spin excitation. Returned tailored pulses durations were 2470  $\mu\text{s}$  for the 90° excitation and 4650  $\mu\text{s}$  for the refocusing.

Pulse performances were calculated via numerical Bloch simulations in the spinor domain (relaxation was ignored). To assess refocusing quality, many metrics were computed: the Cost Function of GRAPE (CF):  $\sum_{i=1}^N(1 - |\beta_i|^2)/N$ , the Rotation Angle Normalized Root Mean

Square Error (RA NRMSE):  $\frac{1}{\pi} \sqrt{\sum_{i=1}^N(\pi - \theta_i)^2/N}$  ( $\theta_i$  being the rotation angle in the  $i$ th voxel),

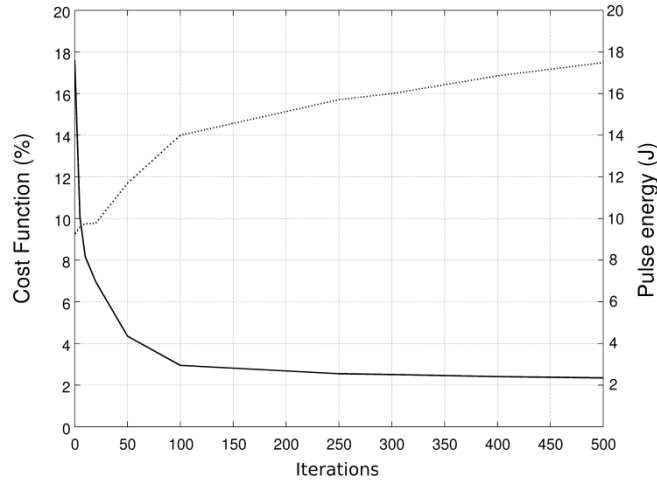
and the Axis Normalized Root Mean Square Error (A NRMSE):  $\sqrt{\sum_{i=1}^N(1 - (n_x^2 + n_y^2))/N}$ .

Table 6.1. summarizes all these metrics calculated for the proposed method and its alternatives. In addition to these metrics, the total energy of the pulses was computed.

Pulses	Duration ( $\mu\text{s}$ )	Cost Function (%)	RA NRMSE (%)	A NRMSE (%)	Energy (J)
<i>CP-mode</i>	630	52.6	53.0	15.0	3.3
<i>RF-shim</i>	1270	13.3	24.1	13.2	6.6
<i>STA</i>	4650	17.6	13.6	37.6	9.2
<i>GRAPE</i>	4650	2.55	8.1	10.2	15.7
<i>Short BIR-4</i>	5000	6.9	8.8	23.0	22.9
<i>Long BIR-4</i>	10000	3.4	3.0	17.9	46.7

**Table 6.1:** Pulse design metrics. Simulation results.

Both pseudo CP-mode and RF-shim hard pulses performed relatively poorly, as expected. The initial  $k_T$ -points solution based on the STA approximation results in a better RA NRMSE, but globally worse cost function, and with elongated pulse duration and roughly 50% increased energy. After GRAPE optimization, simulations show a sharp improvement of all metrics, with a reasonable amount of energy. A BIR-4 adiabatic pulse of equivalent duration, with a higher energetic cost, is not able to produce the refocusing quality of our tailored pulse. A 10-ms BIR-4 pulse however is producing rather comparable performance, but takes twice as long and requires about three times the energy. In Figure 6.3 is shown the evolution of the cost function (%) and the cumulative energy deposition (J), targeting a 180° transverse rotation with the GRAPE algorithm, as a function of the number of iterations. Clearly, the energy of the GRAPE pulse could have been a bit lower, with only a mild cost in performance.



**Figure 6.3:** Cost function and pulse energy versus the number of iterations. Evolution of the cost function in % (solid line) and the cumulative energy deposition in Joules (dashed line) targeting a 180 degrees rotation angle with the GRAPE algorithm, function of the number of iterations.

#### 6.4.2. Measurement of the rotation matrix induced by the refocusing pulse

Figure 6.4.a provides axial slices for both measured and simulated angles of rotation, obtained with Quantum Process Tomography and Bloch simulations respectively. Good correspondence is found between them, as the experimentally obtained RA NRMSE for the whole phantom is 7.14 % (8.07 % simulated). The cost function ( $1-|\beta|^2$ ) is shown as well on Figure 6.4.b, experimental value being 3.44 % (2.55 % simulated). In-plane rotation angle profiles along several segments are also provided.

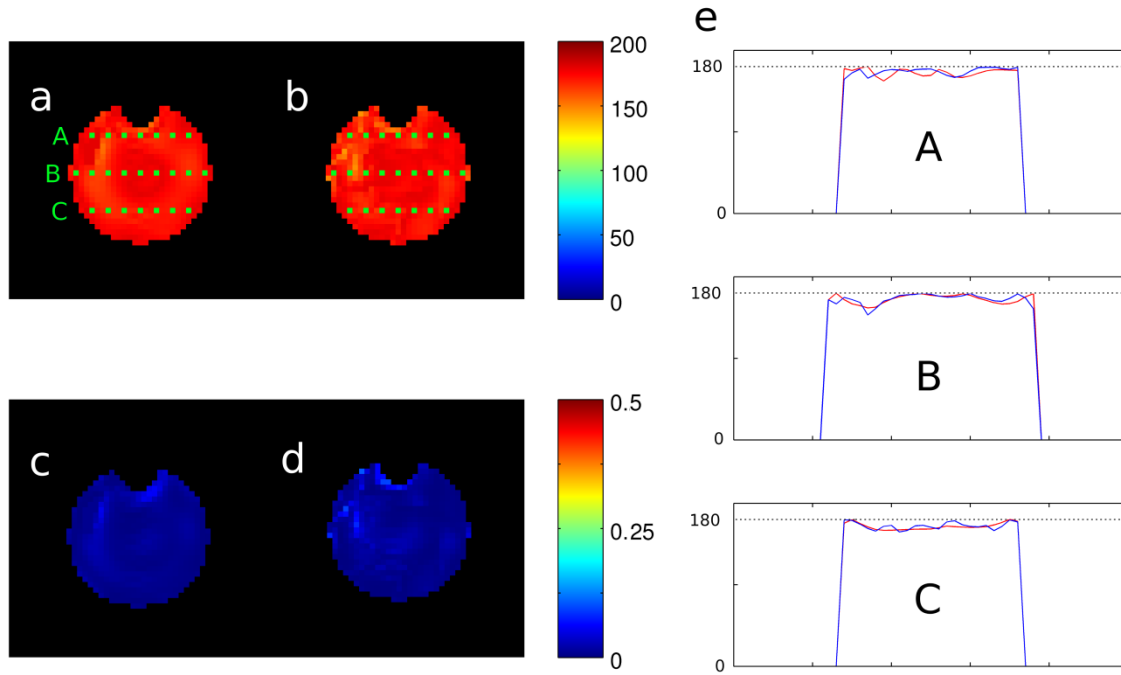


**Figure 6.4:** Quantum process tomography results (axial central slices). **a:** Measured rotation angle in degrees. **b:** Corresponding simulated rotation angle in degrees. **c:** Measured cost function ( $1-|\beta|^2$ ). **d:** Corresponding simulated cost function. **e:** 1-D in-plane rotation angle profiles along the segments marked in a. (red: measured, blue: simulated).

### 6.4.3. Spin echo measurement

In Figure 6.5 are provided images of the central slices of the phantom, after data post-processing was applied to remove the reception profile contribution. First, one can clearly see that when only tailored  $90^\circ$  excitation is played, the signal is lost in areas with strong  $\Delta B_0$  gradients, i.e. close to the ping-pong ball. Pseudo CP-mode refocusing hard pulses yield a poor quality image, where the signal is significantly reduced in most regions, except in the middle where the  $180^\circ$  rotation was calibrated. Likewise, spin-echo hard pulses with RF-shim resulted in similar signal attenuations albeit occurring at different locations. The modified spin-echo with both tailored excitation and refocusing pulses however brings back most of the dephased signal and yields good uniformity. The images produced adopting a 5-ms BIR-4 refocusing pulse still contain signal inhomogeneities and the dephased signal around the ping-pong ball is not completely retrieved. The 10-ms BIR-4 pulse yields rather good homogeneity and signal recovery, as predicted by our simulations, but requires three times more energy (Table 6.1). In all cases, the RF refocusing pulses being sandwiched by crusher gradients, the  $\Delta B_0$  evolution was to some extent refocused, but with a signal intensity in

principle varying as  $\sin^2(\theta/2)$  (Sodickson and Cory, 1998), where  $\theta$  is the rotation angle of the refocusing pulse (assuming purely transverse rotation axis). In all figures, some signal inhomogeneities remain due to an imperfect knowledge of the reception profile, whose estimation suffered from a low signal to noise ratio in some regions.

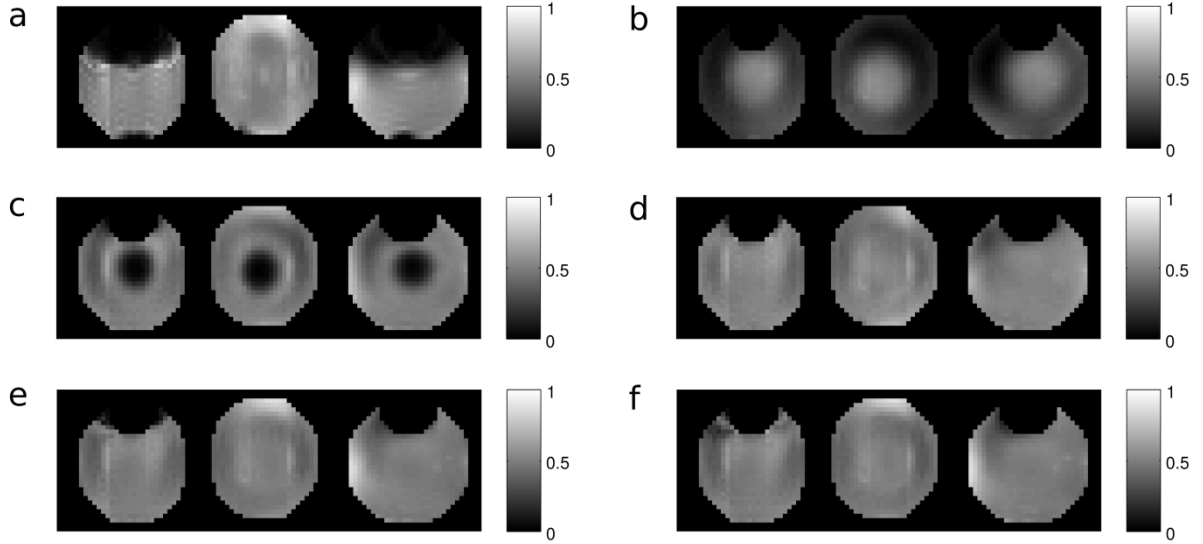


**Figure 6.5:** Spin-echo results. **a:** Excitation only (OCA). **b:** Spin-Echo with hard pulses in pseudo CP-mode **c:** Spin-Echo with hard pulses in RF-shim configuration. **d:** GRAPE Spin-Echo. **e:** Spin-Echo with short adiabatic pulse. **f:** Spin-Echo with long adiabatic pulse. From left to right in each subfigure are shown sagittal, coronal and axial central slices.

## 6.5. Discussion

### 6.5.1. The GRAPE algorithm

In this study, we have investigated a new algorithm dedicated to the design of non-selective refocusing pulses with a phase-free transverse rotation axis. This method, named gradient ascent pulse engineering can simultaneously mitigate severe  $B_1$  and  $\Delta B_0$  inhomogeneities comparable to what may be expected for human brain at 7 T. The power of this method lays in the optimization of the rotation matrices themselves and in the relaxation of the phase constraint on the rotation axis, which gives more freedom in pulse design. In addition, the analytical computation of the derivatives with respect to the control parameters speeds up the algorithm compared to other numerical methods. To this end, and further validate the

results predicted by the simulations, several MRI experiments were performed on a 7 T scanner with an 8-channel transmit array, including an innovative application of Quantum Process Tomography to MRI.

The optimal control GRAPE algorithm presents several advantages compared to conventionally used finite difference methods, as it requires fewer computations. Indeed, finite difference methods require adding a small perturbation to the total magnetic field for every control parameter. Once the perturbation is added, the elementary matrix rotation induced is constructed, and then concatenated with the other unaffected elementary rotation matrices. The resulting overall net matrix rotation finally gives the new performance index and thus the gradient, allowing the control parameters to be updated. The GRAPE algorithm spares the pulse designer all these elementary calculations due to the analytical result (Equation 6.9). This enables a significantly faster computation which can efficiently be evaluated on GPUs allowing the final result to be obtained in less than 5 minutes. If this time is considered unsatisfactory, Figure 6.3 indicates that almost equivalent performance could have been obtained in 100-150 iterations, thereby halving this computation time. Finally, and in agreement with (Setsompop et al., 2008b), we have found that it was possible to undersample by at least a factor of 2 the number of voxels without affecting substantially the performance criterion. As a result, such pulses can be realistically designed in less than 2 minutes with the above-described computing capabilities.

It has been found in practice that the choice of the initial candidate pulse greatly influences the final result of the optimization. The full optimization of these degrees of freedom, the  $k_T$ -point locations and order, remains the topic of further study. The continuous  $k$ -space trajectory optimization could as well be addressed using the GRAPE algorithm but we fear that the increased dimensions of the parameter space may result in worse local minima. Last, in the approach that we report here, we have found the conjugate gradient technique to yield significantly better results than the steepest descent method.

### **6.5.2. Phase-free refocusing pulses are strictly equivalent to inversion pulses**

One can find a few instances in the literature where pulse designs relying on a state description of the dynamics (by looking at the initial magnetization along  $z$ ) to perform inversion pulses were boldly attempted for refocusing purposes. For instance in (Grissom et al., 2008), the pulses yielded good refocusing performance while leaving some residual phase inhomogeneity in the region of interest, despite the fact that only a few, but not all, LCLTA criteria were presumably fulfilled. As we will now demonstrate, this behavior can also be understood using the spinor formalism.

The Mz magnetization state in SU(2) corresponds to the  $[1\ 0]'$  vector. Propagating this vector by an arbitrary unitary matrix parameterized by  $\alpha$  and  $\beta$  yields:

$$\begin{pmatrix} \alpha \\ \beta \end{pmatrix} = \begin{pmatrix} \alpha & -\beta^* \\ \beta & \alpha^* \end{pmatrix} \begin{pmatrix} 1 \\ 0 \end{pmatrix} \quad (6.15)$$

Finally, projecting this result along the  $-M_z$  state, i.e. the  $[0\ 1]'$  vector, and taking the absolute value square returns:

$$\left| \begin{pmatrix} 0 & 1 \end{pmatrix} \begin{pmatrix} \alpha & -\beta^* \\ \beta & \alpha^* \end{pmatrix} \begin{pmatrix} 1 \\ 0 \end{pmatrix} \right|^2 = |\beta|^2 \quad (6.16)$$

which is just our performance index. The two recipes, from the mathematical point of view, thus are strictly equivalent. This could possibly explain the results in (Grissom et al., 2008), including the remaining phase dispersion in the region of interest. The similarity however stops here, i.e. with  $180^\circ$  rotations. As we have tried to convey in the theory section, the performance metrics can involve a different angle of rotation as well as a target phase for the axis of rotation (Khaneja et al., 2005). Many applications thus requiring the implementation of true arbitrary rotations could benefit from the GRAPE approach. Finally, it saves a factor of two in computation time compared to other optimal control approaches where the spin dynamics is calculated for two orthogonal states (Deng et al., 2011).

### 6.5.3. Quantum Process Tomography

We have applied for the first time Quantum Process Tomography to MRI in order to characterize the rotation matrix in every voxel. The obtained results confirmed the successful implementation of a  $180^\circ$  rotation with a phase-free transverse axis of rotation. Simplifications could be done due to the fact that the duration of the pulse was short compared to  $T_1$  and  $T_2$ . Had it not been the case, seven more measurements would have been needed to fully characterize the process and the analysis would have been more elaborate (Weinstein et al., 2004). But for many applications where the pulses are reasonably short compared to the relaxation times, quantum process tomography is a fairly straightforward procedure to implement and can thus be used to characterize the axes and angles of the rotation matrices. It may become a standard to verify the correct implementation of desired rotation matrices for the pulse designer.



#### **6.5.4. Spin-echo results**

Our spin echo results demonstrate a sharp improvement of the GRAPE pulses over hard pulse configurations (RF-shim, pseudo-CP mode). Compared to adiabatic pulses, the main advantage of GRAPE is the small pulse duration and energy required to obtain the same level of performance, although energy penalties were not enforced here. According to our simulations (Table 6.1), even a BIR-4 pulse twice longer than our GRAPE pulse and requiring about 3 times more energy did not perform nearly as good.

### **6.6. Conclusion**

A joint pulse design algorithm for producing non-selective phase-free refocusing pulses able to mitigate severe  $B_1$  and  $\Delta B_0$  inhomogeneities has been investigated in the context of parallel transmission MRI at 7 T. The gradient ascent pulse engineering algorithm uses optimal control to tailor the propagator corresponding to the RF pulse shape and gradient blips to achieve a phase-free  $180^\circ$  transverse rotation of the spins, regardless of the initial state of the magnetization. The approach was experimentally validated by using Quantum Process Tomography and standard spin-echo sequences. Future work involves the inclusion of specific absorption rate constraints in order to make this technique more viable for in-vivo studies.

## **7. Parallel-transmission-enabled 3D T<sub>2</sub>-weighted imaging of the human brain at 7 Tesla**

This Chapter has been accepted for publication as: Massire [A](#), Vignaud [A](#), Robert B, Le Bihan [D](#), Boulant N, Amadon [A](#). Parallel-transmission-enabled 3D T<sub>2</sub>-weighted imaging of the human brain at 7 Tesla. Magnetic Resonance in Medicine doi: 10.1002/mrm.25353 (2014).

The methods & principles contained in this chapter were also published as an abstract in the proceedings of the Annual Meeting of the International Society for Magnetic Resonance in Medicine 2014.

## Abstract

**Purpose:** A promise of Ultra High Field MRI is to produce images of the human brain with higher spatial resolution due to an increased signal to noise ratio. Yet, the shorter radiofrequency wavelength induces an inhomogeneous distribution of the transmit magnetic field and thus challenges the applicability of MRI sequences which rely on the spin excitation homogeneity. In this work, the ability of parallel-transmission to obtain high-quality  $T_2$ -weighted images of the human brain at 7 Tesla, using an original pulse design method is evaluated.

**Methods:** Excitation and refocusing square pulses of a SPACE sequence were replaced with short non-selective transmit-SENSE pulses individually tailored with the gradient ascent pulse engineering algorithm, adopting a  $k_T$ -point trajectory to simultaneously mitigate  $B_1^+$  and  $\Delta B_0$  non-uniformities.

**Results:** In vivo experiments showed that exploiting parallel-transmission at 7T with the proposed methodology produces high quality  $T_2$ -weighted whole brain images with uniform signal and contrast. Subsequent white and gray matter segmentation confirmed the expected improvements in image quality.

**Conclusion:** This work demonstrates that the adopted formalism based on optimal control, combined with the  $k_T$ -point method, successfully enables 3D  $T_2$ -weighted brain imaging at 7T devoid of artifacts resulting from  $B_1^+$  inhomogeneity.

## 7.1. Introduction

T<sub>2</sub>-weighted imaging is a fundamental MRI technique employed for the diagnosis of brain diseases or injuries involving gray matter and white matter lesions such as strokes, ischemia and multiple sclerosis (van der Kolk et al., 2011; de Graaf et al., 2012). T<sub>2</sub>-weighted imaging is commonly achieved thanks to the spin-echo phenomenon, which consists in reversing the dephasing of the transverse magnetization to create a signal echo. RARE imaging (Hennig et al., 1986) (also known as Turbo Spin Echo or Fast Spin Echo) increases the speed of spin-echo imaging by acquiring a series of spin echoes with different phase encodings after each excitation. Later developments on RARE focused on reducing and continuously varying the flip angle of the refocusing pulses as a useful means of addressing high radiofrequency (RF) power deposition and typical RARE image artifacts such as blurring (Hennig and Scheffler, 2001; Hennig et al., 2003, 2004; Busse et al., 2006). The variable flip angle turbo spin echo sequence, referred to as “SPACE” (Sampling Perfection with Application optimized Contrasts using different flip angle Evolution) (Mugler, 2000), is now among the most commonly employed 3D sequences to obtain T<sub>2</sub>-weighted anatomical images of the brain. To this end, an excitation pulse is followed by a long variable angle refocusing pulse train acquiring an entire k-space partition plane per repetition (TR). Careful adjustment of the targeted angles and the echo spacing between the acquisition blocks, as well as the usual imaging parameters, allows excellent contrast between gray matter (GM), white matter (WM) and Cerebrospinal fluid (CSF) at field strengths up to 3 Tesla (Busse et al., 2006). Alternative imaging contrasts are created with preparation (typically inversion) pulses prior to excitation, as in the fluid attenuation inversion recovery (FLAIR) imaging (Visser et al., 2010; de Graaf et al., 2012), one of the most efficient techniques for highlighting contrast between GM and WM, and the double inversion recovery (DIR) imaging (Madelin et al., 2010; de Graaf et al., 2012), widely used for GM visualization.

T<sub>2</sub>-weighted imaging should benefit from the increased signal-to-noise ratio available at high field strengths (7 Tesla and beyond) to enable higher spatial resolution acquisitions and hence better visualization of small structures and fluid interfaces of the brain. However, when moving towards Ultra High Fields (UHF), the increased resonance frequency of proton nuclei (297 MHz at 7 Tesla) causes the RF wavelength to become smaller than the human brain, leading to an inhomogeneous distribution of the transmit magnetic field ( $B_1^+$ ). This spatial  $B_1^+$  inhomogeneity gives rise not only to variations in signal intensity for a given tissue across the brain, but more importantly, to different levels of contrast in the same image (Madelin et al., 2010; Visser et al., 2010). Parallel transmission (pTX) (Katscher et al., 2003; Zhu, 2004; Grissom et al., 2006) has been repeatedly shown to successfully mitigate these issues. This

technique utilizes multiple independently-driven coil elements distributed around the subject. In its simplest form, referred to as RF-Shimming (Van de Moortele et al., 2005), the  $B_1^+$  fields from all coil elements are combined optimizing the amplitude and phase of each array element, while keeping the waveforms identical, to optimize the  $B_1^+$  distribution in a region of interest (ROI). RF-shimming has already demonstrated its ability to mitigate the  $B_1^+$  field inhomogeneity at 3 T in the context of  $T_2$ -weighted imaging with a TSE sequence (Malik et al., 2012). Further generalization of this concept led to the introduction of Transmit-SENSE, exploiting the full potential of the transmit-array by tailoring the RF waveforms to apply to each of the individual coil-elements. This transmission generally occurs in concert with magnetic field gradients to provide additional degrees of freedom in order to maximize the final excitation uniformity.

In that framework, whole-brain non-selective uniform spin excitations were demonstrated at 7 Tesla using a  $k_T$ -point trajectory (Cloos et al., 2012a). This technique proposes a minimalistic transmit k-space trajectory concentrated around the center of k-space to compensate for the smooth RF inhomogeneities present in volumes such as the human brain. This method was then extended to large tip angles (Boulant and Hoult, 2012; Hoyos-Idrobo et al., 2013). Using optimal control theory (Xu et al., 2008) and when applied to MP-RAGE  $T_1$ -weighted imaging, such pulses were shown to provide excellent spatial uniformity throughout the human brain (Cloos et al., 2012b). More recently, further optimized non-selective phase-free refocusing  $k_T$ -points pulses able to mitigate severe  $B_1^+$  and  $\Delta B_0$  inhomogeneities have been investigated to achieve a target transverse rotation of the spins, regardless of the initial state of the magnetization at 7 Tesla with pTX (Massire et al., 2013), thanks to the GRAdient Ascent Pulse Engineering algorithm (GRAPE) (Khaneja et al., 2005). In the meantime, self-refocused  $k_T$ -points pulses were placed in a SPACE sequence and provided  $T_2$ -weighted images of improved quality in terms of signal and contrast homogeneity (Eggenschwiler et al., 2013). However in that study, only one RF pulse was designed and subsequently scaled for the whole RF echo train, an approximation that worsens with the angle value. A purely transverse rotation axis was also assumed by imposing self-refocused pulses (Pauly et al., 1989b), likewise an approximation that deteriorates at high flip angle values and when there are off-resonance effects.

The objective of this work thus is to extend the GRAPE algorithm formalism, combined with the successfully demonstrated  $k_T$ -point method, to design all the individual non-selective excitation, inversion and refocusing pulses that are used in 3D  $T_2$ -weighted brain imaging. In order to significantly improve the signal homogeneity observed at 7 Tesla, no approximations on the refocusing process are made and off-resonance effects are considered throughout in the pulse design. Such tailored pulses were included in a home-made variable flip angle turbo spin echo sequence (SPACE) to replace the conventionally used hard pulses. This

sequence seeks to drive the signal evolution of the flip angle train for a specified couple of  $T_1$  and  $T_2$  relaxation times, achieving a pseudo-steady state ([Mugler, 2000](#)). It can be supplemented by preparation pulses to achieve alternative contrasts (FLAIR & DIR). Experimental results obtained at 7 T with both conventional (pseudo-Circularly Polarized mode and RF-shim configuration) and hereby proposed pTX methods are compared in terms of image quality. Subsequent white and gray matter segmentation emphasizes the expected improvements.

## 7.2. Theory

In a previous study ([Massire et al., 2013](#)), a new algorithm dedicated to the design of non-selective refocusing pulses with a phase-free transverse rotation axis was investigated. This method, named GRAPE, can simultaneously mitigate severe  $B_1^+$  and  $\Delta B_0$  inhomogeneities typically observed in the human brain at 7 Tesla. The power of this method lays in the optimization of the rotation matrices themselves, which is very appealing in the framework of refocusing pulses encountered in the SPACE sequence, as the initial magnetization state before each refocusing pulse can be arbitrary. Still, in the SPACE sequence, all refocusing pulses must share the same phase pattern to fulfill the assumed Carr-Purcell-Meiboom-Gill (CPMG) condition ([Mugler, 2000](#); [Hennig and Scheffler, 2001](#); [Hennig et al., 1986, 2003, 2004](#); [Busse et al., 2006](#)). Last, the analytical computation of the derivatives with respect to the control parameters provided by the algorithm spares the pulse designer many time-consuming elementary calculations necessary to other numerical methods. In this section, various adaptations of the GRAPE algorithm are described in order to tailor every single RF pulse of a SPACE-like sequence to obtain sustainable refocusing of magnetization.

### 7.2.1. GRAPE aiming at any given refocusing angle with a phase-free transverse rotation axis

The running of the gradient ascent pulse engineering algorithm for the design of a  $180^\circ$  refocusing pulse is already described in details in ([Massire et al., 2013](#)). This formalism is extended here to tailor excitations that approach the target propagator corresponding to any rotation angle about a free transverse rotation axis, through a new performance index to maximize using optimal control, and a new target operator to aim at. The phase constraint on the rotation axis of this reference pulse is relaxed, which gives more freedom to improve its performance, as the dephased magnetization due to  $\Delta B_0$  offsets is refocused regardless of

that phase. Once this improved reference pulse is found, it dictates the phase pattern for all the other pulses in order to fulfill the CPMG condition.

To save computation time and memory requirements, the spin-domain representation is used to express Bloch dynamics of the magnetization for the  $n^{\text{th}}$  voxel when an RF pulse of duration  $T$  is applied, as a  $2 \times 2$  unitary rotation matrix with complex-valued Cayley-Klein parameters  $(\alpha, \beta)$  (Pauly et al., 1991):

$$U_n(T) = \begin{bmatrix} \alpha & -\beta^* \\ \beta & \alpha^* \end{bmatrix}, \text{ with } \begin{cases} \alpha = \cos \frac{\Phi}{2} - i n_z \sin \frac{\Phi}{2} \\ \beta = -i(n_x + i n_y) \sin \frac{\Phi}{2} \end{cases} \text{ and } |\alpha|^2 + |\beta|^2 = 1, \quad (7.1)$$

with an angle  $\Phi$  about a rotation axis vector  $\mathbf{n}$  ( $n_x, n_y, n_z$ ). In the case of refocusing, the target is a rotation matrix of a given angle, with a purely transverse axis, whose in-plane direction is left free. Once a proper target is established, a metric to optimize its distance with the candidate pulse needs to be found. Mathematically, minimizing the  $L_2$  norm of these two unitary matrices difference is strictly equivalent to maximizing their inner product, which directly quantifies the overlap between the two. If  $\theta$  is the desired rotation angle, building upon our previous work (Massire et al., 2013), two “virtual” target rotation matrices decomposing the desired operation can be used:

$$U_{F1} = \begin{bmatrix} \cos \frac{\theta}{2} & 0 \\ 0 & \cos \frac{\theta}{2} \end{bmatrix} \text{ and } U_{F2} = \begin{bmatrix} 0 & 2 \sin \frac{\theta}{2} \\ 0 & 0 \end{bmatrix}. \quad (7.2)$$

To tailor the RF pulse rotation matrix in the  $n^{\text{th}}$  voxel, a possible performance criterion  $\varphi_n$  is:

$$\varphi_n = \varphi_{1,n} + \varphi_{2,n} = \left| \langle U_{F1} | U_n(T) \rangle / 2 \right| + \left| \langle U_{F2} | U_n(T) \rangle / 2 \right|. \quad (7.3)$$

Indeed, rewriting this expression knowing that  $\langle U_{F1} | U_n(T) \rangle = \text{Tr}(U_{F1}^\dagger U_n(T))$  gives:

$$\varphi_n = \left| \cos \frac{\theta}{2} \cos \frac{\Phi}{2} \right| + \sqrt{n_x^2 + n_y^2} \left| \sin \frac{\theta}{2} \sin \frac{\Phi}{2} \right|. \quad (7.4)$$

Evaluation of  $\varphi_n$  shows that this criterion is equal to one, its maximum value, if and only if:

$$\begin{cases} \Phi = \theta \\ \sqrt{n_x^2 + n_y^2} = 1 \end{cases} \text{ or } \begin{cases} \Phi = 2k\pi \pm \theta \\ \sqrt{n_x^2 + n_y^2} = 1 \end{cases}, \text{ where } k \text{ is an integer.} \quad (7.5)$$

In practice, the second case is not encountered, as the required energy would be considerably higher for the same pulse duration. After summing this performance criterion for all voxels ( $\varphi = \frac{1}{N} \sum_{n=1}^N \varphi_n$ ), a cost function equal to  $1-\varphi$  is minimal, if and only if the rotation angle is  $\theta$  and the rotation axis is purely transverse everywhere in the ROI. Note that  $U_{F1}$  and  $U_{F2}$  do not correspond to physical rotation matrices, as they are not unitary. It is simply a mathematical convenience that removes the phase constraint on the transverse rotation axis. After time discretization, the derivatives of this performance function with respect to all control parameters  $u_k$  (which are the real and imaginary parts of the RF pulse on each coil channel) are taken to compute its gradient, knowing that for each voxel:

$$\frac{\partial \varphi_{1,2}}{\partial u_k} = \frac{1}{2} \frac{1}{\varphi_{1,2}} \frac{\partial \varphi_{1,2}^2}{\partial u_k}. \quad (7.6)$$

In this way, the original analytical formulation of the derivative proper to the GRAPE algorithm could be retrieved, acknowledging the fact that this function is not strictly speaking differentiable at  $\varphi_{1,2} = 0$  (see references ([Khaneja et al., 2005](#); [Massire et al., 2013](#)) for the whole expression of the derivative with  $2 \times 2$  rotations matrices). Control parameters are then updated using the conjugate gradient method. As in ([Massire et al., 2013](#)), gradient blips intensities are also considered as additional degrees of freedom and optimized with the RF throughout this work in order to modulate the k-space trajectory.

### 7.2.2. GRAPE aiming at any given refocusing angle with a specific phase pattern target

In the case of the SPACE sequence, the formalism described above is used to tailor a reference refocusing pulse of the RF echo train. This pulse then dictates a phase pattern for the whole sequence. For all subsequent refocusing pulses, as well as the initial excitation pulse, care has to be taken as the CPMG condition fulfillment is mandatory to obtain the desired refocusing of magnetization. Indeed, as several types of echoes (primary echo, stimulated echo, etc.) arise from multiple refocusing pathways, it is crucial that simultaneously acquired echoes are kept phase-coherent. Following the original GRAPE algorithm ([Khaneja et al., 2005](#)), we can target a specific phase pattern, precisely the one of



the reference refocusing pulse, and change only the rotation angle. Hence, the target rotation matrix is:

$$U_F = \begin{bmatrix} \alpha_T & -\beta_T^* \\ \beta_T & \alpha_T^* \end{bmatrix}, \text{ with: } \begin{cases} \alpha_T = \cos \frac{\theta}{2} \\ \beta_T = -i(n_{xT} + in_{yT})\sin \frac{\theta}{2} \end{cases}, \quad (7.7)$$

where  $\theta$  is the new desired target rotation angle,  $n_{xT}$  and  $n_{yT}$  the normalized components of the first refocusing pulse axis of rotation (voxel-dependent). The performance criterion is then:

$$\varphi = \frac{1}{N} \sum_{n=1}^N \varphi_n = \frac{1}{N} \sum_{n=1}^N |\langle U_F | U_n(T) \rangle|^2. \quad (7.8)$$

The optimization procedure and the updating of the control parameters then is the same as in (Massire et al., 2013), the only difference being smaller latitude in the optimization, as the target operator is more specific. Last, thanks to the smooth variation of the angle values along the RF train, a previously designed pulse can be used as an initial guess for the next one, thus greatly speeding up the algorithm convergence.

A flowchart of the whole procedure in order to tailor every single RF pulse of a SPACE-like sequence is provided in Figure 7.1.

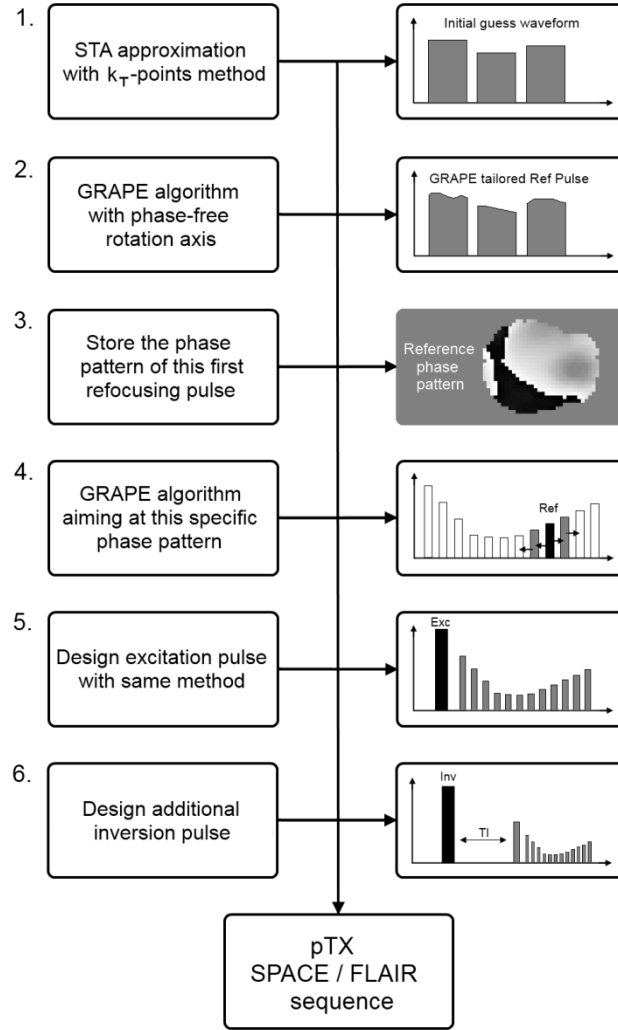


**Figure 7.1:** Flowchart for SPACE/FLAIR pulse design. Step 1: The initial guess waveform is the solution returned by the small tip angle approximation, using the  $k_T$ -points method [16,17]. Step 2: The reference refocusing pulse is designed with a phase-free rotation axis. Its phase pattern is stored and used as a target for the design of all subsequent refocusing pulses (steps 3-4). Step 5: The excitation pulse design is similar, targeting  $90^\circ$  and the same phase pattern dephased by  $+\pi/2$  to fulfill CPMG condition. Step 6: The GRAPE algorithm described in (Massire et al., 2013) can be used to design an additional inversion pulse if needed (e.g. for FLAIR).

## 7.3. Methods

### 7.3.1. Experimental setup

Experimental validation was performed on a 7 Tesla Magnetom scanner (Siemens, Erlangen, Germany), equipped with parallel transmission capabilities and an AC84 head gradient system allowing amplitudes up to of 50 mT/m and a slew rate of 333 T/m/s, on four different healthy volunteers. Our study was approved by our institutional review board and informed consent was obtained from all volunteers. For both RF transmission and reception, a home-made transceiver-array head coil was used ([Ferrand et al., 2010](#)). The array consists of 8 stripline dipoles distributed every  $42.5^\circ$  on a cylindrical surface of 27.6-cm diameter, leaving a small open space in front of the subject's eyes. All dipoles were tuned ideally at 297.18 MHz corresponding to the proton Larmor frequency at 7 Tesla and matched identically to a 50 Ohm line impedance. Second-order  $B_0$  shims were used prior to any imaging sequence.

### 7.3.2. Online fast pTX calibration and pulse design

Transmit sensitivity profiles of every coil element were acquired with the 2D multi-slice magnetization-prepared turbo-FLASH  $B_1^+$  mapping XFL sequence (resolution: 5 mm isotropic, total acquisition time: 4 min) ([Amadon et al., 2012](#); [Fautz et al., 2008](#)). Magnetization preparation was achieved using a very selective VERSE'd saturation pulse, producing a spatially-dependent flip angle (FA) to be measured. In addition, the interferometric method with a  $180^\circ$ -phase-offset on each channel to obtain individual transmit sensitivity profiles was used ([Brunner and Pruessmann, 2009](#)).

To complete the pulse design input, a fast 2D 3-echoes spoiled Gradient Echo (GRE) sequence, was employed to map the  $\Delta B_0$  field (TA ~ 20s). This was followed by a 2.5 mm isotropic higher resolution 2D GRE acquisition to define, with the aid of the brain extraction tool from the FSL software package ([Smith, 2002](#)), the three-dimensional ROI corresponding to the brain on which pulse design should be made (TA ~ 1 min). The complete pulse design procedure was implemented in C++ including GPU-enabled Compute Unified Device Architecture (CUDA<sup>TM</sup>, Nvidia Corporation, Santa Clara, CA, USA). Based on the performance of two Intel Xenon E5-2670 CPUs paired with two NVIDIA Tesla Kepler K20 GPUs, the entire pulse train design was typically achieved in less than 3 minutes.

To focus on the improvement provided by our tailored pulses in terms of contrast and signal homogeneity, the contribution of the highly non-uniform reception profile  $B_1^-$  of our transceiver coil was removed in all in-vivo images ([Mauconduit et al., 2014](#)). The reception profile was obtained with a GRE sequence with very low flip angle ( $1^\circ$ ) and relatively short TR (150 ms), after dividing the image by the computed CP transmit profile (known from the  $B_1^+$  mapping procedure). A 3D polynomial filter (8<sup>th</sup> order) was subsequently applied to the resulting map to abrogate remaining contrast of tissues due to proton density.

### 7.3.3. Sequence design and validation

The variable flip angle series of the SPACE sequence that yields prescribed signal evolution was calculated as in (Mugler, 2000) and subsequent studies, using the Spatially Resolved Extended Phase Graph (SR-EPG) for specified  $T_1 = 1400$  ms and  $T_2 = 40$  ms relaxation times (min. angle:  $10^\circ$ , max angle:  $100^\circ$ ). Conventional square pulse durations were set to 600  $\mu$ s and 900  $\mu$ s for the CP-mode and RF-shimming respectively. An initial candidate waveform fed to the GRAPE algorithm consisted of solving the Magnitude Least Squares problem (Setsompop et al., 2008a) with a 3  $k_T$ -point self-refocused trajectory (i.e.  $k(0)=0$ ) surrounding the center of  $k$ -space. The location of the  $k_T$ -points was determined empirically off-line for an initial case study (Cloos et al., 2012a) and was kept the same for all the subjects, keeping in mind that these locations were then free to move thanks to the GRAPE algorithm. The reference refocusing pulse design was achieved after about 100 iterations of the first adaptation of the GRAPE algorithm presented in the theory section. For the other pulses, a quasi-linear scaling of their duration with respect to the prescribed angle was followed by 2 to 10 iterations of the GRAPE algorithm presented in the second part of the theory section. With this setup, about 50 different pulses needed to be designed, since several similar pulses are used in the echo train. The peak amplitudes of the designed waveforms were constrained to the maximum voltage available per channel (180 V). Replacing the original hard pulses of the SPACE sequence with sets of sub-pulses and gradients blips inevitably increases their durations and Specific Absorption Rate (SAR) contributions. This inherently affects the TR of the sequence, the echo spacing ES and the shape of the RF echo train. The following sequence protocols were implemented:

**SPACE:** TR: 6 s, ES: 9 ms, effective TE: 315 ms, Echo Train Length: 96 pulses, resolution: 1 mm isotropic, matrix size: 256x224x160, GRAPPA factor: 2, Partial Fourier: 6/8, TA: 12 min.

**FLAIR:** same as SPACE, except TR: 9 s, TI: 2.5 s, TA: 18 min.

As an aside, the same GRAPE recipe was used for a 0.8 mm isotropic version of the SPACE sequence with similar acceleration factors, bringing the echo train length to 117 pulses and the acquisition time to 14 minutes. The sequence is expected to hold well in terms of Contrast to Noise Ratio (CNR) and SAR, at the expense of a decrease in Signal to Noise Ratio (SNR). Last, to ensure that GRAPE-tailored pulses led to the expected signal evolution during the refocusing echo train, a “4-dimension” SPACE sequence was run on a spherical

phantom (16 cm diameter, filled with agarose gel and  $\text{CuSO}_4$ -doped salted distilled water,  $T_1$ :  $1100 \pm 50$  ms,  $T_2$ :  $50 \pm 2$  ms). In this longer sequence, all echoes of the refocusing train encode the same phase-encoded line during a repetition time. In that way, if there are  $N$  echoes,  $N$  images of the phantom are generated, each with its own signal intensity. As a result, this sequence provides a spatially-dependent signal evolution monitoring during the echo train.

#### 7.3.4. SAR evaluation

In this study, SAR was never directly taken into account in the pulse design procedure for simplicity. On the other hand, compliance with the SAR guidelines (IEC, 2010) was checked by monitoring the TR-averaged RF power levels for each transmit-channel. Similarly to some endeavors dedicated to provide accurate SAR predictions (Graesslin et al., 2012), our SAR assessment tool (Cloos et al., 2010b) evaluates both the global and local 10-gram SAR over four pre-simulated data sets (different anatomies, different positions) in a conservative manner (Boulant et al., 2011). From these models, the software then returns the worst case SAR scenario and ensures that 10-g and whole-head average SAR values respect the IEC guidelines (10 W/kg and 3.2 W/kg respectively). On average, our conservative approach (Boulant et al., 2011) typically overestimates the true absorbed energy by a factor 5. In all cases, the 10-g local SAR found approached its limit more closely than the global one.

### 7.4. Results

#### 7.4.1. pTX calibration and pulse design

Individual  $B_1^+$  maps obtained with our coil on the first subject are shown in Figure 7.2.a. For the four subjects scanned in CP-mode, the measured standard deviation divided by the mean value of  $B_1^+$  was around  $26.5 \pm 2.3\%$  in the ROI. Measurements of  $\Delta B_0$  inhomogeneities (Figure 7.2.b.) showed a mean standard deviation of around 40 Hz, with peak values up to about 250 Hz. The durations of the tailored pulses varied approximately from 300  $\mu\text{s}$  to 2 ms.

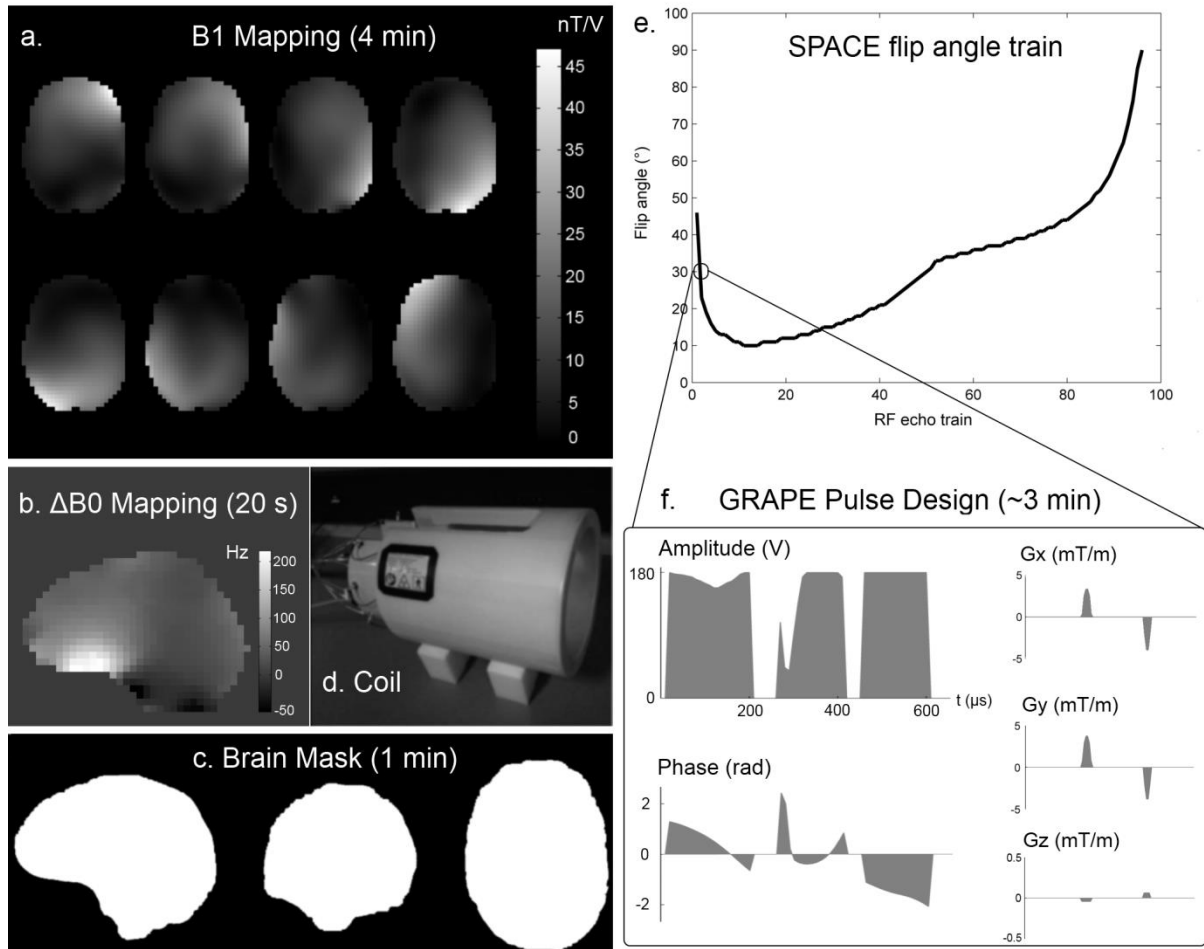


**Figure 7.2:** Online fast pTX calibration and pulse design. **a.** Measured transmit sensitivity magnitudes of the eight transmit elements (central axial slices). **b.**  $\Delta B_0$  map measured in Hz, central sagittal slice. **c.** Brain mask extracted with FSL (central slices). **d.** Eight-channel transceiver-array coil used in this work. **e.** Flip angle train designed for the SPACE sequence used in this study. **f.** Example of a tailored RF pulse on one of the Tx-channels (amplitude, phase and gradient blips).

Based on the four volunteers' data, Bloch simulations were performed to evaluate the theoretical performance of the first refocusing pulse designed (example on one channel on Figure 7.2.f.), whose performance is similar to any subsequent refocusing pulse. The cost function defined in the Methods section directly quantifies how good the rotation of the prescribed angle along a purely transverse axis is. On average, the GRAPE optimization achieved a  $37 \pm 2\%$  relative improvement of this cost function, starting from RF pulses designed with the STA approximation, with 100 iterations in about 30 seconds. Even though the cost function employed here is useful because it is concise and its derivatives are analytical (Massire et al., 2013), it remains that the numbers returned are more abstract

compared to more standard pulse designers' metrics. For this reason we also defined two metrics: **a.** the dispersion of the angle value itself, called here Rotation Angle Normalized

Root Mean Square Error (RA NRMSE):  $\frac{1}{\theta} \sqrt{\sum_{i=1}^N (\theta - \Phi_i)^2 / N}$  ( $\theta$  being the prescribed rotation

angle,  $\Phi_i$  the effective rotation angle in the  $i$ th voxel and  $N$  the total number of voxels), and **b.**

the deviation of the rotation axis from the transverse plane, called here Axis NRMSE:

$\sqrt{\sum_{i=1}^N (1 - \sqrt{n_x^2 + n_y^2})^2 / N}$ . On average, the GRAPE optimization reaches a RA NRMSE of

$12.1 \pm 0.4\%$  and an A NRMSE of  $5.5 \pm 0.3\%$  across subjects. These values are 3 to 4 times better than the ones obtained from hard pulses played in CP-mode ( $40.6 \pm 0.5\%$  and  $17.6 \pm 0.6\%$ ) or in a 3D-optimized RF-shim mode ( $34.6 \pm 1.1\%$  and  $20.2 \pm 0.4\%$ ), both configurations being inherently strongly affected by the  $\Delta B_0$  distribution. Experimental validation of individual RF pulse could be performed using Quantum Process Tomography applied to MRI, just like in ([Massire et al., 2013](#)).

#### 7.4.2. Sequence validation

Figure 7.3 displays a comparison of the signal evolution throughout the RF echo train between hard pulses played in CP-mode and GRAPE-tailored  $k_T$ -points pulses, for the spherical phantom. Regions of interest for signal assessment were selected in the central 10-mm-thick sagittal slice, one in the center and the three others in random locations between the center and the borders. Whereas the CP-mode enables very good behavior of the signal in the center of the phantom (black line) compared to the expected one predicted by the SR-EPG framework (a light grey area is used to illustrate the standard deviation of measured phantom  $T_1$  and  $T_2$ ), signal persistence is altered in other regions (grey lines). GRAPE pulses on the other hand were able to reproduce to a good extent the same pattern for the whole phantom, confirming the expected signal behavior as well as a better signal homogeneity in the whole pulse design ROI.

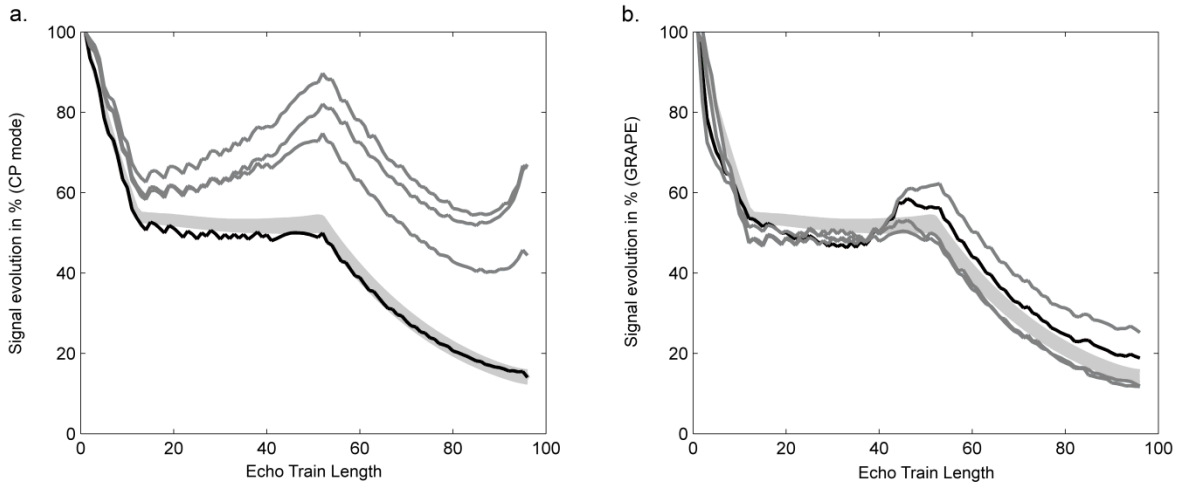


**Figure 7.3:** Measured signal behavior along the RF echo train in the central sagittal slice, in percent of the first signal echo intensity (light grey area: theory; black line: ROI in the center of the phantom; grey lines: ROI in other regions). **a.** Hard pulses played in a pseudo-Circularly Polarized mode. **b.** Proposed methodology with the GRAPE algorithm.

#### 7.4.3. SPACE & FLAIR $T_2$ -weighted images

SPACE images for three configurations (CP-mode, RF-shim configuration and GRAPE design) are displayed on Figure 7.4, for one of the subjects. The conventional CP-mode method implemented at 7 Tesla resulted in strong signal voids in the cerebellum and in temporal lobes. Application of a subject-specific RF-shim improved image quality to some extent, thus allowing cerebellar GM/WM to be distinguished. Even so, residual  $B_1^+$  non-uniformities introduced significant signal variations in other regions of the brain, complicating distinction between GM and WM in these regions with confidence. Using GRAPE-tailored  $k_T$ -points improved every refocusing profile and led to higher signal homogeneity for a given tissue across the brain. Considerable improvements occurred in the cerebellum, in the upper brain region and in the temporal lobes. In addition, intricate structures of the cortex can now be resolved in greater detail. This is particularly true in the 0.8 mm isotropic SPACE images provided in Figure 7.5, where 117 RF pulses are used to encode one partition of the k-space.



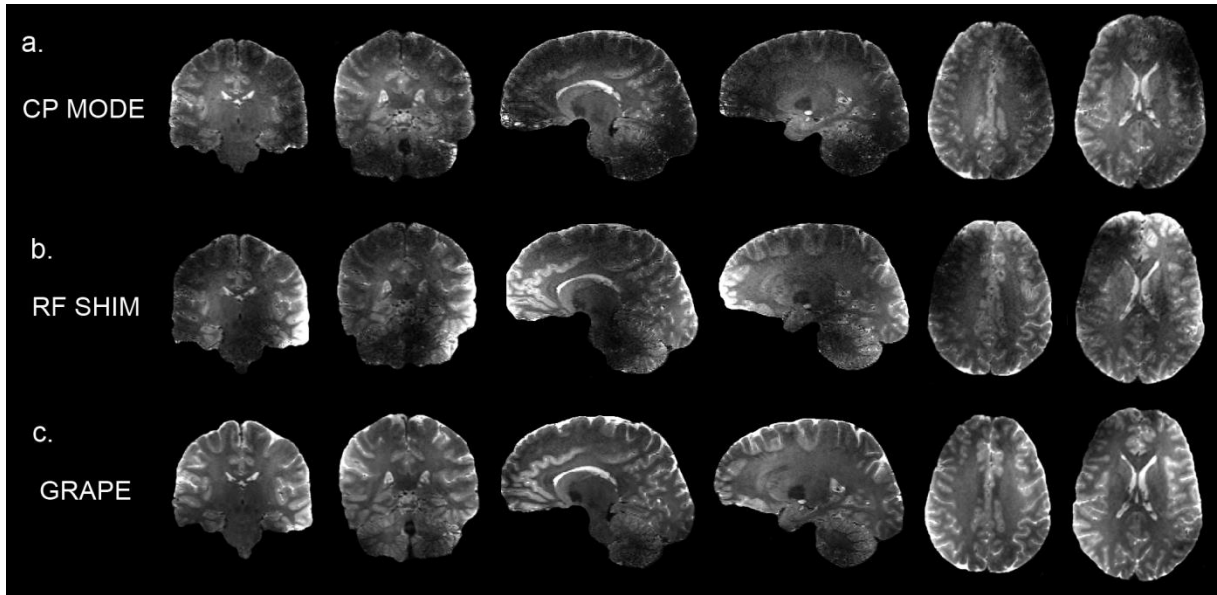


**Figure 7.4:**  $T_2$ -weighted SPACE images of Subject #2 at 1mm isotropic resolution (all images are corrected for coil reception profile). From top to bottom: **a.** Conventional hard pulses played in a pseudo-Circularly Polarized mode. **b.** Hard pulses played in a static RF-shim configuration. **c.** Proposed methodology with GRAPE-tailored pulses for excitation and refocusing.

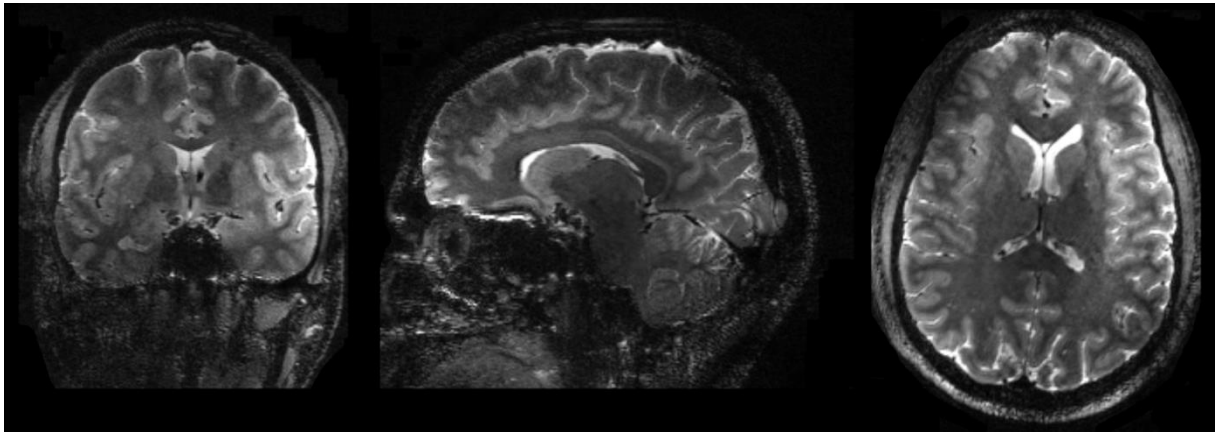


**Figure 7.5:**  $T_2$ -weighted SPACE images (coronal, sagittal and axial slices, from left to right) of Subject #3 with 0.8mm isotropic resolution and GRAPE-tailored RF pulses (all images are corrected for coil reception profile).

To perform the FLAIR inversion necessary to nullify the CSF signal, a 5180  $\mu\text{s}$  duration  $180^\circ$  GRAPE pulse was designed (Number of  $k_T$ -points: 8, RA NRMSE: 6.55%, A NRMSE: 1.53%, pulse energy: 7.8 J) and placed before the SPACE sequence block. FLAIR images are provided in Figure 7.6. The CSF signal is clearly suppressed everywhere in the ventricles

and around the brain and the cerebellum, confirming the quality of the inversion on the whole ROI. Last, as opposed to what is commonly seen in clinical studies at 7 Tesla ([Visser et al., 2010](#); [de Graaf et al., 2012](#)), here the cerebellum and the temporal lobes visibility is increased thanks to the proposed design. In addition, the energy of the GRAPE inversion pulse is smaller than the one of an adiabatic pulse traditionally used for inversion purposes and therefore compatible with UHF exams ([Massire et al., 2013](#)).

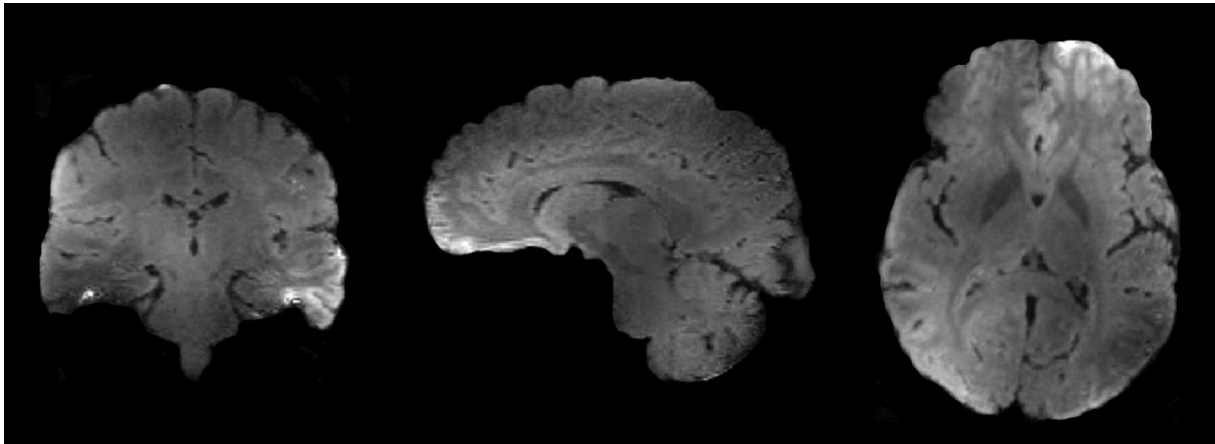


**Figure 7.6:**  $T_2$ -weighted FLAIR images (coronal, sagittal and axial slices, from left to right) of Subject #4 with 1mm isotropic resolution and GRAPE-tailored RF pulses (all images are corrected for coil reception profile).

#### 7.4.4. $T_2$ -weighted images automated segmentation

MRI is a sensitive modality for visualizing multiple sclerosis lesions. For the diagnosis of this disease,  $T_2$ -weighted image analysis could outperform  $T_1$ -weighted image analysis in term of accuracy ([de Graaf et al., 2012](#)). Yet, automated tissue segmentation from  $T_2$ -weighted images is a prerequisite for large-scale estimation of lesion volumes. In this work, we adapt the brain tissue segmentation pipeline of the BrainVisa ([BrainVISA/Anatomist, 2014](#)) software, to extract a voxel classification from our improved  $T_2$ -weighted images. As shown in Figure 7.7, these images could be accurately segmented, even in the temporal lobes, where signal is commonly lacking with conventional methods at such high field strength.

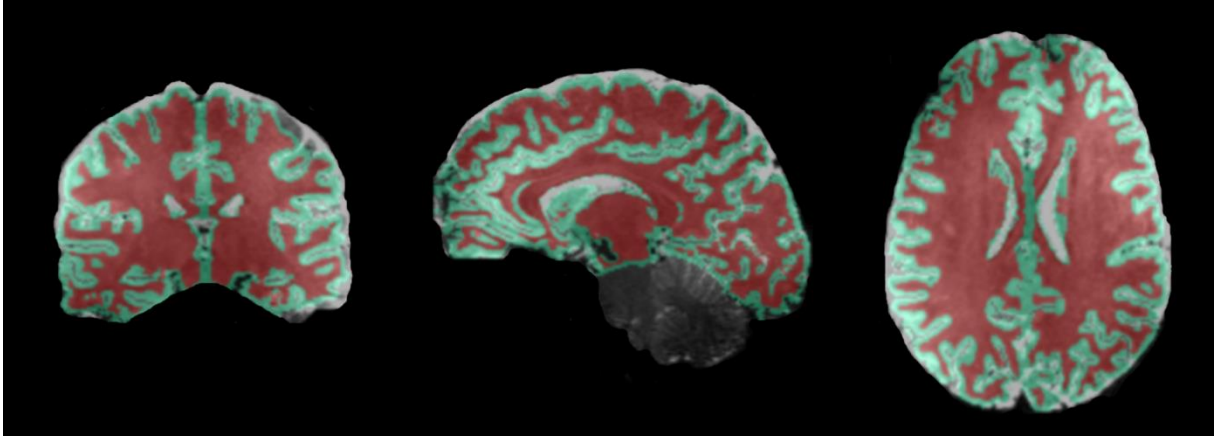


**Figure 7.7:** Results of automated brain tissue segmentation on 1 mm isotropic resolution SPACE images of Subject #2. Voxels identified as GM are superimposed in green, whereas voxels identified as WM are superimposed in red. Image post-processing includes contrast inversion, edges detection and bias correction.

## 7.5. Discussion

We have investigated in this study how the GRAPE algorithm can simultaneously mitigate severe  $B_1^+$  and  $\Delta B_0$  inhomogeneities to produce high quality  $T_2$ -weighted images of the human brain. Given that this optimal control process proposed is directly applied to rotation operators, refocusing pulses perform well regardless of the initial magnetization state and enforce proper magnetization evolution during the refocusing echo train. We proposed a novel approach to use the GRAPE optimization which enables the design of either an arbitrary RF phase pattern with a prescribed rotation angle, or a specific RF phase pattern with a prescribed rotation angle. The GRAPE algorithm presents several advantages compared to other optimization strategies ([Eggenschwiler et al., 2013](#)), as it makes no approximation such as the linear class of large tip angle ([Pauly et al., 1989b](#)) and fully takes into account  $\Delta B_0$  offsets for each pulse. Not properly taking into account the latter likely introduces a loss of coherence among the different echoes and thus a loss of signal in the image. Considering our pulse design, because the duration of the pulses varied across the pulse train, it was critical to ensure the same free evolution time between all consecutive pulses. Last, CPMG conditions are kept to comply with the assumptions made in the flip angle series algorithm ([Mugler, 2000](#)) and therefore reduce the latitude in the optimization process. A very interesting approach would be then to ignore CPMG conditions, model and optimize the signal throughout the SPACE sequence with the SR-EPG framework, as

suggested in (Malik et al., 2012), and include this into a whole iterative pulse design procedure.

It has been found in practice that the choice of the initial candidate pulse influences only to some extent the final result of the GRAPE optimization. Indeed, the k-space trajectory optimization is partially addressed using the GRAPE algorithm but somewhat restricted, as we note that the large number of control parameters may trap the cost function in non-optimal local minima. This is why RF pulses used as initial guesses in this study were already self-refocused pulses with fairly good refocusing performance. When non-self-refocused pulses with random k-space trajectories are used as initial guesses, improvements of the cost functions shown here are considerably larger, but in the end they always achieve worse (yet comparable) refocusing performances than self-refocused initial guesses. The full optimization of the  $k_T$ -points number, locations and order, remains the topic of further study.

In this study, neither additional local SAR constraints nor energy deposition penalties were taken into account. Indeed, despite the compression model of SAR constraints through VOPs (Virtual Observation Points) (Eichfelder and Gebhardt, 2011; Lee et al., 2012), taking directly into account the SAR in the optimization procedure does not seem tractable yet due to the large number of degrees of freedom considered here (about 3000 only for the excitation pulse for instance). Nevertheless, perhaps the use of second-order optimization methods (de Fouquieres et al., 2011; Hoyos-Idrobo et al., 2013) could reduce substantially this number while still achieving good performance. These endeavors led the way to pulse design achieving very good mitigation performances with direct local SAR constraints (Brunner and Pruessmann, 2010; Guérin et al., 2013; Hoyos-Idrobo et al., 2013), or even with local temperature constraints (Boulant et al., 2013). This is also the subject of future work.

Since refocusing pulses of variable angles are used in the SPACE sequence, the magnetization vector is not purely transverse throughout the echo train: its decay occurs more slowly than  $T_2$ , and image contrast is altered by  $T_1$  relaxation through stimulated echoes (Busse et al., 2006). The effective TE (defined as the time at which the center of k-space is sampled) thus no longer corresponds to the expected amount of spin-echo  $T_2$  contrast. In our sequence, the effective TE was directly set by the Partial Fourier factor, yet several studies (Hennig and Scheffler, 2001; Hennig et al., 2004) suggest delaying the sampling of the center of k-space to retrieve the original  $T_2$  contrast from  $180^\circ$  refocusing. This complex matter, which requires a dedicated study, is beyond the scope of this work, whose purpose was only signal conservation for a specified  $T_1/T_2$  target. Regarding the FLAIR contrast at 7T, the incomplete recovery of GM and WM at TI, due to the prolonged  $T_1$  relaxation, alters the observed  $T_2$  contrast, as well as image SNR (Visser et al., 2010). These

issues could be overcome with a dedicated magnetization preparation block prior to the excitation with the cost of higher SAR ([Visser et al., 2010](#)).

Although in-vivo images were obtained with fairly high resolution (0.8 mm isotropic), still better in-plane resolution could be achieved without any SAR and acquisition time increase. Indeed, for the same TR, a greater acceleration factor could be used and/or more echoes could be inserted to acquire more lines of the k-space. In that case, the values of the angles prescribed by the pseudo-steady state algorithm are lower, thus maintaining the SAR level of the sequence at an interestingly similar value. However higher resolution would require more SNR and consequently better coil-arrays than the one used in this study. This is why the pTX methods comparison done in this work was made on images of 1 mm isotropic resolution, considering the poor SNR obtained here with conventional pTX methods. In future studies, the receive performance should be enhanced substantially by including a dedicated receive loop-array. As far as SAR is concerned, a less conservative approach is required if one wants to decrease the acquisition time, or when more energy is needed to increase spatial resolution in partition direction while keeping a similar acquisition time.

For the moment, about 6 preliminary minutes of subject-specific calibration data acquisition are still necessary at the beginning of a pTx exam; this duration is likely to decrease in the near future. Pulse design itself can presumably be done while performing a more basic MRI acquisition, in order to save time.

## 7.6. Conclusion

In the end, we have demonstrated the soundness of the GRAPE pulse design method in the framework of parallel transmission applied to  $T_2$ -weighted 3D-imaging of the human brain at 7 Tesla. Replacing the original hard pulses of a SPACE sequence by our tailored pulses provides restoration of the expected excitation/refocusing uniform distribution, and consequently  $T_2$ -weighted images of high quality in terms of signal and contrast homogeneity.

# General Conclusion & Perspectives

In the framework of medical imaging, with the aim of generating always better-resolved MR images, ultra-high main magnetic field strengths are explored. While progressively ramping up the static field enhances the NMR signal, it simultaneously increases the proton Larmor frequency. Considering clinical systems operating at 3 Tesla, the corresponding RF wavelength already becomes comparable to the dimensions of the human body. As a result, when investigating large organs, zones of shades and losses of contrast arise in the image. Migrating to 7 Tesla, the resulting RF non-uniformities are so strong that these artifacts happen even in smaller regions such as the human brain. In preparation of the arrival of the 11.7 Tesla system dedicated to human imaging at NeuroSpin, it becomes increasingly urgent to provide adequate solutions to mitigate these excitation non-uniformities. Otherwise, such ultra-high field systems cannot reach their full potential.

To develop the techniques necessary to tackle the above-mentioned challenges, an 8-channel parallel transmission setup was installed in our 7 Tesla MRI system. Whereas most clinical MRI systems only use one transmit-channel at a time, the pTX extension allows different RF waveforms to be played through multiple channels in concert. The additional degrees of freedom provided by this pTX extension can be used to mitigate excitation non-uniformities and reach solutions with more favorable energy distributions.

Nevertheless, the inherent potential occurrence of highly localized energy depositions in the imaged subject during a pTX exam requires special care to ensure safety. This is why numerical simulations were performed in order to assess the compliance of the SAR guidelines with the biological primary biological parameter of interest: the temperature, to avoid local thermal damage or thermoregulatory problems, in the context of parallel transmission MRI at 7 Tesla. Based on Pennes' bioheat equation, these simulations showed that the local temperature inside the human head never exceeds 39 °C (and barely 38 °C) but temperature rises larger than 1 °C may occur in the eye, when using the recommended values of SAR in parallel transmission MRI exams.

The core of this thesis was a new pTX-based pulse design strategy relying on optimal control, introduced to tackle non-selective uniform refocusing at UHF in any spin echo-based 3D MRI sequence. This approach was first experimentally validated by using Quantum Process Tomography and standard spin-echo sequences. In the end, the soundness of the GRAPE pulse design method in the framework of parallel transmission applied to  $T_2$ -weighted 3D-imaging of the human brain at 7 Tesla was demonstrated, providing restoration of the expected excitation/refocusing uniform distribution.

The work presented herein completes what was done at NeuroSpin regarding MRI sequences such as GRE or MP-RAGE, giving the community potent tools to perform anatomical 3D imaging at UHF. As this thesis comes to its end, other current endeavors at NeuroSpin focus on: pulse optimization under strict SAR constraints, brain local temperature estimation, homogeneous 2D imaging, ultra-fast echo-planar imaging, simultaneous multi-slice imaging, advanced coil design, inner volume excitation and selection, and many more exciting fields of study.

# List of Publications

## International peer-reviewed journals:

N Boulant, M Bottlaender, L Uhrig, E Giacomini, M Luong, A Amadon, **A Massire**, B Larrat, A Vignaud. FID navigator-based MR-Thermometry method to monitor small temperature changes in the brain of ventilated animals. NMR in Biomedicine, in review (2014).

**A Massire**, A Vignaud, B Robert, D Le Bihan, N Boulant, A Amadon. Parallel-transmission-enabled 3D T<sub>2</sub>-weighted imaging of the human brain at 7 Tesla. Magnetic Resonance in Medicine, doi: 10.1002/mrm.25353 (2014).

N Boulant, **A Massire**, A Amadon, A Vignaud. Parallel transmission pulse design under strict temperature constraints. Magnetic Resonance in Medicine, doi: 10.1002/mrm.24974 (2014).

A Hoyos-Idrobo, P Weiss, **A Massire**, A Amadon, N Boulant. On variant strategies to solve the Magnitude Least Squares optimization problem in parallel transmission RF pulse design and under strict SAR and power constraints. IEEE Transactions on Medical Imaging 33:739-748 (2014).

**A Massire**, MA Cloos, A Vignaud, D Le Bihan, A Amadon, N Boulant. Design of non-selective refocusing pulses with phase-free rotation axis by gradient ascent pulse engineering in parallel transmission at 7 T. Journal of Magnetic Resonance 230:76-83 (2013).

**A Massire**, MA Cloos, M Luong, A Amadon, A Vignaud, CJ Wiggins, N Boulant. Thermal simulations in the human head for high field MRI using Parallel Transmission. Journal of Magnetic Resonance Imaging 35:1312-1321 (2012).

## Proceedings:

### - International Society of Magnetic Resonance in Medicine, Milan, Italy, 2014:

**A Massire**, A Vignaud, A Amadon, B Robert, D Le Bihan, N Boulant. Parallel-transmission-enabled 3D T<sub>2</sub>-weighted imaging of the human brain at 7 Tesla. **Oral ("Magna cum Laude" Award)**

N Boulant, **A Massire**, A Amadon, A Vignaud. Parallel transmission pulse design under strict temperature constraints. **Oral**



A Hoyos-Idrobo, P Weiss, **A Massire**, A Amadon, N Boulant. On variant strategies to solve the Magnitude Least Squares optimization problem in parallel transmission RF pulse design and under strict SAR and power constraints. **Poster**

N Boulant, A Vignaud, E Giacomini, B Larrat, **A Massire**, A Amadon, L Uhrig, M Bottlaender. New MR thermometry approach to follow small temperature variation: in-vivo validation on the anesthetized baboon's brain at 7T. **Poster**

N Boulant, U Katscher, M Luong, **A Massire**, A Amadon, A Vignaud.  $B_1^+$ -based SAR assessment using a birdcage coil at 7 Tesla: experimental evaluation using magnetic resonance thermometry. **Poster**

F Mauconduit, **A Massire**, N Boulant, A Amadon, A Vignaud. Reception sensitivity inhomogeneity correction at ultra-high field using a fast gradient echo sequence. **Poster**

#### **- International Society of Magnetic Resonance in Medicine, Salt-Lake City, USA, 2013:**

**A Massire**, MA Cloos, A Vignaud, D Le Bihan, A Amadon, N Boulant. Design of non-selective refocusing pulses with phase-free rotation axis by gradient ascent algorithm in parallel transmission at 7 T. **Poster**

N Boulant, **A Massire**, A Amadon. First implementation of quantum process tomography in MRI. **Poster**

A Amadon, A Vignaud, **A Massire**, M Bottlaender, N Boulant. Is a 2D-spiral excitation trajectory sufficient for 3D Inner Volume Imaging? **Poster**

#### **- International Society of Magnetic Resonance in Medicine, Melbourne, Australia, 2012:**

**A Massire**, MA Cloos, M Luong, A Amadon, A Vignaud, CJ Wiggins, N Boulant. Thermal simulations in the human head for high field MRI using parallel transmission. **Poster**

#### **Patents:**

**A Massire**, N Boulant (2014). A method of designing and generating pulse for Magnetic Resonance Imaging. European Patent n°14165238.8

# Nomenclature

<b>ADC</b>	Analog-to-Digital Converter
<b>AFI</b>	Actual Flip-angle Imaging
<b>ASE</b>	Anatomical Structure Entity
<b>ASL</b>	Arterial Spin Labeling
<b>B<sub>0</sub></b>	Static magnetic field
<b>B<sub>1</sub><sup>+</sup></b>	Transmit sensitivity
<b>B<sub>1</sub><sup>-</sup></b>	Receive sensitivity
<b>BOLD</b>	Blood Oxygen Level Dependent effect
<b>BW</b>	Bandwidth
<b>C++</b>	C Object-Oriented Programming Language
<b>CNR</b>	Contrast-to-Noise Ratio
<b>CP</b>	Circularly Polarized
<b>CPMG</b>	Carr-Purcell-Meiboom-Gill
<b>CSF</b>	Cerebrospinal fluid
<b>CT</b>	Computed Tomography
<b>CUDA</b>	Compute Unified Device Architecture
<b>ΔB<sub>0</sub></b>	Static magnetic field offset
<b>DIR</b>	Double Inversion Recovery
<b>dMRI</b>	Diffusion Magnetic Resonance Imaging
<b>DREAM</b>	Dual Refocusing Echo Acquisition Mode
<b>ECG</b>	Electrocardiography
<b>EEG</b>	Electroencephalography
<b>EMF</b>	Electromotive force
<b>EPG</b>	Extended Phase Graph
<b>EP</b>	Echo Planar
<b>EPI</b>	Echo Planar Imaging
<b>ES</b>	Echo Spacing
<b>ETL</b>	Echo Train Length
<b>FA</b>	Flip Angle
<b>FDTD</b>	Finite-Difference-Time-Domain
<b>FEM</b>	Finite Element Method
<b>FID</b>	Free Induction Decay
<b>FLASH</b>	Fast low angle shot

<b>FLAIR</b>	Fluid Attenuation Inversion Recovery
<b>FM</b>	Frequency Modulation
<b>fMRI</b>	Functional Magnetic Resonance Imaging
<b>FSE</b>	Fast Spin Echo
<b>GM</b>	Gray Matter
<b>GPU</b>	Graphics Processing Units
<b>GRAPE</b>	Gradient ascent pulse engineering
<b>GRAPPA</b>	GeneRalized Autocalibrating Partially Parallel Acquisitions
<b>GRASE</b>	Gradient Spin Echo
<b>GRE</b>	Gradient-Recalled Echo
<b>IEC</b>	International Electrotechnical Commission
<b>L2</b>	Euclidian Norm
<b>LCLTA</b>	Linear Class of Large-Tip-Angle
<b>LTA</b>	Large-Tip-Angle
<b>LS</b>	Least Square
<b>M<sub>0</sub></b>	Magnetization vector at equilibrium
<b>MEG</b>	Magnetoencephalography
<b>MLS</b>	Magnitude Least Square
<b>MP-RAGE</b>	Magnetization-prepared rapid gradient echo
<b>MR</b>	Magnetic Resonance
<b>MRA</b>	Magnetic Resonance Angiography
<b>MRI</b>	Magnetic Resonance Imaging
<b>MRS</b>	Magnetic Resonance Spectroscopy
<b>M<sub>T</sub></b>	Transverse Magnetization
<b>M<sub>z</sub></b>	Longitudinal Magnetization
<b>MRM</b>	Magnetic Resonance Microscopy
<b>NMR</b>	Nuclear Magnetic Resonance
<b>NRMSE</b>	Normalized Root Mean Square Error
<b>OCA</b>	Optimal Control Approach
<b>PET</b>	Positron Emission Tomography
<b>PD</b>	Proton Density
<b>PRFS</b>	Proton Resonance Frequency Shift
<b>PSS</b>	Pseudo-Steady-State
<b>pTX</b>	Parallel transmission
<b>QPT</b>	Quantum Process Tomography
<b>RA</b>	Rotation Angle
<b>RARE</b>	Rapid Acquisition with Relaxation Enhancement

<b>RF</b>	Radio Frequency
<b>ROI</b>	Region of Interest
<b>SAR</b>	Specific Absorption Rate
<b>SD</b>	Standard deviation
<b>SDM</b>	Spatial Domain Method
<b>SE</b>	Spin Echo
<b>SENSE</b>	Sensitivity encoding
<b>SLR</b>	Shinnar-Le Roux
<b>SMASH</b>	Simultaneous Acquisition of Spatial Harmonics
<b>SNR</b>	Signal-to-Noise Ratio
<b>SPACE</b>	Sampling perfection with application optimized contrasts using different flip angle evolution
<b>STA</b>	Small-Tip-Angle
<b>SU(2)</b>	Spin Domain
<b>T1</b>	Spin-lattice relaxation
<b>T2</b>	Spin-spin relaxation
<b>T2*</b>	Apparent spin-spin relaxation
<b>TALES</b>	Transmit Antenna Level Sensor
<b>TE</b>	Time of echo
<b>TOF</b>	Time of Flight
<b>TSE</b>	Turbo Spin Echo
<b>TI</b>	Inversion time
<b>TR</b>	Time of repetition
<b>T/R</b>	Transmit-Receive
<b>UHF</b>	Ultra-high fields
<b>VERSE</b>	Variable-rate selective
<b>VFA</b>	Variable Flip Angle
<b>VOP</b>	Virtual Observation Point
<b>WIFI</b>	Wireless local area network
<b>WM</b>	White matter

# Bibliography

- Adriany, G., Van de Moortele, P-F., Wiesinger, F., Moeller, S., Strupp, J.P., Andersen, P., Snyder, C., Zhang, X., Chen, W., Pruessmann, K.P., Boesiger, P., Vaughan, T., Uğurbil, K., 2005. Transmit and receive transmission line arrays for 7 Tesla parallel imaging. *Magn. Reson. Med.* 53, 434–445.
- Alagappan, V., Nistler, J., Adalsteinsson, E., Setsompop, K., Fontius, U., Zelinski, A., Vester, M., Wiggins, G.C., Hebrank, F., Renz, W., Schmitt, F., Wald, L.L., 2007. Degenerate mode band-pass birdcage coil for accelerated parallel excitation. *Magn. Reson. Med.* 57, 1148–1158.
- Alon, L., Deniz, C.M., Sodickson, D.K., 2011. Do constraints on  $|B_1+|$  also constrain  $|E|$  and SAR in high field MR? In: *Proc. Intl. Soc. Mag. Reson. Med. Montreal, Quebec, Canada*. p. 491.
- Alsop, D.C., 1997. The sensitivity of low flip angle RARE imaging. *Magn. Reson. Med.* 37, 176–184.
- Amadon, A., Boulant, N., 2008. Simultaneous measurement of  $B_0$ - and  $B_1$ -maps with modified Actual Flip Angle Imaging sequence. In: *Proc. Intl. Soc. Mag. Reson. Med. Toronto, Ontario, Canada*. p. 1248.
- Amadon, A., Cloos, M.A., Boulant, N., Hang, M-F., Wiggins, C.J., Fautz, H-P., 2012. Validation of a very fast  $B_1$ -mapping sequence for parallel transmission on a human brain at 7T. In: *Proc. Intl. Soc. Mag. Reson. Med. Melbourne, Australia*, p. 3358.
- Athey, T.W., 1989. A model of the temperature rise in the head due to magnetic resonance imaging procedures. *Magn. Reson. Med.* 9, 177–184.
- Bachmann, R., Reilmann, R., Schwindt, W., Kugel, H., Heindel, W., Krämer, S., 2006. FLAIR imaging for multiple sclerosis: a comparative MR study at 1.5 and 3.0 Tesla. *Eur. Radiol.* 16, 915–921.
- Barber, B.J., Schaefer, D.J., Gordon, C.J., Zawieja, D.C., Hecker, J., 1990. Thermal effects of MR imaging: worst-case studies on sheep. *Am. J. Roentgenol.* 155, 1105–1110.
- Bernardi, P., Cavagnaro, M., Pisa, S., Piuze, E., 2003. Specific absorption rate and temperature elevation in a subject exposed in the far-field of radio-frequency sources operating in the 10-900-MHz range. *IEEE Trans. Biomed. Eng.* 50, 295–304.
- Bernstein, M., King, K.F., Zhou, X., 2004. *Handbook of MRI pulse sequences*. Elsevier Academic Press, London.
- Bloch, F., 1946. Nuclear Induction. *Phys. Rev.* 70, 460–474.
- Borneman, T.W., Hürlimann, M.D., Cory, D.G., 2010. Application of optimal control to CPMG refocusing pulse design. *J. Magn. Reson.* 207, 220–233.
- Bottomley, P.A., Andrew, E.R., 1978. RF magnetic field penetration, phase shift and power dissipation in biological tissue: implications for NMR imaging. *Phys. Med. Biol.* 23, 630–643.
- Bottomley, P.A., Hardy, C.J., 1987. Two-dimensional spatially selective spin inversion and spin-echo refocusing with a single nuclear magnetic resonance pulse. *J. Appl. Phys.* 62, 4284–4290.
- Boulant, N., Havel, T.F., Pravia, M.A., Cory, D.G., 2003. A Robust Method for Estimating the Lindblad Operators of a Dissipative Quantum Process from Measurements of the Density Operator at Multiple Time Points. *Phys. Rev.* 67.
- Boulant, N., Cloos, M.A., Amadon, A., 2010. A simple and analytical way to correct for  $B_0$  inhomogeneity in the evaluation of  $B_1$  maps relying on flip angle measurements and non-selective square pulses. In: *Proc. Intl. Soc. Mag. Reson. Med. Stockholm, Sweden*. p. 4918.
- Boulant, N., Cloos, M.A., Luong, M., Ferrand, G., Wiggins, C.J., Amadon, A., 2011. Method for monitoring safety in parallel transmission systems based on channel-dependent

- average powers. In: Proc. Intl. Soc. Mag. Reson. Med. Montreal, Quebec, Canada. p. 3850.
- Boulant, N., Hoult, D.I., 2012. High tip angle approximation based on a modified Bloch-Riccati equation. *Magn. Reson. Med.* 67, 339–343.
- Boulant, N., Massire, A., Amadon, A., Vignaud, A., 2014. Radiofrequency pulse design in parallel transmission under strict temperature constraints. *Magn. Reson. Med.* doi:10.1002/mrm.24974.
- Boulant, N., Bottlaender, M., Uhrig, L., Giacomini, E., Luong, M., Amadon, A., Massire, A., Larrat, B., Vignaud, A., 2014. FID navigator-based MR-Thermometry method to monitor small temperature changes in the brain of ventilated animals. *NMR Biomed.* In review.
- BrainVISA / Anatomist, 2014. <http://www.brainvisa.info/index.html>. Accessed March 1, 2014.
- Brix, G., Reinl, M., Brinker, G., 2001. Sampling and evaluation of specific absorption rates during patient examinations performed on 1.5-Tesla MR systems. *Magn. Reson. Imaging* 19, 769–779.
- Brix, G., Seebass, M., Hellwig, G., Griebel, J., 2002. Estimation of heat transfer and temperature rise in partial-body regions during MR procedures: an analytical approach with respect to safety considerations. *Magn. Reson. Imaging* 20, 65–76.
- Brunner, D.O., Paska, J., Froehlich, J., Pruessmann, K.P., 2008. SAR assessment of transmit arrays: Deterministic calculation of worst- and best-case performance. In: Proc. Intl. Soc. Mag. Reson. Med, Toronto, Ontario, Canada. p. 4803.
- Brunner, D.O., Pruessmann, K.P., 2008. A matrix approach for mapping array transmit fields in under a minute. In: Proc. Intl. Soc. Mag. Reson. Med, Toronto, Ontario, Canada. p. 354.
- Brunner, D.O., De Zanche, N., Fröhlich, J., Paska, J., Pruessmann, K.P., 2009. Travelling-wave nuclear magnetic resonance. *Nature* 457, 994–998.
- Brunner, D.O., Pruessmann, K.P., 2009. B1(+) interferometry for the calibration of RF transmitter arrays. *Magn. Reson. Med.* 61, 1480–1488.
- Brunner, D.O., Pruessmann, K.P., 2010. Optimal design of multiple-channel RF pulses under strict power and SAR constraints. *Magn. Reson. Med.* 63, 1280–1291.
- Busse, R.F., Hariharan, H., Vu, A., Brittain, J.H., 2006. Fast spin echo sequences with very long echo trains: design of variable refocusing flip angle schedules and generation of clinical  $T_2$  contrast. *Magn. Reson. Med.* 55, 1030–1037.
- Bydder, G.M., Young, I.R., 1985. MR imaging: clinical use of the inversion recovery sequence. *J. Comput. Assist. Tomogr.* 9, 659–675.
- Carr, H.Y., 1952. Free Precession Techniques in Nuclear Magnetic Resonance (Ph.D. thesis, Reprinted in *Encyclopedia of Nuclear Magnetic Resonance*, Vol.I, J.Wiley & Sons 1996, Boston.).
- Carr, H.Y., Purcell, E.M., 1954. Effects of Diffusion on Free Precession in Nuclear Magnetic Resonance Experiments. *Phys. Rev.* 94, 630–638.
- Christ, A., Kainz, W., Hahn, E.G., Honegger, K., Zefferer, M., Neufeld, E., Rascher, W., Janka, R., Bautz, W., Chen, J., Kiefer, B., Schmitt, P., Hollenbach, H-P., Shen, J., Oberle, M., Szczerba, D., Kam, A., Guag, J.W., Kuster, N., 2010. The Virtual Family-development of surface-based anatomical models of two adults and two children for dosimetric simulations. *Phys. Med. Biol.* 55, 23-38.
- Ciobanu, L., Reynaud, O., Uhrig, L., Jarraya, B., Le Bihan, D., 2012. Effects of anesthetic agents on brain blood oxygenation level revealed with ultra-high field MRI. *PloS One* 7.
- Cloos, M.A., Luong, M., Ferrand, G., Amadon, A., Le Bihan, D., Boulant, N., 2010a. Local SAR reduction in parallel excitation based on channel-dependent Tikhonov parameters. *J. Magn. Reson. Imaging* 32, 1209–1216.
- Cloos, M.A., Boulant, N., Luong, M., Ferrand, G., Le Bihan, D., Amadon, A., 2010b. Specific absorption rate monitor for in-vivo parallel transmission at 7 Tesla. In: Proc. Intl. Soc. Mag. Reson. Med, Stockholm, Sweden. p. 3871.

- Cloos, M.A., Boulant, N., Luong, M., Ferrand, G., Giacomini, E., Le Bihan, D., Amadon, A., 2012a.  $k_T$ -points: short three-dimensional tailored RF pulses for flip-angle homogenization over an extended volume. *Magn. Reson. Med.* 67, 72–80.
- Cloos, M.A., Boulant, N., Luong, M., Ferrand, G., Giacomini, E., Hang, M.-F., Wiggins, C.J., Le Bihan, D., Amadon, A., 2012b. Parallel-transmission-enabled magnetization-prepared rapid gradient-echo T1-weighted imaging of the human brain at 7 T. *NeuroImage* 62, 2140–2150.
- Cloos, M.A., 2012. Parallel Transmission for Magnetic Resonance Imaging of the Human Brain at Ultra High Field. Specific Absorption Rate Control & Flip-Angle Homogenization. PhD Thesis. Paris XI.
- Collins, C.M., Liu, W., Wang, J., Gruetter, R., Vaughan, J.T., Ugurbil, K., Smith, M.B., 2004. Temperature and SAR calculations for a human head within volume and surface coils at 64 and 300 MHz. *J. Magn. Reson. Imaging* 19, 650–656.
- Collins, C.M., Wang, Z., Smith, M.B., 2007. A Conservative method for ensuring safety within transmit arrays. In: *Proc. Intl. Soc. Mag. Reson. Med.* Berlin, Germany. p. 1092.
- Conolly, S., Nishimura, D., Macovski, A., 1986. Optimal Control Solutions to the Magnetic Resonance Selective Excitation Problem. *IEEE Trans. Med. Imaging* 5, 106–115.
- Constable, R.T., Anderson, A.W., Zhong, J., Gore, J.C., 1992. Factors influencing contrast in fast spin-echo MR imaging. *Magn. Reson. Imaging* 10, 497–511.
- De Fouquieres, P., Schirmer, S.G., Glaser, S.J., Kuprov, I., 2011. Second order gradient ascent pulse engineering. *J. Magn. Reson.* 212, 412–417.
- De Graaf, W.L., Zwanenburg, J.J.M., Visser, F., Wattjes, M.P., Pouwels, P.J.W., Geurts, J.J.G., Polman, C.H., Barkhof, F., Luijten, P.R., Castelijns, J.A., 2012. Lesion detection at seven Tesla in multiple sclerosis using magnetization prepared 3D-FLAIR and 3D-DIR. *Eur. Radiol.* 22, 221–231.
- Deng, W., Yang, C., Stenger, V.A., 2011. Multi-dimensional refocusing pulses for parallel transmission by optimal control. In: *Proc. Intl. Soc. Mag. Reson. Med.* Montreal, Quebec, Canada. p. 2900.
- Eggenschwiler, F., O'Brien, K.R., Gruetter, R., Marques, J.P., 2013. Improving  $T_2$ -weighted imaging at high field through the use of  $k_T$ -points. *Magn. Reson. Med.* doi:10.1002/mrm.24805.
- Eichfelder, G., Gebhardt, M., 2011. Local specific absorption rate control for parallel transmission by virtual observation points. *Magn. Reson. Med.* 66, 1468–1476.
- Epstein, F.H., Mugler, J.P., Brookeman, J.R., 1996. Spoiling of transverse magnetization in gradient-echo (GRE) imaging during the approach to steady state. *Magn. Reson. Med.* 35, 237–245.
- Fan, K., Hoffman, J., 1955. Some metric inequalities in the space of matrices. *Proc. Am. Math. Soc.* 6, 111–116.
- Fautz, H-P., Vogel, M.W., Gross, P., Kerr, A.B., Zhu, Y., 2008. B1 mapping of coil arrays for parallel transmission. In: *Proc. Intl. Soc. Mag. Reson. Med.* Toronto, Ontario, Canada, p. 1247.
- Favazza, C., Gorny, K., Felmlee, J., 2013. Experimental Evaluation of RF Shield at 1.5 and 3.0 Tesla MRI. Presented at the AAPM Spring Clinical Meeting, Phoenix, AZ, USA.
- Feinberg, D.A., Mills, C.M., Posin, J.P., Ortendahl, D.A., Hylton, N.M., Crooks, L.E., Watts, J.C., Kaufman, L., Arakawa, M., Hoenninger, J.C., 1985. Multiple spin-echo magnetic resonance imaging. *Radiology* 155, 437–442.
- Ferrand, G., Luong, M., France, A., 2010. Antenne pour système IRM. Patent Application No. 1050905.
- Frahm, J., Haase, A., Matthaei, D., 1986. Rapid NMR imaging of dynamic processes using the FLASII technique. *Magn. Reson. Med.* 3, 321–327.
- Frieden, E., 1972. The Chemical Elements of Life. *Sci. Am.* 52–60.
- Gagoski, B.A., Gumbrecht, R., Hamm, M., Setsompop, K., Keil, B., Lee, J., Makhoul, K., Mareyam, A., Fujimoto, K., Witzel, T., Fontius, U., Pfeuffer, J., Adalsteinsson, E., Wald, L.L., 2009. Real time RF monitoring in a 7T parallel transmit system. In: *Proc. Intl. Soc. Mag. Reson. Med.* Stockholm, Sweden. p. 781.

- Garwood, M., Ke, Y., 1991. Symmetric pulses to induce arbitrary flip angles with compensation for rf inhomogeneity and resonance offsets. *J. Magn. Reson.* 94, 511–525.
- Ge, Y., Grossman, R.I., Babb, J.S., Rabin, M.L., Mannon, L.J., Kolson, D.L., 2002. Age-Related Total Gray Matter and White Matter Changes in Normal Adult Brain. Part I: Volumetric MR Imaging Analysis. *Am. J. Neuroradiol.* 23, 1327–1333.
- Graesslin, I., Schweser, F., Annighefer, B., 2008. A minimum SAR RF pulse design approach for parallel Tx with local hot spot suppression and exact fidelity constraint. In: *Proc. Intl. Soc. Mag. Reson. Med*, Toronto, Ontario, Canada. p. 621.
- Graesslin, I., Biederer, S., Annighefer, B., Homann, H., Stahl, H., Vernickel, P., Katscher, U., Glaesel, D., Harvey, P., 2009a. Real-time global and local SAR monitoring for parallel transmission systems. In: *Proc. Intl. Soc. Mag. Reson. Med*, Honolulu, Hawaii, USA. p. 302.
- Graesslin, I., Weller, J., Annighefer, B., 2009b. SAR hotspot reduction by temporal averaging in parallel transmission. In: *Proc. Intl. Soc. Mag. Reson. Med*, Honolulu, Hawaii, USA. p. 176.
- Graesslin, I., Homann, H., Biederer, S., Börnert, P., Nehrke, K., Vernickel, P., Mens, G., Harvey, P., Katscher, U., 2012. A specific absorption rate prediction concept for parallel transmission MR. *Magn. Reson. Med.* 68, 1664–1674.
- Grissom, W., Yip, C., Zhang, Z., Stenger, V.A., Fessler, J.A., Noll, D.C., 2006. Spatial domain method for the design of RF pulses in multicoil parallel excitation. *Magn. Reson. Med.* 56, 620–629.
- Grissom, W.A., Yip, C.-Y., Wright, S.M., Fessler, J.A., Noll, D.C., 2008. Additive angle method for fast large-tip-angle RF pulse design in parallel excitation. *Magn. Reson. Med.* 59, 779–787.
- Grissom, W.A., Xu, D., Kerr, A.B., Fessler, J.A., Noll, D.C., 2009. Fast large-tip-angle multidimensional and parallel RF pulse design in MRI. *IEEE Trans. Med. Imaging* 28, 1548–1559.
- Griswold, M.A., Jakob, P.M., Heidemann, R.M., Nittka, M., Jellus, V., Wang, J., Kiefer, B., Haase, A., 2002. Generalized autocalibrating partially parallel acquisitions (GRAPPA). *Magn. Reson. Med.* 47, 1202–1210.
- Guérin, B., Gebhardt, M., Cauley, S., Adalsteinsson, E., Wald, L.L., 2013. Local specific absorption rate (SAR), global SAR, transmitter power, and excitation accuracy trade-offs in low flip-angle parallel transmit pulse design. *Magn. Reson. Med.* doi:10.1002/mrm.24800.
- Haase, A., Frahm, J., Matthaei, D., Hanicke, W., Merboldt, K.-D., 1986. FLASH imaging. Rapid NMR imaging using low flip-angle pulses. *J. Magn. Reson.* 67, 258–266.
- Hahn, E.L., 1950a. Nuclear Induction Due to Free Larmor Precession. *Phys. Rev.* 77, 297–298.
- Hahn, E.L., 1950b. Spin Echoes. *Phys. Rev.* 80, 580–594.
- Hajnal, J.V., Bryant, D.J., Kasuboski, L., Pattany, P.M., De Coene, B., Lewis, P.D., Pennock, J.M., Oatridge, A., Young, I.R., Bydder, G.M., 1992a. Use of fluid attenuated inversion recovery (FLAIR) pulse sequences in MRI of the brain. *J. Comput. Assist. Tomogr.* 16, 841–844.
- Hajnal, J.V., De Coene, B., Lewis, P.D., Baudouin, C.J., Cowan, F.M., Pennock, J.M., Young, I.R., Bydder, G.M., 1992b. High signal regions in normal white matter shown by heavily T<sub>2</sub>-weighted CSF nulled IR sequences. *J. Comput. Assist. Tomogr.* 16, 506–513.
- Havel, T.F., 2002. Procedures for Converting among Lindblad, Kraus and Matrix Representations of Quantum Dynamical Semigroups. *J. Math. Phys.*
- Hayes, C.E., Edelstein, W.A., Schenck, J.F., Mueller, O.M., Eash, M., 1985. An efficient, highly homogeneous radiofrequency coil for whole-body NMR imaging at 1.5 T. *J. Magn. Reson.* 63, 622–628.
- Hendrick, R., 1999. Image contrast and noise. St. Louis. ed, In *Magnetic Resonance Imaging*. D.D. Stark and W.G. Bradley.



- Hennig, J., Nauerth, A., Friedburg, H., 1986. RARE imaging: A fast imaging method for clinical MR. *Magn. Reson. Med.* 3, 823–833.
- Hennig, J., 1988. Multiecho imaging sequences with low refocusing flip angles. *J. Magn. Reson.* 78, 397–407.
- Hennig, J., 2000. Easy improvement of signal-to-noise in RARE-sequences with low refocusing flip angles. *Magn. Reson. Med.* 44, 983–985.
- Hennig, J., Scheffler, K., 2001. Hyperechoes. *Magn. Reson. Med.* 46, 6–12.
- Hennig, J., Weigel, M., Scheffler, K., 2003. Multiecho sequences with variable refocusing flip angles: Optimization of signal behavior using smooth transitions between pseudo steady states (TRAPS). *Magn. Reson. Med.* 49, 527–535.
- Hennig, J., Weigel, M., Scheffler, K., 2004. Calculation of flip angles for echo trains with predefined amplitudes with the extended phase graph (EPG)-algorithm: Principles and applications to hyperecho and TRAPS sequences. *Magn. Reson. Med.* 51, 68–80.
- Hindman, J.C., 1966. Proton Resonance Shift of Water in the Gas and Liquid States. *J. Chem. Phys.* 44, 4582–4592.
- Hoult, D.I., Lauterbur, P.C., 1979. The sensitivity of the zeugmatographic experiment involving human samples. *J. Magn. Reson.* 34, 425–433.
- Hoult, D.I., Bhakar, B., 1997. NMR signal reception: Virtual photons and coherent spontaneous emission. *Concepts Magn. Reson.* 9, 277–297.
- Hoyos-Idrobo, A., Weiss, P., Massire, A., Amadon, A., Boulant, N., 2013. On Variant Strategies To Solve The Magnitude Least Squares Optimization Problem In Parallel Transmission Pulse Design And Under Strict SAR And Power Constraints. *IEEE Trans. Med. Imaging.* doi:10.1109/TMI.2013.2295465.
- Ibrahim, T.S., Lee, R., Baertlein, B.A., Kangarlu, A., Robitaille, P.-M.L., 2000. Application of finite difference time domain method for the design of birdcage RF head coils using multi-port excitations. *Magn. Reson. Imaging* 18, 733–742.
- Ibrahim, T.S., Abduljalil, A.M., Baertlein, B.A., Lee, R., Robitaille, P.M., 2001. Analysis of B1 field profiles and SAR values for multi-strut transverse electromagnetic RF coils in high field MRI applications. *Phys. Med. Biol.* 46, 2545–2555.
- ICNIRP statement on the “Guidelines for limiting exposure to time-varying electric, magnetic, and electromagnetic fields (up to 300 GHz)”, 2004. *Health Phys.* 197–216.
- International Electrotechnical Commission. Medical electrical equipment-part 2–33: particular requirements for the basic safety and essential performance of magnetic resonance equipment for medical diagnosis, 2010. Geneva. p. 2–33.
- Jelescu, I.O., Nargeot, R., Le Bihan, D., Ciobanu, L., 2013. Highlighting manganese dynamics in the nervous system of *Aplysia californica* using MEMRI at ultra-high field. *NeuroImage* 76, 264–271.
- Katscher, U., Börnert, P., Leussler, C., van den Brink, J.S., 2003. Transmit SENSE. *Magn. Reson. Med.* 49, 144–150.
- Katscher, U., Röhrs, J., Börnert, P., 2005. Basic considerations on the impact of the coil array on the performance of Transmit SENSE. *Magn. Reson. Mater. Phys. Biol. Med.* 18, 81–88.
- Katscher, U., Börnert, P., 2006. Parallel RF transmission in MRI. *NMR Biomed.* 19, 393–400.
- Katscher, U., Börnert, P., 2007. Parallel magnetic resonance imaging. *Neurotherapeutics* 4, 499–510.
- Katscher, U., Findelee, C., Voigt, T., 2012. B1-based specific energy absorption rate determination for nonquadrature radiofrequency excitation. *Magn. Reson. Med.* 68, 1911–1918.
- Kerr, A.B., Zhu, Y., Pauly, J.M., 2007. Phase Constraint Relaxation in Parallel Excitation Pulse Design. In: *Proc. Intl. Soc. Mag. Reson. Med.*, Berlin, Germany. p. 1694.
- Khaneja, N., Reiss, T., Kehlet, C., Schulte-Herbrüggen, T., Glaser, S.J., 2005. Optimal control of coupled spin dynamics: design of NMR pulse sequences by gradient ascent algorithms. *J. Magn. Reson.* 172, 296–305.

- Kozlov, M., Rothe, T., Turner, R., 2009. Optimization of SAR calculation for 3-D EM time and frequency domain data. In: Proc. Intl. Soc. Mag. Reson. Med, Honolulu, Hawai, USA. p. 4779.
- Kozlov, M., Turner, R., 2009. Fast MRI coil analysis based on 3-D electromagnetic and RF circuit co-simulation. *J. Magn. Reson.* 200, 147–152.
- Kuroda, K., Oshio, K., Chung, A.H., Hynynen, K., Jolesz, F.A., 1997. Temperature mapping using the water proton chemical shift: a chemical shift selective phase mapping method. *Magn. Reson. Med.* 38, 845–851.
- Kwong, K.K., Belliveau, J.W., Chesler, D.A., Goldberg, I.E., Weisskoff, R.M., Poncelet, B.P., Kennedy, D.N., Hoppel, B.E., Cohen, M.S., Turner, R., 1992. Dynamic magnetic resonance imaging of human brain activity during primary sensory stimulation. *Proc. Natl. Acad. Sci.* 89, 5675–5679.
- Lauterbur, P.C., 1973. Image Formation by Induced Local Interactions: Examples Employing Nuclear Magnetic Resonance. *Nature* 242, 190–191.
- Le Bihan, D., Breton, E., 1985. Imagerie de diffusion in vivo par résonance magnétique nucléaire. *Comptes Rendus Académie Sci. Sér. 2 Mécanique Phys. Chim. Sci. Univers Sci. Terre* 301, 1109–1112.
- Le Roux, P., Hinks, R.S., 1993. Stabilization of echo amplitudes in FSE sequences. *Magn. Reson. Med.* 30, 183–190.
- Lee, J., Gebhardt, M., Wald, L.L., Adalsteinsson, E., 2012. Local SAR in parallel transmission pulse design. *Magn. Reson. Med.* 67, 1566–1578.
- Ma, D., Gulani, V., Seiberlich, N., Liu, K., Sunshine, J.L., Duerk, J.L., Griswold, M.A., 2013. Magnetic resonance fingerprinting. *Nature* 495, 187–192.
- Madelin, G., Oesingmann, N., Inglese, M., 2010. Double Inversion Recovery MRI with Fat Suppression at 7 Tesla: Initial Experience. *J. Neuroimaging* 20, 87–92.
- Magill, A.W., Schaller, B., Gruetter, R., 2010. Balanced microstip feeds. In: Proc. Intl. Soc. Mag. Reson. Med, Stockholm, Sweden. p. 1520.
- Mainero, C., Benner, T., Radding, A., van der Kouwe, A., Jensen, R., Rosen, B.R., Kinkel, R.P., 2009. In vivo imaging of cortical pathology in multiple sclerosis using ultra-high field MRI. *Neurology* 73, 941–948.
- Makris, N., Angelone, L., Tulloch, S., Sorg, S., Kaiser, J., Kennedy, D., Bonmassar, G., 2008. MRI-based anatomical model of the human head for specific absorption rate mapping. *Med. Biol. Eng. Comput.* 46, 1239–1251.
- Malik, S.J., Padormo, F., Price, A.N., Hajnal, J.V., 2012. Spatially resolved extended phase graphs: modeling and design of multipulse sequences with parallel transmission. *Magn. Reson. Med.* 68, 1481–1494.
- Mansfield, P., 1977. Multi-planar image formation using NMR spin echoes. *J. Phys. C: Solid State Phys.* 10, 55–58.
- Mansfield, P., Maudsley, A.A., 1977. Planar spin imaging by NMR. *J. Magn. Reson.* 27, 101–119.
- Mao, W., Wang, Z., Smith, M.B., Collins, C.M., 2007. Calculation of SAR for Transmit Coil Arrays. *Concepts Magn. Reson. Magn. Reson. Eng.* 31B, 127–131.
- Massire, A., Cloos, M.A., Luong, M., Amadon, A., Vignaud, A., Wiggins, C.J., Boulant, N., 2012. Thermal simulations in the human head for high field MRI using parallel transmission. *J. Magn. Reson. Imaging* 35, 1312–1321.
- Massire, A., Cloos, M.A., Vignaud, A., Le Bihan, D., Amadon, A., Boulant, N., 2013. Design of non-selective refocusing pulses with phase-free rotation axis by gradient ascent pulse engineering algorithm in parallel transmission at 7T. *J. Magn. Reson.* 230, 76–83.
- Mauconduit, F., Massire, A., Boulant, N., Amadon, A., Vignaud, A., 2014. Reception sensitivity inhomogeneity correction at ultra-high field using a fast gradient echo sequence. In: Proc. Intl. Soc. Mag. Reson. Med, Milan, Italy, p. 1642.
- Meiboom, S., Gill, D., 1958. Modified Spin-Echo Method for Measuring Nuclear Relaxation Times. *Rev. Sci. Instrum.* 29, 688–691.

- Moore, J., Jankiewicz, M., Anderson, A.W., Gore, J.C., 2012. Evaluation of non-selective refocusing pulses for 7 T MRI. *J. Magn. Reson.* 214, 212–220.
- Mount, L.E., 1979. Adaptation to thermal environment: man and his productive animals. E. Arnold.
- Mugler, J.P. 3rd, Brookeman, J.R., 1990. Three-dimensional magnetization-prepared rapid gradient-echo imaging (3D MP RAGE). *Magn. Reson. Med.* 15, 152–157.
- Mugler, J.P., 3rd, 2000. Three-dimensional  $T_2$ -weighted imaging of the brain using very long spin-echo trains. In: *Proc. Intl. Soc. Mag. Reson. Med*, Denver, Colorado, USA, p. 687.
- Nehrke, K., 2009. On the steady-state properties of actual flip angle imaging (AFI). *Magn. Reson. Med.* 61, 84–92.
- Nehrke, K., Börnert, P., 2012. DREAM-a novel approach for robust, ultrafast, multislice B1 mapping. *Magn. Reson. Med.* 68, 1517–1526.
- Nielsen, M.A., Chuang, I.L., 2010. *Quantum Computation and Quantum Information: 10th Anniversary Edition*, Cambridge University Press, Cambridge ; New York.
- Ogawa, S., Lee, T.M., Kay, A.R., Tank, D.W., 1990. Brain magnetic resonance imaging with contrast dependent on blood oxygenation. *Proc. Natl. Acad. Sci.* 87, 9868–9872.
- Ohliger, M.A., Sodickson, D.K., 2006. An introduction to coil array design for parallel MRI. *NMR Biomed.* 19, 300–315.
- Oshio, K., Feinberg, D.A., 1991. GRASE (Gradient- and spin-echo) imaging: a novel fast MRI technique. *Magn. Reson. Med.* 20, 344–349.
- Pauly, J., Nishimura, D., Macovski, A., 1989a. A k-space analysis of small-tip-angle excitation. *J. Magn. Reson.* 213, 544–557.
- Pauly, J., Nishimura, D., Macovski, A., 1989b. A linear class of large-tip-angle selective excitation pulses. *J. Magn. Reson.* 82, 571–587.
- Pauly, J., Le Roux, P., Nishimura, D., Macovski, A., 1991. Parameter relations for the Shinnar-Le Roux selective excitation pulse design algorithm [NMR imaging]. *IEEE Trans. Med. Imaging* 10, 53–65.
- Pauly, J.M., Spielman, D., Meyer, C.H., Macovski, A., 1993. A RARE-spiral pulse sequence. In: *Proc. Intl. Soc. Mag. Reson. Med*, Kyoto, Japan. p. 1258.
- Pennes, H.H., 1948. Analysis of tissue and arterial blood temperatures in the resting human forearm. *J. Appl. Physiol.* 85.
- Press, W.H., Teukolsky, S.A., Vetterling, W.T., Flannery, B.P., 2007. *Numerical Recipes 3rd Edition: The Art of Scientific Computing*, Cambridge University Press, Cambridge, UK ; New York.
- Pruessmann, K.P., Weiger, M., Scheidegger, M.B., Boesiger, P., 1999. SENSE: sensitivity encoding for fast MRI. *Magn. Reson. Med.* 42, 952–962.
- Rabi, I.I., Zacharias, J.R., Millman, S., Kusch, P., 1938. A New Method of Measuring Nuclear Magnetic Moment. *Phys. Rev.* 53, 318–318.
- Restivo, M.C., van den Berg, C., van Lier, A.L.H.M.W., Polders, D.L., Raaijmaker, A.J.E., Luijten, P.R., Hoogduin, J.M., 2014. The Effect of Brain Tumors on Local SAR Levels at 7T. In: *Proc. Intl. Soc. Mag. Reson. Med*, Milan, Italy, p. 4901.
- Rieke, V., Pauly, K.B., 2008. MR Thermometry. *J. Magn. Reson. Imaging* 27, 376–390.
- Roemer, P.B., Edelstein, W.A., Hayes, C.E., Souza, S.P., Mueller, O.M., 1990. The NMR phased array. *Magn. Reson. Med.* 16, 192–225.
- Rooney, W.D., Johnson, G., Li, X., Cohen, E.R., Kim, S.-G., Ugurbil, K., Springer, C.S., 2007. Magnetic field and tissue dependencies of human brain longitudinal  $1H_2O$  relaxation in vivo. *Magn. Reson. Med.* 57, 308–318.
- Saekho, S., Boada, F.E., Noll, D.C., Stenger, V.A., 2005. Small tip angle three-dimensional tailored radiofrequency slab-select pulse for reduced B1 inhomogeneity at 3 T. *Magn. Reson. Med.* 53, 479–484.
- Saekho, S., Yip, C., Noll, D.C., Boada, F.E., Stenger, V.A., 2006. Fast-kz three-dimensional tailored radiofrequency pulse for reduced B1 inhomogeneity. *Magn. Reson. Med.* 55, 719–724.

- Schmitter, S., Wu, X., Auerbach, E.J., Adrian, G., Pfeuffer, J., Hamm, M., Uğurbil, K., van de Moortele, P-F., 2014. Seven-Tesla Time-of-Flight Angiography Using a 16-Channel Parallel Transmit System With Power-Constrained 3-dimensional Spoke Radiofrequency Pulse Design. *Invest. Radiol.* 49, 314–325.
- Schneider, J.T., Kalayciyan, R., Haas, M., Herrmann, S.R., Ruhm, W., Hennig, J., Ullmann, P., 2013. Inner-volume imaging in vivo using three-dimensional parallel spatially selective excitation. *Magn. Reson. Med.* 69, 1367–1378.
- Setsompop, K., Wald, L.L., Alagappan, V., Gagoski, B.A., Adalsteinsson, E., 2008a. Magnitude least squares optimization for parallel radio frequency excitation design demonstrated at 7 Tesla with eight channels. *Magn. Reson. Med.* 59, 908–915.
- Setsompop, K., Alagappan, V., Zelinski, A.C., Potthast, A., Fontius, U., Hebrank, F., Schmitt, F., Wald, L.L., Adalsteinsson, E., 2008b. High-flip-angle slice-selective parallel RF transmission with 8 channels at 7 T. *J. Magn. Reson.* 195, 76–84.
- Setsompop, K., Alagappan, V., Gagoski, B., Witzel, T., Polimeni, J., Potthast, A., Hebrank, F., Fontius, U., Schmitt, F., Wald, L.L., Adalsteinsson, E., 2008c. Slice-selective RF pulses for in vivo B1+ inhomogeneity mitigation at 7 tesla using parallel RF excitation with a 16-element coil. *Magn. Reson. Med.* 60, 1422–1432.
- Shrivastava, D., Hanson, T., Kulesa, J., Tian, J., Adrian, G., Vaughan, J.T., 2011. Radiofrequency heating in porcine models with a “large” 32 cm internal diameter, 7 T (296 MHz) head coil. *Magn. Reson. Med.* 66, 255–263.
- Sijbers, J., Scheunders, P., Bonnet, N., Van Dyck, D., Raman, E., 1996. Quantification and improvement of the signal-to-noise ratio in a magnetic resonance image acquisition procedure. *Magn. Reson. Imaging* 14, 1157–1163.
- Silver, M., Joseph, R., Hoult, D.I., 1984. Highly selective  $\pi/2$  and  $\pi$  pulse generation. *J. Magn. Reson.* 59, 347–351.
- Smith, S.M., 2002. Fast robust automated brain extraction. *Hum. Brain Mapp.* 17, 143–155.
- Sodickson, A., Cory, D.G., 1998. A generalized k-space formalism for treating the spatial aspects of a variety of NMR experiments. *Prog. Nucl. Magn. Reson. Spectrosc.* 33, 77–108.
- Sodickson, D.K., Manning, W.J., 1997. Simultaneous acquisition of spatial harmonics (SMASH): fast imaging with radiofrequency coil arrays. *Magn. Reson. Med.* 38, 591–603.
- Staewen, R.S., Johnson, A.J., Ross, B.D., Parrish, T., Merkle, H., Garwood, M., 1990. 3-D FLASH imaging using a single surface coil and a new adiabatic pulse, BIR-4. *Invest. Radiol.* 25, 559–567.
- Stehling, M.K., Turner, R., Mansfield, P., 1991. Echo-planar imaging: magnetic resonance imaging in a fraction of a second. *Science* 254, 43–50.
- Szczerba, D., Neufeld, E., Zefferer, M., Szekely, G., Kuster, N., 2010. Unstructured mesh generation from the Virtual Family models for whole body biomedical simulations. *Procedia Comput. Sci.* 837–844.
- Triantafyllou, C., Hoge, R.D., Krueger, G., Wiggins, C.J., Potthast, A., Wiggins, G.C., Wald, L.L., 2005. Comparison of physiological noise at 1.5 T, 3 T and 7 T and optimization of fMRI acquisition parameters. *NeuroImage* 26, 243–250.
- Turner, R., Le Bihan, D., Maier, J., Vavrek, R., Hedges, L.K., Pekar, J., 1990. Echo-planar imaging of intravoxel incoherent motion. *Radiology* 177, 407–414.
- Turner, R., Le Bihan, D., Moonen, C.T., Despres, D., Frank, J., 1991. Echo-planar time course MRI of cat brain oxygenation changes. *Magn. Reson. Med.* 22, 159–166.
- Uecker, M., Zhang, S., Voit, D., Karaus, A., Merboldt, K-D., Frahm, J., 2010. Real-time MRI at a resolution of 20 ms. *NMR Biomed.* 23, 986–994.
- Uğurbil, K., Adrian, G., Andersen, P., Chen, W., Garwood, M., Gruetter, R., Henry, P-G., Kim, S-G., Lieu, H., Tkac, I., Vaughan, T., Van De Moortele, P-F., Yacoub, E., Zhu, X-H., 2003. Ultrahigh field magnetic resonance imaging and spectroscopy. *Magn. Reson. Imaging* 21, 1263–1281.

- Van de Moortele, P-F., Akgun, C., Adriany, G., Moeller, S., Ritter, J., Collins, C.M., Smith, M.B., Vaughan, J.T., Uğurbil, K., 2005. B1 destructive interferences and spatial phase patterns at 7 T with a head transceiver array coil. *Magn. Reson. Med.* 54, 1503–1518.
- van der Kolk, A.G., Zwanenburg, J.J.M., Brundel, M., Biessels, G-J., Visser, F., Luijten, P.R., Hendrikse, J., 2011. Intracranial Vessel Wall Imaging at 7T MRI. *Stroke* 42, 2478–2484.
- Vaughan, J.T., Hetherington, H.P., Otu, J.O., Pan, J.W., Pohost, G.M., 1994. High frequency volume coils for clinical NMR imaging and spectroscopy. *Magn. Reson. Med.* 32, 206–218.
- Visser, F., Zwanenburg, J.J.M., Hoogduin, J.M., Luijten, P.R., 2010. High-resolution magnetization-prepared 3D-FLAIR imaging at 7.0 Tesla. *Magn. Reson. Med.* 64, 194–202.
- Voigt, T., Homann, H., Katscher, U., Doessel, O., 2012. Patient-individual local SAR determination: in vivo measurements and numerical validation. *Magn. Reson. Med.* 68, 1117–1126.
- Wang, J., Fujiwara, O., 1999. FDTD computation of temperature rise in the human head for portable telephones. *IEEE Trans. Microw. Theory* 47, 1528–1534.
- Wang, Z., Lin, J.C., Mao, W., Liu, W., Smith, M.B., Collins, C.M., 2007a. SAR and temperature: Simulations and comparison to regulatory limits for MRI. *J. Magn. Reson. Imaging* 26, 437–441.
- Wang, Z., Smith, M.B., Collins, C.M., 2007b. Dependence of temperature increase on pulse sequence with equivalent time-average SAR. In: *Proc. Intl. Soc. Mag. Reson. Med.*, Berlin, Germany. p. 3247.
- Wang, Z., Lin, J.C., Vaughan, J.T., Collins, C.M., 2008. Consideration of physiological response in numerical models of temperature during MRI of the human head. *J. Magn. Reson. Imaging* 28, 1303–1308.
- Wang, Z., Collins, C.M., Zhao, S., Robb, F., 2009. The effect of human model resolution on numerical calculation of SAR and temperature in MRI. In: *Proc. Intl. Soc. Mag. Reson. Med.*, Honolulu, Hawaii, USA. p. 4797.
- Weinstein, Y.S., Havel, T.F., Emerson, J., Boulant, N., Saraceno, M., Lloyd, S., Cory, D.G., 2004. Quantum Process Tomography of the Quantum Fourier Transform. *J. Chem. Phys.* 121.
- Wiggins, C.J., Caillat, M., Le Bihan, D., Schmitt, F., Eberlein, E., 2010. Use of Opposed Shim Currents for Infold Reduction on a UHF MRI System with Head Gradient. In: *Proc. Intl. Soc. Mag. Reson. Med.*, Stockholm, Sweden. p. 2339.
- Wissler, E.H., 1998. Pennes' 1948 paper revisited. *J. Appl. Physiol.* 85, 35–41.
- Wolf, S., Speck, O., 2011. Comparison of deviations in SAR prediction between highly detailed and proper simplified human models at 7T. In: *Proc. Intl. Soc. Mag. Reson. Med.*, Montreal, Quebec, Canada. p. 3806.
- Wu, X., Schmitter, S., Auerbach, E.J., Moeller, S., Uğurbil, K., Van de Moortele, P-F., 2013. Simultaneous multislice multiband parallel radiofrequency excitation with independent slice-specific transmit B1 homogenization. *Magn. Reson. Med.* doi:10.1002/mrm.24828.
- Xu, D., King, K.F., Zhu, Y., McKinnon, G.C., Liang, Z-P., 2007. A noniterative method to design large-tip-angle multidimensional spatially-selective radio frequency pulses for parallel transmission. *Magn. Reson. Med.* 58, 326–334.
- Xu, D., King, K.F., Zhu, Y., McKinnon, G.C., Liang, Z-P., 2008. Designing multichannel, multidimensional, arbitrary flip angle RF pulses using an optimal control approach. *Magn. Reson. Med.* 59, 547–560.
- Yang, Q.X., Williams, G.D., Demeure, R.J., Mosher, T.J., Smith, M.B., 1998. Removal of local field gradient artifacts in  $T_2^*$ -weighted images at high fields by gradient-echo slice excitation profile imaging. *Magn. Reson. Med.* 39, 402–409.
- Yarnykh, V.L., 2007. Actual flip-angle imaging in the pulsed steady state: a method for rapid three-dimensional mapping of the transmitted radiofrequency field. *Magn. Reson. Med.* 57, 192–200.

- Yip, C-Y., Fessler, J.A., Noll, D.C., 2005. Iterative RF pulse design for multidimensional, small-tip-angle selective excitation. *Magn. Reson. Med.* 54, 908–917.
- Yip, C-Y., Grissom, W.A., Fessler, J.A., Noll, D.C., 2007. Joint design of trajectory and RF pulses for parallel excitation. *Magn. Reson. Med.* 58, 598–604.
- Zakhor, A., Weisskoff, R., Rzedzian, R., 1991. Optimal sampling and reconstruction of MRI signals resulting from sinusoidal gradients. *IEEE Trans. Signal Process.* 39, 2056–2065.
- Zelinski, A.C., Goyal, V.K., Angelone, L., Bonmassar, G., Wald, L.L., Adalsteinsson, E., 2007. Designing RF pulses with optimal specific absorption rate (SAR) characteristics and exploring excitation fidelity, SAR and pulse duration tradeoffs. In: *Proc. Intl. Soc. Mag. Reson. Med.*, Berlin, Germany. p. 1699.
- Zhu, Y., 2004. Parallel excitation with an array of transmit coils. *Magn. Reson. Med.* 51, 775–784.
- Zhu, Y., 2006. RF Power Deposition and “g-factor” in Parallel Transmit. In: *Proc. Intl. Soc. Mag. Reson. Med.*, Seattle, WA, USA, p. 599.
- Zuo, Z., Wang, R., Zhuo, Y., Xue, R., Lawrence, K.S.S., Wang, D.J., 2013. Turbo-FLASH Based Arterial Spin Labeled Perfusion MRI at 7 T. *PLoS ONE* 8. doi:10.1371/journal.pone.0066612.
- Zwanenburg, J.J.M., Hendrikse, J., Visser, F., Takahara, T., Luijten, P.R., 2010. Fluid attenuated inversion recovery (FLAIR) MRI at 7.0 Tesla: comparison with 1.5 and 3.0 Tesla. *Eur. Radiol.* 20, 915–922.